The Binary Fraction of Red Supergiants

Kathryn Forbes Neugent

A dissertation
submitted in partial fulfillment of the
requirements for the degree of

Doctor of Philosophy

University of Washington

2021

Reading Committee:

Emily Levesque, Chair

Benjamin Williams

Meredith Rawls

Philip Massey

Joseph Hellerstein

Program Authorized to Offer Degree:
Astronomy

University of Washington

Abstract

The Binary Fraction of Red Supergiants

Kathryn Forbes Neugent

Chair of the Supervisory Committee:
Dr. Emily Levesque
Astronomy

The binary fraction of massive main sequence OB stars is thought to be as high as 70%. However, until recently, only around a dozen binary red supergiants (RSGs) had been identified, despite the fact that these stars are the evolved descendants of most OB stars. As dictated by stellar evolution, binary RSGs will most commonly have B-type companions and such systems will have unique photometric signatures due to the shape of their spectral energy distributions. Using these signatures, we spectroscopically confirmed 250 new RSG+B binaries in the Local Group galaxies M31, M33, and the Magellanic Clouds. Near-IR photometric surveys of these galaxies additionally lead to the identification of a complete sample of RSGs down to a limiting luminosity. We estimated the binary fraction using a k-nearest neighbors algorithm that classifies RSGs as single or binary based on photometry with our spectroscopic sample as a training set. Taking into account observational biases, we calculated a RSG binary fraction as a function of metallicity in M31, M33, and the Large Magellanic Cloud and found that binary fraction appears to decrease with decreasing metallicity. This dependence most likely stems not from changes in the physical properties of RSGs due to metallicity, but changes in the parent distribution of OB binaries. Understanding this dependence is vital to supernovae population studies, predicting gravitational wave events, and deciphering how these massive stars enrich our Universe with heavy elements.

TABLE OF CONTENTS

Page

List of Figures iii

List of Tables v

Chapter 1: Introduction 1

Chapter 2: Detecting the Stellar Companions of RSGs 6
2.1 Observational Biases Against Detecting Companions 6
2.2 B-Type Stars 8
2.3 Stellar Atmosphere Models 12
2.4 Searching for RSGs with Balmer Lines 15
2.5 Photometric Criteria for Detecting Companions 19

Chapter 3: Characterizing B-type Companions 25
3.1 Spectroscopically Confirming RSG Binaries in M31 and M33 25
3.2 Newly Confirmed Small Magellanic Cloud RSG+B Star Binaries 39
3.3 Modeling the Spectra 43
3.4 Discussion 51

Chapter 4: The RSG Binary Fraction in the Large Magellanic Cloud 53
4.1 Identifying Red Supergiants 54
4.2 Spectroscopically Confirming RSG+B Binaries 66
4.3 Calculating the Binary Fraction 70
4.4 Discussion 80
4.5 Brief Summary 86

Chapter 5: The RSG Binary Fraction in M31 and M33 88
5.1 Spectroscopically Confirmed RSG+B Binaries 89

5.2 Classifying RSGs as Single or Binary 93
5.3 The Overall Binary Fraction 102

Chapter 6: RSG Binary Fraction as a Function of Metallicity 108
6.1 A Clear Trend 108
6.2 Possible Explanations 111
6.3 Comments on the Metallicities of M31 and M33 112
6.4 Summary 113

Chapter 7: Two Complementary Projects: Mass-Loss Rates and Mergers 115
7.1 Project #1: Measuring the Mass-Loss Rates of M31 RSGs 115
7.2 Mass-Loss in Red Supergiants 116
7.3 The Need for New Near-Infrared Data 118
7.4 Observations and Reductions 122
7.5 Identifying the Red Supergiants 126
7.6 Transformations of Photometry to Effective Temperatures and Bolometric Luminosities 137
7.7 Model Comparisons 140
7.8 Discussion 144
7.9 Summary and Conclusions 146
7.10 Project #2: RSG Mergers 146
7.11 The High Resolution Spectral Data 147
7.12 Identifying Merged RSGs 150

Chapter 8: Summary, Conclusions, and Next Steps 152

LIST OF FIGURES

Figure Number		Page
2.1	RSG Photometric Variability	7
2.2	Observed RSG Spectra with Blue Companions	11
2.3	Combined Model RSG and B Star Spectra	14
2.4	Observed and Model Spectra of 31 Cyg	16
2.5	Spectrum of LMC K1I + B Binary	17
2.6	Balmer Lines in RSG Binary W Cep	19
2.7	Constraining Balmer Line Detections	20
2.8	Synthetic Photometry of Model Spectra	21
2.9	Color-Color Diagram of Observed and Synthetic RSGs	23
2.10	Color-Color Diagram at Varying Metallicites	24
3.1	M31 and M33 LGGS Photometry	26
3.2	Stellar Contaminants in Color-Color Space	27
3.3	Color-Color Diagram of Observed RSG+B Candidates	29
3.4	Spectra of RSG+B star Binaries	30
3.5	Spectrum of a Symbiotic RSG	37
3.6	Spectrum of a RSG+Be Binary	42
3.7	MARCS Model Fits to RSG Spectra	44
3.8	BSTAR06 Model Fits to B star Spectra	46
4.1	LMC Color-Magnitude Diagram	55
4.2	LMC GAIA Proper Motion and Parallax Cuts	57
4.3	Color-Magnitude Diagram for Cool LMC Members	60
4.4	LMC k-NN Classification Results	75
4.5	HR Diagram from BPASS of RSG Companions	84
5.1	Color-Color Diagram of M31 and M33 RSG Binary Candidates	92
5.2	M31 and M33 k-NN Classification Results	100

6.1 M31 and M33 RSG+OB Binary Fraction As a Function of ρ 109
7.1 Theoretical RSG Luminosity Function 119
7.2 HR Diagram of M31 RSGs 122
7.3 Location of UKIRT M31 Fields 123
7.4 Photometric Errors 126
7.5 Observed Color Magnitude Diagram 129
7.6 M31 Color Magnitude Diagram 132
7.7 Control Field Color Magnitude Diagram 133
7.8 RSG Color Magnitude Diagram 136
7.9 RSG Extinction 139
7.10 HR Diagram of M31 RSGs 141
7.11 Observed M31 RSG Luminosity Function 143
7.12 High Resolution Spectrum of CE Tau 148

LIST OF TABLES

Table Number		Page
1.1	Previously Known RSG+B Star Binaries with Spectral Types	2
3.1	Coordinates and Magnitudes of Classified M31 and M33 Stars	31
3.2	Coordinates and Magnitudes of Confirmed MC RSG+B Star Binaries	40
3.3	Modeled Physical Parameters of Confirmed RSG+B Star Binaries	47
4.1	Adopted and Derived Relations for LMC	62
4.2	Red Supergiant Content of the LMC	66
4.3	Spectroscopically Observed SMC Stars	71
4.4	Percent Likelihood of Binarity	74
4.5	Binary Fraction of LMC RSGs	81
5.1	Spectroscopically Observed M31 and M33 Stars	94
5.2	k-NN Parameters	99
5.3	Binary Fraction	103
7.1	UKIRT Imaging	123
7.2	UKIRT Photometry M31 Fields A and B	127
7.3	UKIRT Photometry M31 Control Field	127
7.4	M31 Adopted and Derived Relations	135
7.5	Galactic RSGs Observed with EXPRES	149

ACKNOWLEDGMENTS

Twenty-one years ago, on February 2, 2000, I decided to become an astronomer. Jamin' Jamie, our field trip leader, took my 6th grade class on a night hike in Yosemite National Park and I saw the Milky Way for the first time. There have been a lot of twists and turns along the way, but here I am, *finally* getting my last degree.

First and foremost, I thank my PhD advisor Emily Levesque for her unwavering support over the past four eventful years. She was (and still is!) always available for a fun science discussion, but also encouraged me to independently develop my own ideas. I really can't imagine my PhD experience going much smoother (global pandemic aside), and the majority of that is due to Emily's advising.

I also couldn't have done this without the help of my longtime friend and collaborator, Phil Massey. Without our REU experience over a decade ago I'd still be making tons of money in the field of cyber security or studying something silly like asteroids. Actually, neither of those options sound that bad ... maybe I shouldn't have accepted that REU offer. Oh well, I guess everything has still worked out.

I've additionally been privileged to work alongside some amazing friends, collaborators, and mentors throughout the years including Nidia Morrell, Steve Slivan, Allison Youngblood, Bekki Dawson, Jamie Lomax, Maria Drout, and all my fellow University of Washington grads. In particular, I'd like to thank fellow massive star enthusiast Trevor Dorn-Wallenstein, and my 2017 cohort of Lupita Tovar, Brianna Thomas, and Dino Bektešević. I also appreciate the support and guidance from my committee including Ben Williams, Meredith Rawls, and my Graduate Student Representative, Joseph Hellerstein.

I would also like to acknowledge that much of the research presented here was done on

the traditional land of the first people of Seattle, the Duwamish People past and present and honor with gratitude the land itself and the Duwamish Tribe. Additionally, data used for this thesis was obtained at both Mauna Kea on the traditional land of the Kānaka Maoli, and at the MMT on the traditional land of the Tohono O'odham.

Finally, I thank my dear friend and partner, Garrett Thompson. The past four years have been full of incredible challenges and wonderful moments and I'm forever thankful you have been by my side. We're a pretty awesome power couple.

Chapter 1

INTRODUCTION

Massive stars are the cosmic engines that provide important energy input and chemical enrichment on galaxy-wide scales. Their UV radiation ionizes H II regions and powers the far-infrared luminosities of distant galaxies. They are the primary sources of carbon and oxygen, and their dramatic deaths as supernovae (SNe) produce all elements in the universe heavier than iron as they enrich the surrounding interstellar medium (ISM). They are also the source of the most energetic phenomena ever observed, emitting gamma-ray bursts as they collapse into black holes. During their core-collapse deaths they produce compact objects, a field currently undergoing a resurgence thanks to the recent discovery of gravitational waves. Massive star binary systems are the direct progenitors of the transient neutron star and black hole mergers that have recently been detected by LIGO (Abbott et al., 2016, 2017, 2019).

The majority of massive stars go through a red supergiant (RSG) phase after they turn off the main sequence and begin burning helium. Such RSGs are the evolved descendants of 8-30$M_{\odot}$ OB main sequence stars. After these luminous and hot OB stars burn through their core hydrogen, they evolve off the main sequence and briefly (over a couple hundred thousand years) pass through the yellow supergiant (YSG) phase before cooling down to temperatures below $T_{\rm eff} \sim 4300$K and drastically expanding in radius to reach sizes of hundreds or even thousands of times larger than the Sun. The vast majority of these stars then end their lives as Type II-P supernovae, though some higher mass RSGs evolve back bluewards to higher temperatures prior to core-collapse (e.g. Ekström et al. 2012).

While RSGs have been a topic of great interest for decades, until the past few years not much was known about their binary properties. When this dissertation research began in 2018, only around a dozen confirmed binary RSGs were known (see Table 1.1 for the 10

Table 1.1. Previously Known RSG+B Star Binaries with Spectral Types

Name	Type	Reference
22 Vul	G4I + B9V	Ahmad & Parsons (1985)
31 Cyg	K4Iab + B4IV-V	Vinter Hansen (1944); Stencel et al. (1984)
32 Cyg	K5Iab + B7V	McLaughlin (1950); Chun (1992)
AL Vel	RSG + BV	Kilkenny et al. (1995)
BD +59°224	K4.5Ib + B3V	Gray & Skiff (2004)
XX Per	M4Ib + B7V	Stothers & Leung (1971)
V766 Cen	RSG + BV	Wittkowski et al. (2017)
V838 Mon	MI + BV	Munari et al. (2007); Tylenda et al. (2009)
VV Cep	M2Iab + B0-2V	Cowley (1969); Pollmann et al. (2017)
α Sco	M1.5Iab-Ib + B2.5V	Baade & Reimers (2007)

with known spectral types) among the hundreds known in our own Galaxy. This low binary fraction of RSGs is in contrast with the relatively high binary fraction of their un-evolved counterparts, the OB stars. Studies of un-evolved massive stars typically find an observed binary fraction of 30-35% for O-type stars in relatively short period systems (Garmany et al., 1980; Sana et al., 2013). These short period systems are generally interacting and experiencing Roche-lobe overflow (RLOF) where one star ends up stripping its more massive companion of material. In systems such as these, the evolution of both of the stars is heavily altered due to being in a binary system. However, there are additionally longer-period systems that are gravitationally bound but not experiencing RLOF or really interacting in any material sense. When such long-period systems are included, the percentage of binary OB stars rises and approaches 70% or more (Gies, 2008; Sana et al., 2012). However, it is not clear to what extent these long-period systems are important from an evolutionary perspective (see, for instance, discussion in Massey et al. 2017). If the two stars in these long-period systems never interact, in many ways they can essentially be thought of as single stars from an evolutionary perspective. Still, if the binary fraction of these un-evolved OB stars is perhaps higher than 70%, why were there only a dozen binary RSGs known out of

the hundreds of known Galactic RSGs?

The explanation for such an apparent lack of RSG binaries could either point to an observational or evolutionary bias. As is discussed in detail in Chapter 2, the two main methods commonly used for identifying binary systems, radial velocity variations and light curve studies, are quite inefficient at detecting large populations of binary RSGs. This is primarily due to their decade-long periods. VV Cep, for example, has a 20.3 year orbit (Bauer & Bennett, 2000) meaning baseline photometry and spectroscopy for light curve and radial velocity variation studies would need to span several decades to obtain a reliable binary detection. This points to a strong observational bias against detecting such systems on a regular basis with currently available datasets. But, let's also consider an evolutionary bias. If the OB binary fraction begins as 70%, what then happens to all of the binaries once the more massive star evolves into a RSG? In some close systems the binaries will experience RLOF. When this occurs, it can either lead to stable mass transfer, where the primary will be stripped and will thus never evolve into a RSG (see discussion in Dorn-Wallenstein & Levesque 2018), or unstable mass transfer, where the mass is accreted by the secondary faster than it can absorb. In this second case of unstable mass transfer, the secondary will also overflow its Roche lobe and the two stars will enter the common envelope phase. At this point, depending on their proximity, the primary will still evolve into a RSG and over time could merge with its less massive companion. An overview of these scenarios is further described in Ch. 5 of Levesque (2017). However, in the systems with large enough separations, the binary companion should remain. Thus, from an evolutionary point of view, there should also be fewer RSG binary systems than OB binary systems due to mergers. This dissertation attempts to better understand and quantify both these observational and evolutionary biases to determine the overall RSG binary fraction.

In addition to RSG binaries being potentially difficult to detect, there are other reasons why the binary fraction of RSGs had not been well characterized prior to this work. Understanding the binary fraction requires both understanding the number of binary RSGs, but also the total population of RSGs. Our location within one of the Galaxy's dusty spiral arms

makes it impossible to observe the majority of the Milky Way's RSGs given high extinction within the Galactic plane. However, the galaxies of the Local Group provide ideal test beds for such research. They are close enough (and massive stars are luminous enough) that we can characterize luminosity-limited samples of various types of massive stars. However, when searching for RSGs, there are two contaminants that must be removed: foreground red dwarfs, and lower-mass asymptotic giant branch (AGB) stars. Until recently, the process involved in removing these two contaminants was observationally cost-prohibitive towards identifying a complete sample of RSGs in one of the Local Group galaxies. However, as discussed later, thanks to the parallax and proper motion results from Gaia (Gaia Collaboration et al., 2018), as well as a better understanding of the near infrared colors and magnitudes of RSGs compared to AGB stars, we are now able to determine a luminosity-limited sample of RSGs in nearby galaxies and thus make the first determination of the RSG binary fraction.

Obtaining the RSG binary fraction in various Local Group galaxies additionally allows us to investigate it as a function of metallicity. The combination M31, M33 and the Magellanic Clouds allow us to target a large metallicity range with M31 having a super-solar metallicity of $\log(O/H) + 12 = 8.9$ (Sanders et al., 2012), the Large Magellanic Cloud (LMC) having a sub-solar metallicity of $\log(O/H) + 12 = 8.4$ (Russell & Dopita, 1990), and then M33 having a strong metallicity gradient as a function of distance from the center that spans from $\log(O/H) + 12 = 8.3$ in the outer regions to approximately solar ($\log(O/H) + 12 = 8.7$) in the inner regions (Magrini et al., 2007). While there is no doubt that the evolution of massive stars is drastically influenced by the star's initial metallicity (see Maeder 1991; Maeder & Conti 1994), it is less clear whether metallicity influences the binary fraction of such stars, particularly for evolved massive stars. Many studies have been done on the binary fraction of Wolf-Rayet (WR) stars in the Local Group galaxies M31 and M33 (Neugent & Massey, 2014) and the Magellanic Clouds (Foellmi et al., 2003b,a; Bartzakos et al., 2001) and all research points to a metallicity-independent binary fraction of 30-40%. Additionally, there is little evidence for a metallicity dependence in the binary fraction of un-evolved OB stars (e.g. Moe & Di Stefano 2017; Moe et al. 2019). But, before this dissertation, no

observational tests had looked at how the binary fraction of the less massive RSGs might change with metallicity.

These results present the first large-scale, multi-galaxy study of the binary fraction of RSGs as a function of metallicity and can be used to compare with evolutionary and population synthesis models. The recent result that ∼60% of massive stars may *interact* with their binary companions throughout their lives (Sana et al., 2012) has a profound impact on the predicted populations of supernovae (Eldridge et al., 2018; Zapartas et al., 2019), gravitational wave sources (e.g. Tauris et al., 2017), and the ionizing radiation from stellar populations (Götberg et al., 2019; Stanway et al., 2016). However, the details of these predictions depend not only on the initial binary conditions, but also on the outcomes of simplified prescriptions for parameters such as the mass transfer efficiency and outcomes of common envelope evolution (e.g. Podsiadlowski et al., 1992; Wellstein & Langer, 1999; Eldridge et al., 2008). As the OB binary fraction and properties becomes better established, this measurement of the binary fraction of their more evolved descendent stars will provide an important boundary condition to test our models of binary evolution.

This dissertation is broadly presented in chronological order as a combination of five published papers. Chapter 2 is based on Neugent et al. (2018a) and discusses the types of companions we expect to exist in binary systems with RSGs as well as how they might be detected. Chapter 3 follows the work of Neugent et al. (2019) and the process of observing and confirming new RSG binaries in M31, M33, and the LMC. Chapter 4 takes a closer look at the binary fraction of RSGs in the LMC (from Neugent et al. 2020a), while Chapter 5 includes work done in M31 and M33 before comparing the overall RSG binary fraction across metallicities in Chapter 6 (from Neugent 2021). Chapter 7 presents two complementary projects including research done by Neugent et al. (2020b) on RSG mass-loss and the resulting luminosity function in M31, and ongoing research searching for merged RSGs. Finally, a summary and conclusions is presented in Chapter 8.

Chapter 2

DETECTING THE STELLAR COMPANIONS OF RSGS

2.1 Observational Biases Against Detecting Companions

With only around a dozen binary RSGs known, the natural first question was: why were there so few? Did this point to an observational bias, or were binary RSGs incredibly rare and those that had been found represented the majority of the existing systems? Given the high binary fraction of un-evolved OB stars, it seemed more likely that an observational bias was at fault. For example, the two methods commonly used to detect stellar binary systems – photometric and radial velocity variability – are quite inefficient when attempting population studies of RSG binaries.

2.1.1 Photometric Variability

One of the most widely used methods of detecting binary stars is to search for ellipsoidal variations in a star's light curve. However, detecting binary RSGs in this manner has proven to be quite difficult. RSGs themselves have quite large photometric variations, often on the order of 1 magnitude or higher. These variations can create their own periodic light curves, often making it difficult to distinguish between an orbiting star or something intrinsic to the RSG itself. For example, RSGs are known to pulsate on the order of 80 to 3500 days (Guo & Li, 2002), and large convective cells ($\sim$0.5-2 AU across) and hot spots in their chromospheres have timescales on the order of weeks to months or even years (Chiavassa et al., 2011; Baron et al., 2014; Stothers, 2010). Photometric variability in these stars can also be random due to shocks in the atmosphere which excite emission features and large mass-loss events, such as the one recently undergone by Betelgeuse (Levesque & Massey, 2020). All of these variations create difficulties in searching for binary RSGs based on their periodic light curve signatures.

For example, take the lightcurves of two RSGs shown in Figure 2.1. Both of these RSGs show no spectroscopic evidence of a binary companion, and yet they are photometrically variable over the entire 6 year lightcurve obtained by the Zwicky Transient Facility (Bellm et al., 2019). These variations could be due to any of the physical mechanisms described above, and any of these could easily mask the presence of a binary companion in the lightcurve. Thus, searching for binary RSGs using lightcurve analysis is fraught with complications.

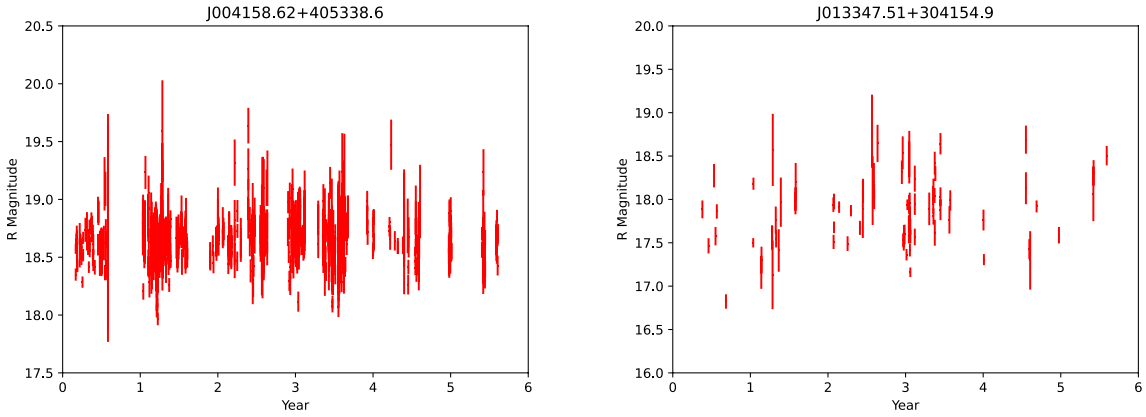

Figure 2.1 - Change in R magnitude of two spectroscopically single RSGs over 6 years taken by the Zwicky Transient Facility. Note in many cases that the photometric variations are larger than the errors (as denoted by the point length), and such variations exceed a magnitude over the course of the survey. The brightness changes are likely due to physical processes within the individual RSGs and not because of the existence of a companion star.

2.1.2 Radial Velocity Variations

Another popular method of detecting stellar binarity is by searching for radial velocity variations by measuring the shift in spectral line locations. For close systems with short periods and small mass discrepancies, these radial velocity shifts can be quite dramatic and on the order of 10s of Angstroms. However, RSGs have radii over thousands of times larger than that of the Sun and thus such binary systems have periods on the order of thousands of days. Thus, searching for radial velocity variations requires a very targeted, high spectral resolution, spectroscopic survey with repeated observations done over a baseline of decades. Take, for example, the Galactic RSG+B star binary system, VV Cep which has a 20.3 year orbit (Bauer & Bennett, 2000). Spectroscopy of such a system would need to occur over a period of years before the radial velocity shift would be apparent in the RSG spectral lines. Therefore, radial velocity variation studies are not a reliable method of searching for binary RSGs on a large scale. However, several long-baseline RSG spectroscopic surveys were completed during the course of this thesis that did successfully identify RSGs with radial velocity shifts (Dorda & Patrick, 2021; Patrick et al., 2019). Their results are discussed primarily in Chapter 6.

2.2 B-Type Stars

We next investigated what type of stellar companion a RSG would have. Of the known RSG binary systems, all of them contain a B star companion (see Table 1.1). Could this simply be a byproduct of observational biases? For example, would a bright O star simply dominate the RSG spectrum? Or would an A dwarf spectrum not be visible at all in a binary system? To answer this question, we first examined this from an observational point of view by combining spectra to "create" different binary systems. We then investigated this issue from an evolutionary point of view by determining what types of stars at different masses would be alive during a RSG's lifetime.

2.2.1 First Look: The Atlas

We first created our own set of spectra showing RSGs in systems with various types of stars. To do this we used a library of stellar spectra created by Jacoby et al. (1984). This spectral database contains fluxed spectra spanning all types and luminosity classes of Galactic stars. Using this database we were able to make a grid of RSG binary spectra combined with the spectra of different types of stars. While we realize that many of these combinations are unphysical from an evolutionary point of view (as discussed in the next section), we first wanted to investigate this from an observational point of view.

To combine the observed spectra we first needed to make several adjustments. We corrected for the reddening of each spectrum using the CCM law Cardelli et al. (1989) where we obtained V using SIMBAD (Wenger et al., 2000) and were provided E(B-V) by Jacoby et al. (1984). We then corrected for the distance to each star using the absolute visual magnitudes based on spectral type from Cox (2000) and Humphreys & McElroy (1984). Multiplying the derived distance correction by the spectral flux produced a reddening and distance corrected spectrum. At this point we could simply add the spectra together to get an "observed" combined spectrum.

Figure 2.2 shows a few examples of spectra combined with the spectrum of a M1Iab, FZ Per. Humphreys & McElroy (1984) estimate an M_V of -6.0 for a typical M1Iab (later we redo this investigation for a more complete set of M_Vs)[1]. Note that, as hypothesized above, the O star spectrum (even as a dwarf) simply overpowers the RSG spectrum. In this case, while the SED shows a slight turn-up in the red, this would hardly be noticeable even with perfect flux calibration. Conversely, both the blue B star's spectrum and the red RSG's spectrum is clearly visible in the combined spectrum for the M1Iab+B0V. This combined spectrum's SED

[1]Now that *Gaia* distances are available, better calibrations for the absolute magnitudes of RSGs will doubtless become available, but this is beyond the scope, or needs, of the present project (also, some of the individual stars we use from Jacoby et al. (1984) are actually too bright for reliable *Gaia* parallaxes.) The absolute magnitudes we have adopted are consistent with what is known for RSGs where the distances are well known, such as the LMC (Levesque et al., 2006) and M31/M33 (Drout et al., 2012; Massey et al., 2009). We note that for FZ Per the agreement is quite good between our approximate method ($M_V = -6$) and the more exact Mv given by the distance Gaia provides ($M_V = -5.6$).

is nearly flat, an attribute we rely on later when searching for these stars photometrically. The remaining two figures show the RSG spectrum combined with a spectrum of an A dwarf and an A supergiant. In the A dwarf's case, the RSG spectrum dominates while in the A supergiant's case, the A star dominates. It would be impossible to determine binarity from spectroscopy. Overall, there appears to be a sweet spot when detecting a binary system spectroscopically because in most cases one of the spectra will "drown out" the other.

2.2.2 Evolutionary Models

While the above exercise is helpful, these stars must co-exist from an evolutionary point of view if they are to be in a binary system with one another. To investigate this we used the Geneva evolutionary models (Georgy et al., 2013; Ekström et al., 2012)[2] to determine the type of star that would exist in a system with a RSG at different mass ranges. We used the evolutionary models to create a grid of models between 0.9 and 29 solar masses.

We did not go above $29M_{\odot}$ because we determined by interpolating between the published Geneva tracks[3] that the most massive star that will become a RSG is $29M_{\odot}$ Ekström et al. (2012). Since the more massive star is going to evolve first, we were justified in starting with $29M_{\odot}$. We then began with the highest mass model and combined it with the lower mass models and did this iteratively for each mass, decreasing in mass after each run. For example, we first combined the $29M_{\odot}$ model with the 27, 25, 23, 20, 15, 12, 9, 7, 5, 4, 3, 2, 1, and $0.9M_{\odot}$ models before then combining the $27M_{\odot}$ model with the 0.9-$25M_{\odot}$ models and so on. For each of these model combinations, we determined the age at which the higher mass model - the primary in a binary system - would be a RSG (as defined by having $T_{\rm eff}$ less than 4500 K) and then determined what type of star the lower mass model would be during the timeframe that the primary would spend as a RSG.

For every one of these combinations we found that the RSG will always be in a system

[2]Since we are assuming these are non-interacting, wide-period binaries, we believe using single star models is appropriate (Georgy & Ekström, 2018).

[3]`https://www.unige.ch/sciences/astro/evolution/en/database/syclist/`

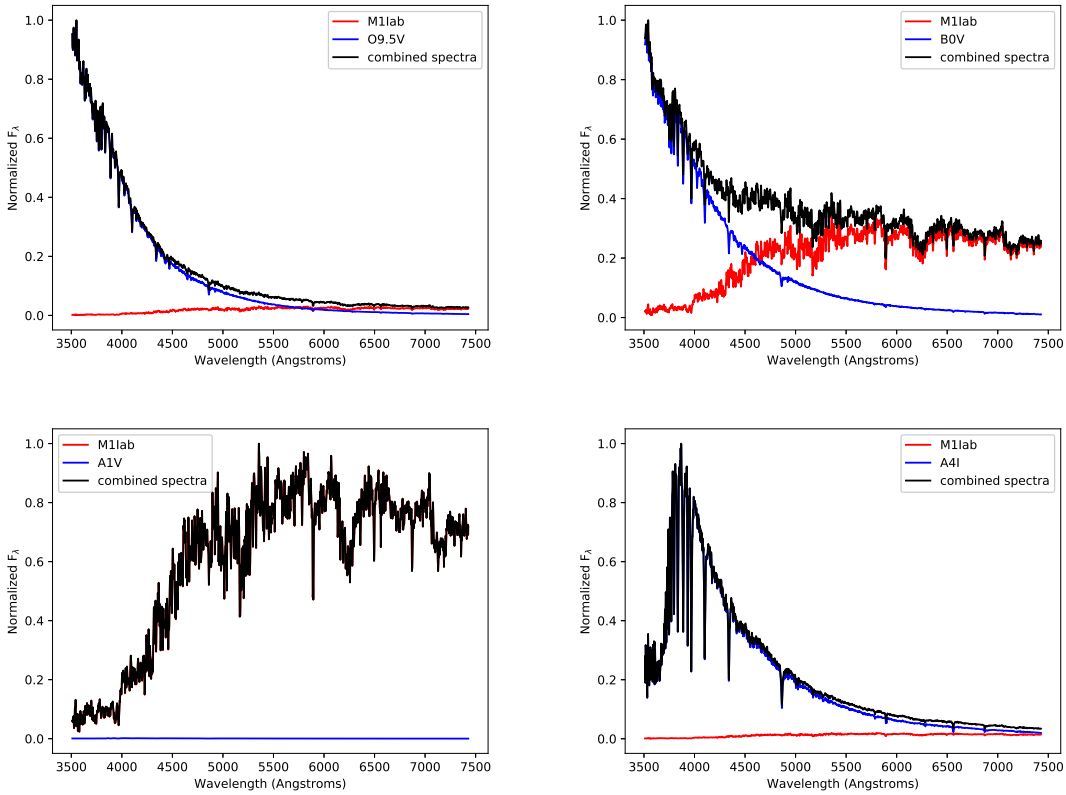

Figure 2.2 - A spectrum of FZ Per, a M1Iab, combined with the spectra of O9.5V, B0V, A1V and A4I stars. The upper left figure shows the M1Iab spectrum combined with the spectrum of BD+62 0249, an O9.5V. In this figure the O9.5V's spectrum dominates the combined spectrum. The upper right figure shows the M1Iab spectrum combined with the spectrum of HD 3237007, a B0V. In this figure both the blue upper Balmer lines and red TiO lines are clearly visible in the combined spectrum. The bottom left figure shows the M1Iab spectrum combined with the spectrum of HD 116608, an A1V. In this case the M1Iab's spectrum is the only one visible in the combined spectrum. The bottom right figure shows the opposite situation where the A4I spectrum (SAO 12096) dominates over the M1Iab RSG's spectrum. All stars and spectra taken from Jacoby et al. (1984). © AAS. Reproduced with permission from Neugent et al. (2018a).

with a B star companion (either a V, III, or I) – this is the primary evolutionary pairing. To make sense of this, we make the assumption that both of the stars within the system are non-interacting (most likely a wide-period binary) and were formed at the same time (see discussion in Section 10 of Moe & Di Stefano 2017). While there are certainly cases where this is not true (for example, a star that is born as a single star and later gravitationally captured by a companion), in general we can assume that both stars in the system formed at the same time.

2.3 Stellar Atmosphere Models

Knowing that binary RSGs primarily exist in systems with B stars, we next used synthetic spectra from model atmospheres to create a database of B star + RSG synthetic spectra. To do this we relied most heavily on two atmospheric modeling database: BSTAR06 (Lanz & Hubeny, 2007) and the MARCS models (Plez et al., 1992)[4].

BSTARS06 is a grid of non-LTE, line-blanketed, plane-parallel, hydrostatic model atmospheres. Temperatures range from 15000 K to 30000 K and include surface gravities ($\log g$) between 1.75 and 4.75 dex. Metallicities range from one tenth to two times solar. There are additional models computed specifically for B supergiants. More information can be found in Lanz & Hubeny (2007).

The MARCS models are a grid of one-dimensional, hydrostatic, plane-parallel and spherical LTE model atmospheres. They encompass spectral types F, G, and K. There are 280 specialized spherical RSG models that were used specifically for this work. Their effective temperatures range from 3400 to 4250 K with [cgs] surface gravities between -0.5 and 1 dex. Metallicities range from one-tenth to 3 times solar ([Fe/H]=-1.0 to +0.3) and the microturbulence parameter is 5 km s^{-1}. More information can be found in Plez et al. (1992).

---

[4]We chose the MARCS models over the PHOENIX models (Husser et al., 2013) because they were successfully used by Levesque et al. (2005) to redefine the effective temperature scale of RSGs and show that their location on the Hertzsprung-Russell diagram was consistent with evolutionary theory.

2.3.1 Combination Process

Over all, 24,640 spectra were created from these models, combining RSGs and B stars of various temperatures and luminosities. These contained B-type stars ranging from 15000 K to 30000 K (in 1000 K steps) with luminosity classes of V, III and I; RSGs from 3400 K to 4250 K (in 1000 K steps with the exception of the last model) with masses of 10, 15, 20 and 25 $M_{\odot}$; and all of these combinations at reddenings of $A_V = 0$ to 2.6 mags (in steps of 0.2 mags).

We used the solar metallicity models for all stars (though we later investigated the effect of different metallicities on our results). Surface gravities for the BSTAR06 models were varied based on the type and luminosity class of the star (Supergiants ranged from $\log g = 2.50$ dex at the hot end and 3.00 dex at the cooler temperatures. Giants ranged between 3.25 dex to 3.50 dex and dwarfs were set to 4.0 dex) while surface gravities of the MARCS RSG models were set to 0.00 dex. All lines were rotationally broadened. The MARCS models were already rotationally broadened before being distributed while the BSTAR06 models were broadened using 150 km s^{-1} following Huang & Gies (2006).

Before adding the spectra together, we first put their fluxes on the same absolute scale. The surface fluxes for both sets of models are in units of [erg s^{-1} cm^{-2} Angstrom^{-1}]. However, before combination we needed to account for their differing luminosities and radii. For the MARCS models, radii and luminosities were taken from the MARCS inputs as given in the model headers. For the B stars we determined the M_V and bolometric corrections based on Humphreys & McElroy (1984) and selected an appropriate surface gravity. We then determined the bolometric luminosities by adopting the absolute visual magnitudes. The radii of each B star model was then calculated using the appropriate luminosity and temperature. Finally, we multiplied the model flux by the square of the appropriate radius.

Our treatment of dust is relatively simplistic. The spectra were reddened for values ranging between $A_V = 0$ and 2.6 mags in steps of 0.2 mags using the CCM law (Cardelli et al., 1989) as RSGs are known to have A_V values that vary over this range (see, for

example, Table 4 of Levesque et al. 2005). We made the conservative assumption that the B star would be enshrouded in the RSG's dust, although this would clearly depend upon the orbital separation. If the B star were less reddened than the RSG then its spectrum in the blue would be even more pronounced.

The resulting $\sim 25,000$ models span a range of combined spectra. A few examples can be seen in Figure 2.3. The model in the top left shows a single 15000 K B dwarf with clear upper Balmer lines. The model in the top right then shows a cool RSG added into a warm B dwarf. The resulting model shows strong Balmer lines but a hint of TiO bands. As the models progress, the TiO bands become stronger and the Balmer lines become weaker as the RSG begins to dominate the spectrum. Finally, the bottom right panel shows a single 3400 K RSG spectrum.

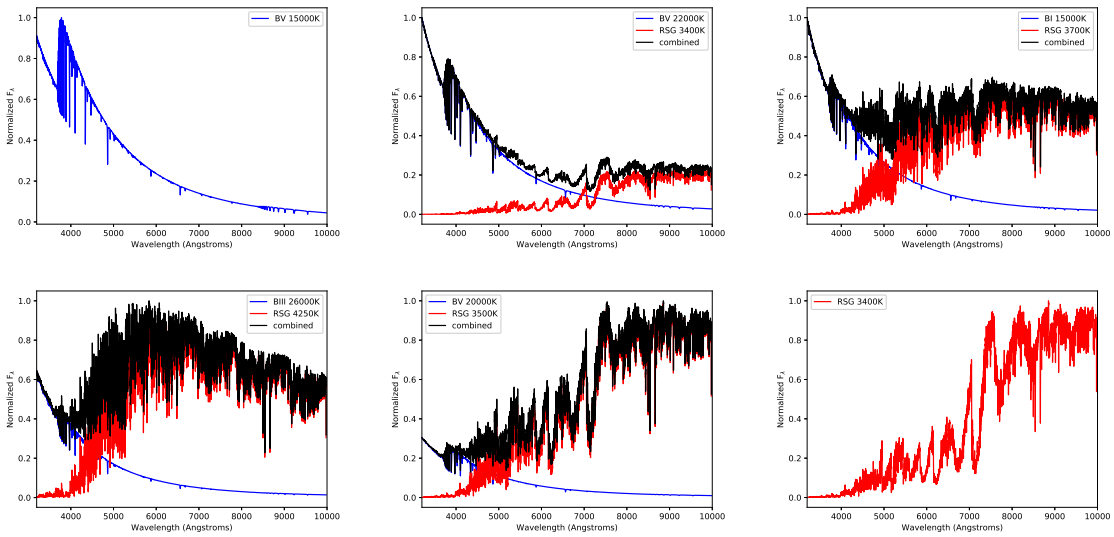

Figure 2.3 - Various combinations of un-reddened synthetic BSTARS06 and MARCS spectra going from a 15000 K BI to a 3400 K RSG with four combinations in between. Note as the Balmer lines grow fainter as the TiO bands grow stronger from top to bottom. © AAS. Reproduced with permission from Neugent et al. (2018a).

Now that we have our combined spectra, we can compare our results with observations.

31 Cyg is an eclipsing binary made up of a K4Iab + B4IV-V with a period of around 10 years (Samus et al., 2009). To test the accuracy of the synthetic combined spectra, we created a combined spectrum of a K4I+B4V star (where the K4I is modeled by a 3800 K RSG and the B4V is modeled by a 19000 K BV), and then compared it to the observed spectrum of this system kindly provided by Phil Bennett. Note the similar shape of the spectral energy distribution (SED) as well as the strengths of the upper Balmer lines and TiO feature near 5167Å.

2.4 Searching for RSGs with Balmer Lines

Our synthetic spectra, the spectrum of 31 Cyg (see Figure 2.4), and the RSG+B stars discussed in the Introduction show that these stars are detectable spectroscopically. From a previous observational survey we had spectra of 598 RSGs in the Magellanic Clouds (MCs) that provided a perfect chance to search for binary RSGs. We also used new spectroscopic observations to search for evidence of additional RSG binaries within our own Galaxy. These observations help us learn more about the binary frequency of RSGs and constrain how difficult they are to discover through spectroscopic observations.

2.4.1 Magellanic Cloud Observations

In connection with another project, we obtained spectra of 598 RSGs within the MCs, and classified them using their spectral lines and determined MC membership based on radial velocities (Evans & Massey, 2017). (The spectra will be described in more detail in a future paper by Evans et al.) We then examined their spectra for this work in an attempt to detect upper Balmer lines. An example spectrum with observable Balmer lines is shown in Figure 2.5. Of the 311 Small Magellanic Cloud (SMC) stars and 287 Large Magellanic Cloud (LMC) stars, 25 stars (14 LMC and 11 SMC) have clear upper Balmer lines in their spectra as is shown in Figure 2.5. We did not find any spectra that appeared to be in a spectroscopic binary with any other type of star (O star, RSG, or WR, for example). While these small numbers might not be enough to do population statistics (the LMC and SMC

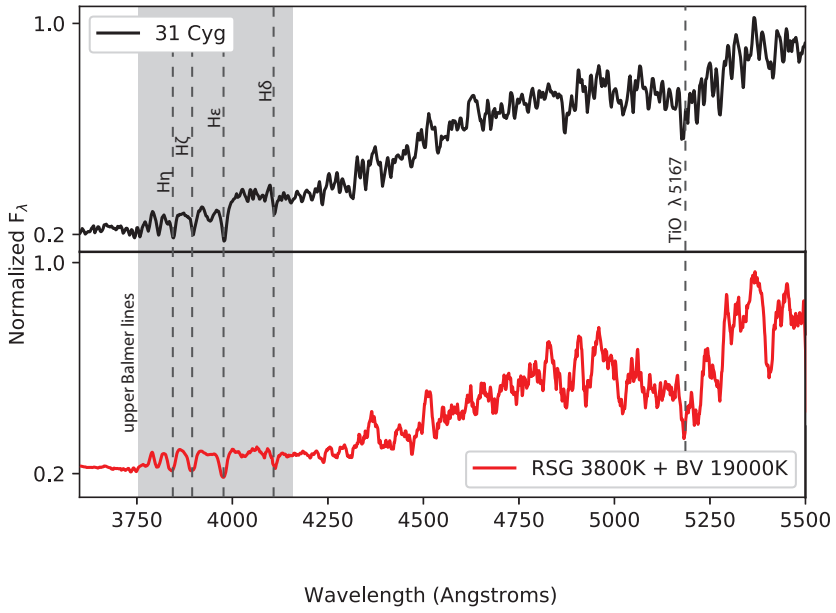

Figure 2.4 - Comparison of observed 31 Cyg spectrum with model BSTAR06 + MARCS combined spectrum. 31 Cyg is a K4Iab + B4IV-V so we chose a 3800 K RSG model to represent the K4Iab star and a 19000 K B dwarf model to represent the B4IV-V star. Note the agreement between the upper Balmer lines between 3750 and 4000 Å as well as the strong TiO band at around 5167Å. Note that the model has been smoothed so that both spectra have about the same resolution. The 31 Cyg spectrum was kindly provided by Phil Bennett.

RSG samples cannot be considered complete), it is clear that RSG + B star binaries are present and observable throughout the MCs.

2.4.2 Galactic Observations

We additionally carried out our own observing campaign searching for Balmer lines in the spectra of known Galactic RSGs. Our goal was not to characterize all of the known RSGs within the Galaxy. Instead we wanted to determine how difficult it is to detect different

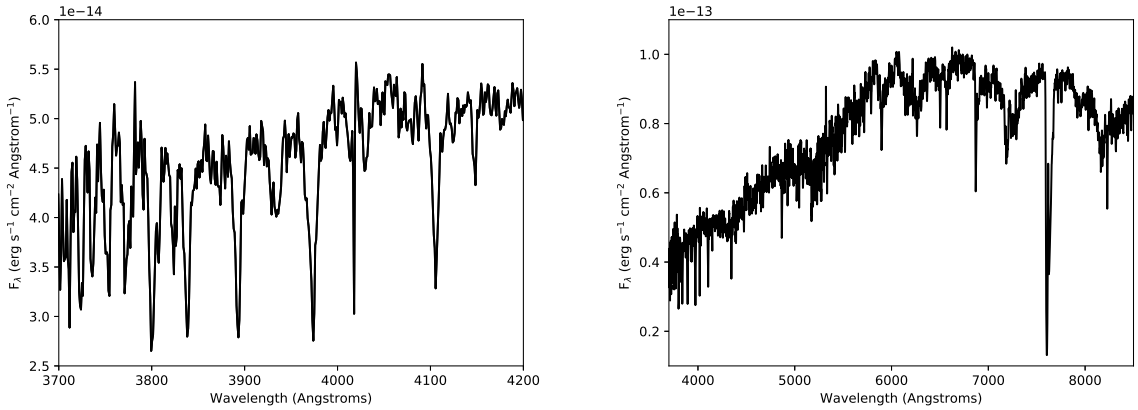

Figure 2.5 - Spectrum of the LMC star J05043378-6806235, a 3900 K K1I + B star companion. In the figure on the right, notice the strong TiO lines upward of 5000 Å indicative of a RSG with strong Balmer lines between 3700 and 4000 Å. The figure on the left shows a closer look at the Balmer lines. Spectra will be published in an upcoming paper by Evans et al. © AAS. Reproduced with permission from Neugent et al. (2018a).

types and luminosity classes of B stars within a RSG's spectrum.

Observations and Reductions

Targets were selected from Humphreys (1978) and Levesque et al. (2005) to ensure we were observing confirmed RSGs as opposed to red giants. Observations were taken on the Apache Point Observatory's 3.5-m telescope using the Dual Imaging Spectrograph (DIS). All of our observations were taken over a clear three night run from UT 21-23 June 2018 during the B half of the night. The seeing was fairly steady and ranged between 1-1.5" throughout the three nights. We observed the 0.9" slit on the first night but switched to the 1.2" slit for the second and third nights due to poor seeing conditions. Since we were interested in the upper Balmer lines spanning from around 3750 - 4000Å, we used the high dispersion B1200 grating centered at 4280Å giving a total wavelength coverage from 3660Å to 4900Å at $R = 3500$. Because the U-band fluxes of the RSGs are quite faint despite the generally

bright V magnitudes, we wound up having to expose for up to 2 hours for a $V = 10$ star to achieve a SN of 100 in the region of the upper Balmer lines. When observing these stars we simply turned off the red channel of the camera to avoid almost certain saturation in the red. We observed the stars in order of decreasing magnitude (and thus increasing exposure time) in an attempt to observe the largest number of targets. We additionally observed Feige 110 and BD+28 421 for flux calibration.

Biases, quartz projector flats, and He-Ne-Ar comparison arcs were obtained during the day and used for reductions. The data were first overscan-subtracted and trimmed and then the remaining bias structure was removed using a master averaged bias. The spectra were extracted using IRAF's "doslit" package[5]. Spectra with multiple observations were then combined with cosmic rays rejected.

Hidden B Stars

During our observing run we observed 20 known RSGs with a signal-to-noise (S/N) $\sim$ 100. None of these stars had Balmer lines except for one known binary, W Cep which is a V = 7.6 mag binary. Our spectrum of W Cep can be seen in Figure 2.6 showing that at least one of the brighter known RSG + B stars can be detected through the presence of Balmer absorption lines.

Even though we did not find any new RSGs with B star companions, these spectra allowed us to constrain the type of B star that could be hidden in the spectra (if any). To do this we relied on the fact that most of these stars had previously been modeled by Levesque et al. (2005) using the MARCS models. Because of this, we were able to shift the observed spectra to the appropriate MARCS model and match the two SEDs. We could then add in the blue BSTAR06 models of increasing brightness until it was possible to see Balmer lines. This process is shown in Figure 2.7. Of the 20 observed stars, six stars had not been modeled

[5]IRAF is distributed by the National Optical Astronomy Observatory, which is operated by the Association of Universities for Research in Astronomy (AURA) under a cooperative agreement with the National Science Foundation.

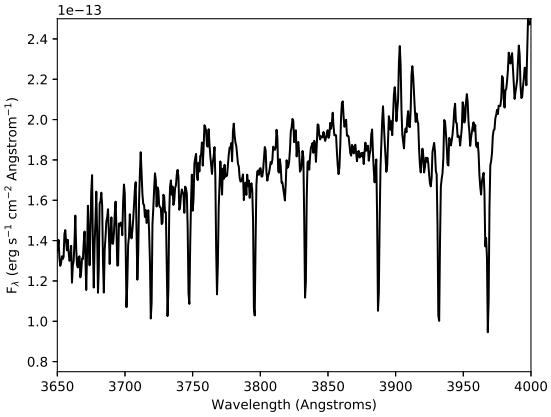

Figure 2.6 - Observed Balmer lines in W Cep. Notice the strong Balmer lines observed as part of our Galactic RSG observing campaign. This proves to us that our set-up was capable of detecting the bright Balmer lines of a RSG+B star binary. © AAS. Reproduced with permission from Neugent et al. (2018a).

using MARCS spectra. Three of the warmest RSGs could have concealed B dwarf stars up to 30000 K ($M_V = -3.5$), while 11 could not have concealed even the faintest BSTAR06 model in our sample (a 15000 K B dwarf; $M_V = -1.5$). Thus, given a S/N of greater than 100 at moderation spectral resolutions ($R > 3000$), it is possible to determine conclusively whether a RSG has a visible (i.e., non-eclipsed) B star companion contributing to its spectrum.

There is a potential problem with this approach. We are making the initial assumption that the star modeled by the MARCS model is a single RSG (with no B star companion) and thus the signal on the blue end is only coming from the RSG. If there was a B star hidden within the spectrum, the blue end would be raised slightly. However, given that we do not see any Balmer lines in the spectrum we believe we can rule out this possibility.

2.5 Photometric Criteria for Detecting Companions

Next we examined the photometric properties of the RSG+B star binaries. Figures 2.2 and 2.3 show the synthetic spectra of a binary RSG and B star. Note that the SED of a RSG+B star binary spectrum is quite a bit flatter than that of either a B star or RSG alone; there is nearly equal signal in both the red and the blue. Given the right set of photometric criteria, we should be able to detect this feature.

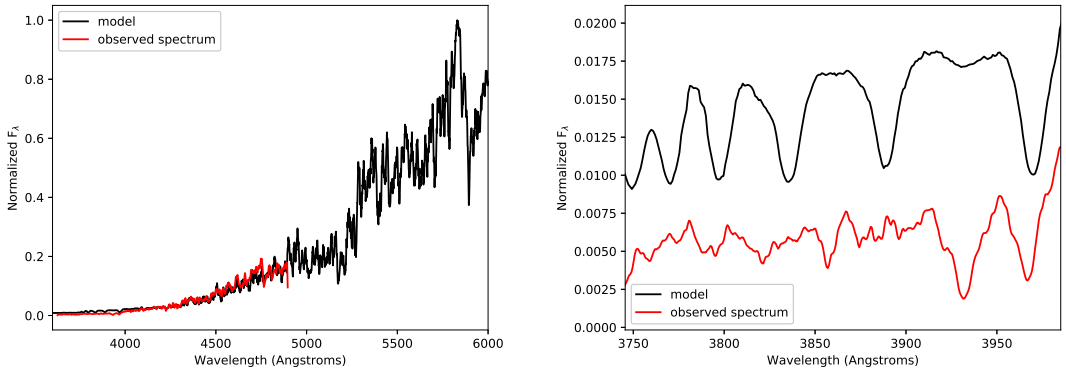

Figure 2.7 - Observed spectrum of BD+39 4208 a 3600 K M3I compared with a cool B dwarf model with Balmer lines. Balmer lines are not visible in the observed spectrum and by comparing them to a spectrum with a similar S/N that contains Balmer lines it is clear that if the star had a B star companion we would have detected the Balmer lines and thus the companion. © AAS. Reproduced with permission from Neugent et al. (2018a).

2.5.1 Synthetic Photometry from Models

To investigate this we used our set of ∼25,000 binary model spectra and synthetic photometry. To simulate photometry of our spectral models we used the Johnson-Cousins filter curves (Johnson & Morgan, 1953; Cousins, 1976) along with the zero-points from Bessell et al. (1998) and bandpasses from Bessell (1990). We calculated U,B,V,R and I photometry. To best represent the combination of blue and red spectra, we plotted our bluest colors (U-B) versus our reddest colors (R-I) in Figure 2.8. The figure on the left shows synthetic photometry from single blue stars, single red stars, and the combined spectra. Note that the composite spectra (black) all fall in a single region in this color-color space. The pastel-colored stars on the diagram and plots below show example combined spectra that occupy different regions within color-color space. They all show evidence of a B star's Balmer lines as well as a RSG's TiO bands, with varying strengths depending on where they fall within the black "composite spectra" region. Spectra near the red models (yellow star on plot)

unsurprisingly show more red features than the spectra near the blue models (green star) which show more blue features.

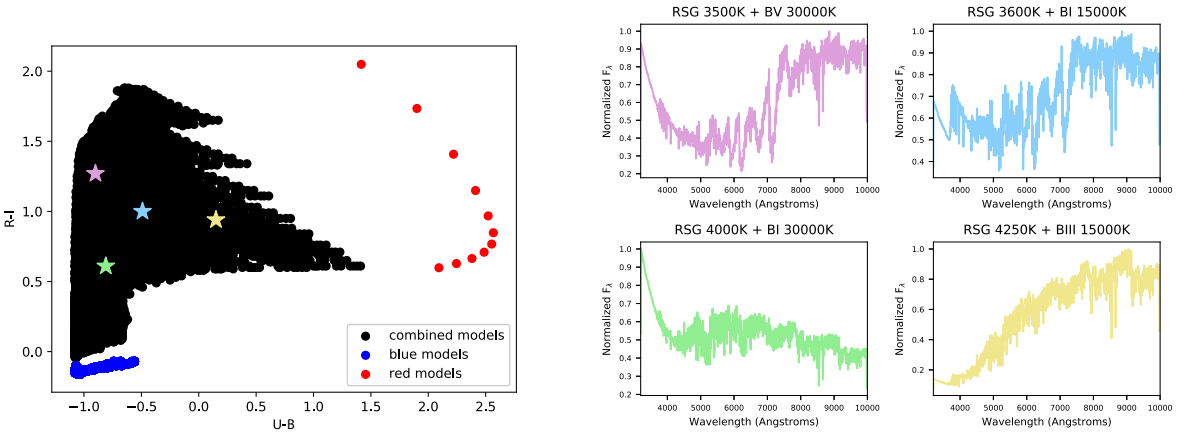

Figure 2.8 - Synthetic Photometry of 25,000 models. Blue points represent the B-type star models. Red points represent the RSG models. Black points represent the photometry of the combined synthetic spectra. The pastel-colored stars show example spectra from different regions within the color-color space. Notice that all combined spectra show examples of the Balmer lines as well as RSG-like spectral components. Depending on where the example falls within the composite spectra region, the Balmer lines will be more or less visible. For example, spectra near the red models (yellow star) show more red features than the spectra near the blue models (green star). © AAS. Reproduced with permission from Neugent et al. (2018a).

2.5.2 Comparisons with Observed Spectra

We next wanted to see how well our synthetic photometry matched with the photometry of our observed MC RSG sample discussed in Chapter 2.4.1. While we could determine colors based on the spectroscopy, we were limited by the poor quality of the flux calibrations. The MC data were taken using the Anglo-Australian Telescope's multi-fiber fed spectrograph, 2dF+AAOmega. Flux calibration of fiber instruments is notoriously difficult due to differ-

ences in the sensitivity function from one fiber to another (Fabricant et al., 2008; Massey & Hanson, 2013). The fluxing of AAOmega spectra was based on an observation of one spectrophotometric standard taken through a single fiber on a different night than the science data. While the spectral energy distribution looks reasonable for some of the data, it is clearly wrong for others. Thus, we were unsure of any colors derived from spectroscopy. In addition, the spectra did not extend as far in the blue as all of the U band, nor as far into the red as all I band. Thus, we were unwilling to rely on colors derived from the spectroscopic data.

Figure 2.9 shows the result of plotting U-B vs. R-I of the observed MC RSGs on top of the BSTAR06 and MARCS model's synthetic photometry. Only the stars with U, B and R magnitudes from Massey (2002) and the I magnitudes from Zaritsky et al. (2002) (SMC) or Zaritsky et al. (2004) (LMC) have been plotted. As discussed earlier, of the 311 SMC stars and 287 LMC stars, 25 stars (14 LMC and 11 SMC) had clear upper Balmer lines in their spectra. In the figure, the 25 stars with observed Balmer lines are within the composite spectra region (with the exception of a few that fall below the region). There is some contamination with non-Balmer-lined RSGs but this contamination is minimal. Most of these spectra show an up-turn in the blue which could be due to either bad photometry, poor flux calibrations, or the physical explanation of possible UV excess (Massey et al., 2005), such as with R Coronae Borealis stars (Hecht et al., 1998).

Note that very few of the green points that represent the Magellanic Cloud photometry of single RSGs overlap with the MARCS model's red points. We believe this is due to a failure of the MARCS models to accurately reproduce the observed spectrum in the blue. This was previously found by Massey et al. (2005) when looking at the reddening of RSGs. Because the blue MARCS spectrum is somewhat too weak it allows the BSTAR06 models to dominate the blue spectrum earlier than they should. Thus, the upper Balmer lines become visible within the synthetic spectrum before they would in an observed spectrum. This effect does not influence our results negatively. Instead, it simply means that the synthetic photometry we derived from the combined models for our RSG+B binary systems is likely

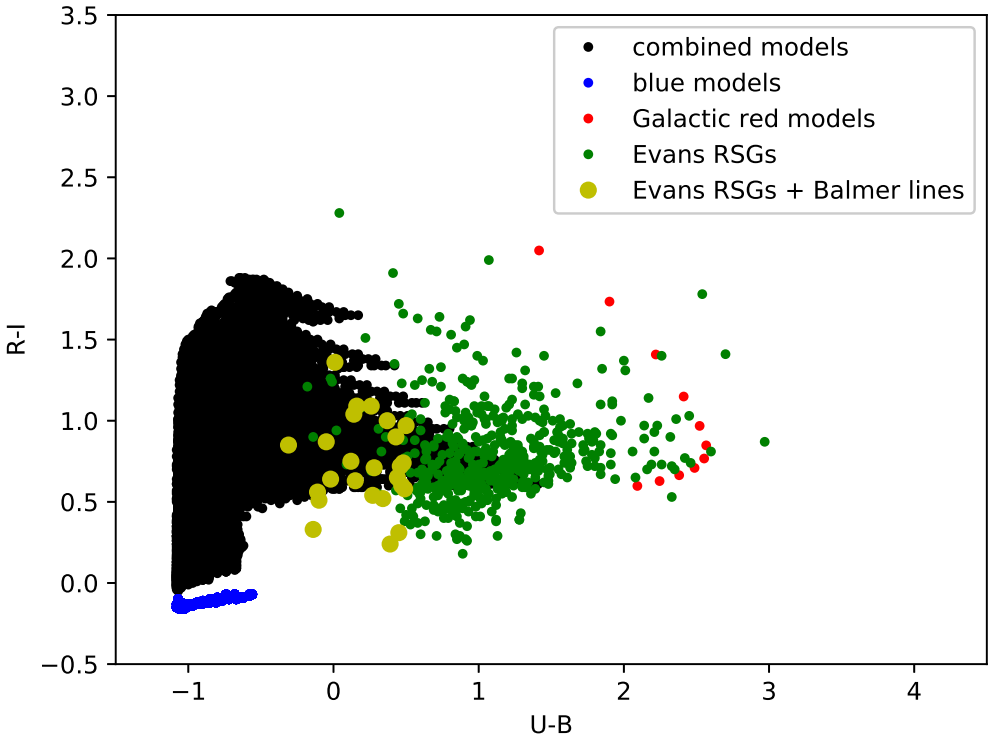

Figure 2.9 - Photometry of confirmed RSGs plotted alongside synthetic photometry. Of the ∼600 stars observed by Evans et al. (in prep), 25 of them (yellow dots) showed evidence of Balmer lines while the rest (green dots) did not. For the most part, these yellow dots fall within the composite spectra region of the photometry from the combined synthetic spectra. Photometric errors are around 0.05 mag in each bandpass and thus smaller than the point sizes. © AAS. Reproduced with permission from Neugent et al. (2018a).

to have a small amount of excess blue light in the blue. This means that the region in color-color space where we expect to find RSG+B binaries should be shifted a bit to the redder side (higher U-B values) and thus we expect to find fewer observed RSG+B binaries with low U-B values (U-B less than -0.5). As will be discussed below, we later tested this observationally and found this to be the case.

We were a little concerned about comparing apples to oranges in terms of metallicities. All of the models were computed with solar metallicities ($Z = Z_{\odot}$) while the LMC and SMC have metallicities of $0.5Z_{\odot}$ and $0.27Z_{\odot}$, respectively (Russell & Dopita, 1990). Figure 2.10 shows synthetic photometry from the MARCS RSG models plotted for two different metallicities (solar, and SMC). As you can see, shifts in the photometry due to metallicity are small. We additionally re-ran the synthetic models using BSTAR06 and the MARCS models with a metallicity of $0.25Z_{\odot}$ (SMC-like) and found the result shown in Figure 2.10. While there is some difference between the synthetic photometry with solar and SMC metallicity, the changes are minor and will not play any role in changing the photometric criteria.

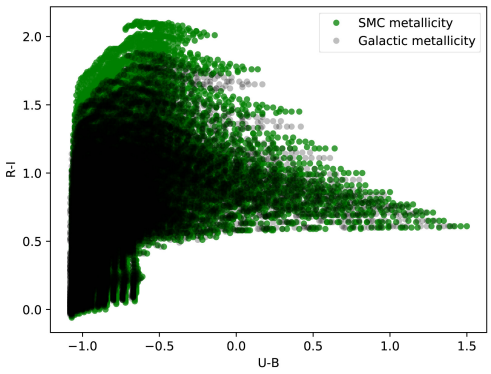

Figure 2.10 - Synthetic photometry of models with Galactic and SMC metallicities. Changing the metallicity of the synthetic models made only small changes to the overall shape of the combined spectra region in color-color space. Therefore we can use the photometric cutoffs for stars of all metallicities. © AAS. Reproduced with permission from Neugent et al. (2018a).

At this point, we had determined that RSGs in stellar binary systems will primarily have B-type companions as well as how to photometrically and spectroscopically identify such systems. Next, we went looking for these systems in M31 and M33 and then attempted to characterize the B-type companions.

Chapter 3

CHARACTERIZING B-TYPE COMPANIONS

As the last chapter showed, RSGs in stellar binary systems will primarily have B-type companions. Photometrically, these binary RSGs will appear different from single RSGs because they will have excess flux in the blue. This allows us to create a candidate list of binary RSGs by looking for stellar sources with the appropriate colors, as determined by synthetic photometry of RSG binary systems.

3.1 Spectroscopically Confirming RSG Binaries in M31 and M33

3.1.1 Photometric Selection

Using the synthetic photometry described in the previous chapter, we were next able to define a list of U-B and R-I photometric cutoffs where we believe RSGs with B star companions should fall on a color-color plot. This region is marked in red in Figure 3.1. B stars and RSGs in M31 and M33 as confirmed by the Local Group Galaxy Survey (Massey et al., 2006) (LGGS) are plotted as well. The triangle-shaped photometric cutoffs were selected to remove as many B and RSG stars as possible, though there is still a small amount of contamination.

We also investigated contamination from other spectral types and reddening. Figure 3.2 shows photometry from the Kurucz models (Castelli et al., 1997). These model atmospheres span all spectral types with a large range in effective temperatures and surface gravities. We chose a model that represented each spectral type and luminosity class and plotted their colors on the U-B vs. R-I plot. As is shown in the figure, none of these spectral types fall within the selected region (or within the composite spectra region in general) and thus contamination by stars with other spectral types should not be an issue. Reddening should also not be a problem. Figure 3.2 shows an $A_V = 1$ mag reddening vector. This simply

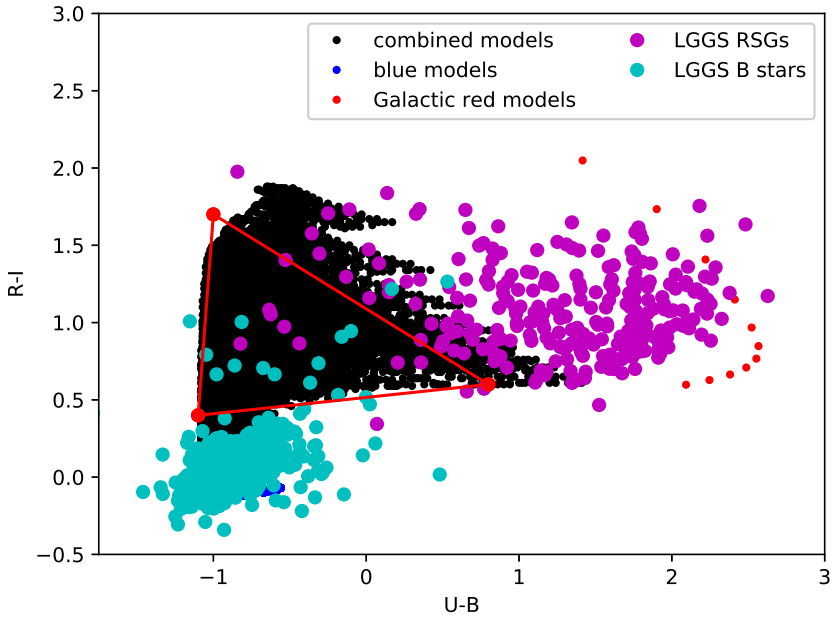

Figure 3.1 - M31 and M33 LGGS B stars and RSGs plotted with the photometrically selected cutoff region. The blue points are the single B star models and the red points are the single MARCS RSG models. The black points are then the combined models using the Galactic metallicity RSGs. The cyan points are the M31 and M33 LGGS B stars while the magenta points are the M31 and M33 LGGS RSGs. To create as little contamination as possible, we have selected the triangle denoted by the red lines as the area encompassing possible RSG+B star binaries in color-color space. The vertices of the points in U-B vs. R-I color space are (-1.1,0.4), (0.8,0.6), and (-1,1.7). Errors on photometry are less than 0.05 mag in each bandpass and thus smaller than the point sizes. © AAS. Reproduced with permission from Neugent et al. (2019).

pushes all of the stars slightly up and to the right. Given this reddening vector, none of the Kurucz models will enter the photometrically selected region.

Given these parameters we were able to build a candidate list of potential RSG+B star binaries for stars within the LGGS, specifically within M31 and M33. To do this, we filtered

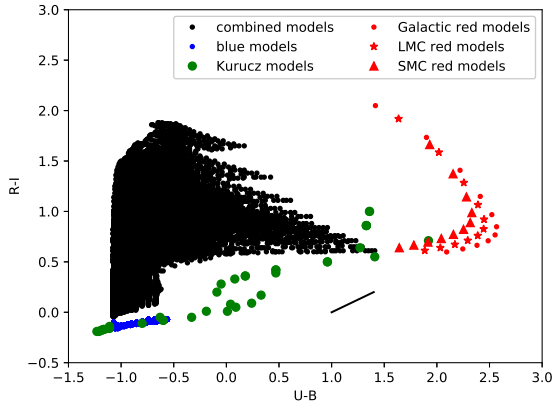

Figure 3.2 - Possible stellar contaminants. Blue, Black and Red points are same as in Figure 3.1. We have additionally plotted the Kurucz models (green circles) for a variety of spectral types showing that we will not have contamination from other types of stars. Finally, we have plotted the reddening vector for $A_V = 1$ as a black line showing that the reddened Kurucz models will not enter the region of composite spectra. © AAS. Reproduced with permission from Neugent et al. (2019).

through the 370,000 stars in M31 and 150,000 stars in M33. We were first concerned about contamination by red dwarfs. We started with a magnitude cutoff of V=20 to limit the search to the brighter stars (more likely to be RSGs). We then used a color-color diagram to pick out the red dwarfs from the RSGs using U-B vs. U-R color cuts. Since we want to eventually get spectra of these stars, we next restricted ourselves to only the isolated stars (as marked in the LGGS). Finally, we weeded out foreground stars by looking for potential matches with *Gaia* (Gaia Collaboration et al., 2018) and restricted the stars to distances less than 10kpc. At this point we were left with 138 potential binaries in M31 and 142 in M33.

We additionally checked the M31 candidates for signal within the UV and NIR. For this we relied on the Panchromatic Hubble Andromeda Treasury (PHAT) dataset (Dalcanton et al., 2012). As opposed to sorting through the photometric catalogs, we instead downloaded the image files and searched for the UV (F275W) and NIR (F160W) signatures visually. In all 138 cases, these stars were visually bright in both the NIR and UV suggesting a SED much like what we have predicted.

3.1.2 Observations and Reductions

To observe as many of the 280 stars as possible, we relied on the multi-object fiber-fed spectrograph, Hectospec, (Fabricant et al., 2005) on the 6.5-m MMT. Its large field of view (1 degree in diameter) was well matched to our M31 and M33 survey areas. We were assigned 2.5 nights of dark time in Fall 2018 through the Arizona Time Allocation Committee in order to study several dozen WR+O binaries in M31 and M33, but since Hectospec has 300 fibers, we were able to piggyback the RSG binarity project onto this time using unused fibers. Due to poor weather and instrument problems, only a single M31 and a single M33 configuration were observed. The M31 field was observed on UT 2018 September 14 while the M33 field was observed on UT 2018 October 6, both with clear sky conditions. The data were taken with the 270 line mm^{-1} grating resulting in spectral coverage from 3700 - 9000 Å, ideal coverage for both the upper Balmer lines (3700Å - 4000Å) originating from the B-type stars and the TiO bands (upwards of 6000Å) of the RSGs. The 250 μm fibers resulted in a spectral resolution of 6Å. Exposures were 3×3000 seconds. Reductions were carried out using the version 2.0 of the Hectospec REDuction (HSRED) code[1] which is similar to the SDSS spectral pipeline.

3.1.3 New Binaries

Out of the 280 candidates in M31 and M33, 149 were observed. Of these, 63 were confirmed as newly discovered RSG+B star binaries. Their locations in U-B vs. R-I color space are plotted in Figure 3.3 as yellow circles. (It should be noted that because Hectospec is a mult-fiber instrument, flux calibration is inherently difficult because each fiber will have a different transmission curve and hence be dependent upon the accuracy of the flat field correction (Fabricant et al., 2008). Thus, when plotting these stars on a color-color plot we relied on their LGGS colors as opposed to photometry derived from the spectra.) Note that they span the entire range of color space where we expected to find RSG binaries.

[1]See, `http://www.mmto.org/hsred-reduction-pipeline/`.

Representative examples of confirmed binary RSGs within the observed color-color space are shown in Figure 3.4.

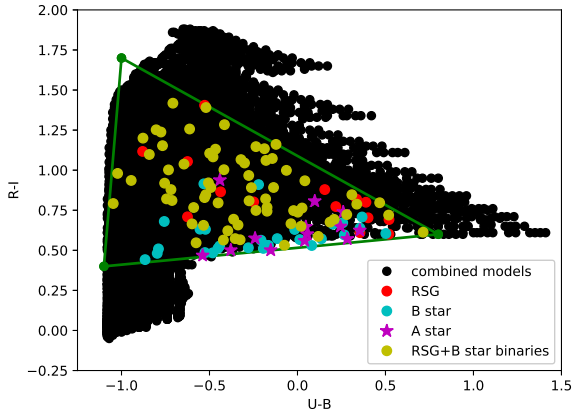

Figure 3.3 - Location of observed RSG+B star binary candidates in R-I vs. U-B color-color space. The confirmed RSG+B star binaries showing both TiO bands and upper Balmer lines are shown as yellow dots. The RSGs with just TiO bands are shown as red dots. The B stars with just upper Balmer lines are shown as blue dots. The A stars are shown as magenta stars. The outline of our photometric cutoffs is shown as a green triangle. Note that the RSG+B star binaries are spread without the entire region in color-color space while the bluer B and A type stars are, for the most part, confined to the low R-I values. Some of the single RSGs are closer to the redder portion in color-color space but half of the sample shows evidence of a blue component in the spectrum. © AAS. Reproduced with permission from Neugent et al. (2019).

The coordinates, magnitudes and general classifications of the stars discussed below are listed in Table 3.1.

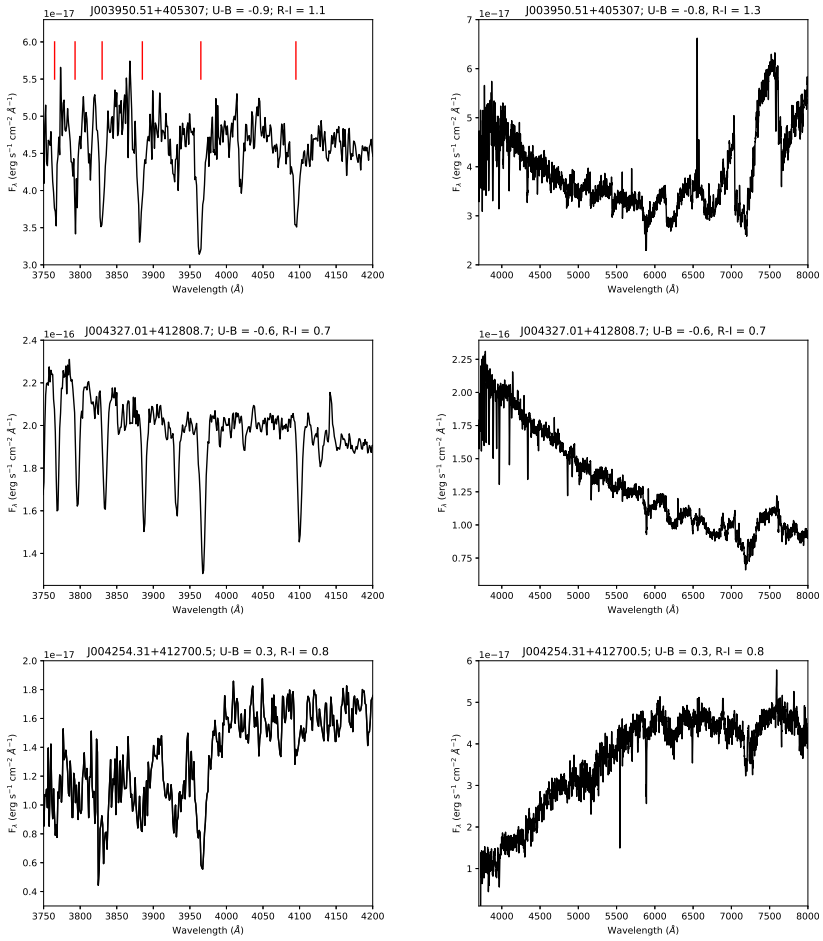

Figure 3.4 - Three representative examples of confirmed RSG+B star binaries. For all three spectra, the entire spectral range (showing both the upper Balmer lines and TiO bands) is shown on the right and an inset of the upper Balmer lines is shown on the left with the Balmer lines marked by red vertical lines. The U-B and R-I values are shown in the title to give a sense of where these stars are located on the color-color plot in Figure 3.3. In general, the top star, J003950.51+405307 is located in the upper portion of the triangle. The middle star, J004327.01+412807.7 is located in the bottom left of the triangle and the bottom star, J004254.31+412700.5 is located in the bottom right of the triangle. Notice how the bluer stars have stronger upper Balmer lines while the redder stars have stronger TiO bands.

Table 3.1. Coordinates and Magnitudes of Classified M31 and M33 Stars

LGGS ID	α_{2000}	δ_{2000}	V	$B-V$	$U-B$	$R-I$	Classification
J003940.67+405125.4	00 39 40.66	+40 51 25.3	19.089	1.849	-0.122	1.161	RSG+B binary
J003942.08+405221.4	00 39 42.07	+40 52 21.3	18.880	0.536	-0.576	0.547	RSG+B binary
J003950.51+405307.4	00 39 50.50	+40 53 07.3	18.985	0.485	-0.803	1.252	RSG+B binary
J003955.78+410426.7	00 39 55.77	+41 04 26.6	19.847	0.602	0.257	0.672	B-type star
J004021.42+404035.7	00 40 21.41	+40 40 35.6	19.685	0.812	-0.396	0.622	RSG+B binary
J004024.49+405418.0	00 40 24.48	+40 54 17.9	19.978	0.526	-0.539	0.468	A-type star
J004024.87+404900.9	00 40 24.86	+40 49 00.8	19.999	1.250	-0.241	0.575	A-type star
J004030.12+404502.3	00 40 30.11	+40 45 02.2	19.916	0.423	-0.744	0.821	RSG+B binary
J004030.95+403923.5	00 40 30.94	+40 39 23.4	18.587	0.871	-0.016	0.630	B-type star
J004032.98+404102.8	00 40 32.97	+40 41 02.7	19.702	0.238	-0.914	0.409	high-mass symbiotic
J004033.98+404429.9	00 40 33.97	+40 44 29.8	18.963	0.998	0.002	0.738	RSG+B binary
J004034.80+404328.6	00 40 34.79	+40 43 28.5	19.644	0.701	-0.554	0.632	B-type star
J004036.31+405058.0	00 40 36.30	+40 50 57.9	19.922	0.996	0.013	0.567	B-type star
J004043.78+404335.3	00 40 43.77	+40 43 35.2	19.830	0.186	-0.866	0.442	B-type star
J004053.01+404356.3	00 40 53.00	+40 43 56.2	19.738	0.778	-0.165	0.531	B-type star
J004059.48+410229.4	00 40 59.47	+41 02 29.3	19.234	0.827	-0.499	1.105	RSG+B binary
J004100.50+410432.5	00 41 00.49	+41 04 32.4	19.917	0.726	-0.279	0.516	B-type star
J004101.95+410911.4	00 41 01.94	+41 09 11.3	19.878	1.456	0.520	0.692	RSG
J004106.51+404848.8	00 41 06.50	+40 48 48.7	19.950	1.131	-0.418	1.003	RSG+B binary
J004115.88+404011.4	00 41 15.87	+40 40 11.3	19.680	1.407	-0.221	0.910	B-type star
J004117.43+410837.5	00 41 17.42	+41 08 37.4	19.346	1.215	-0.466	1.131	RSG+B binary
J004134.79+411418.1	00 41 34.78	+41 14 18.0	19.907	1.076	-0.037	0.666	RSG+B binary
J004136.62+410018.3	00 41 36.61	+41 00 18.2	19.831	1.454	0.519	0.601	RSG
J004139.49+404033.4	00 41 39.48	+40 40 33.3	19.482	0.335	-0.379	0.501	A-type star
J004143.13+411734.9	00 41 43.12	+41 17 34.8	19.907	0.701	-0.207	0.563	B-type star
J004145.25+411229.4	00 41 45.24	+41 12 29.3	19.446	0.288	-0.074	0.532	RSG+B binary
J004149.73+405300.1	00 41 49.72	+40 53 00.0	19.537	0.509	-0.492	0.892	RSG+B binary
J004151.42+411804.7	00 41 51.41	+41 18 04.6	19.992	0.776	-0.755	0.919	RSG+B binary
J004153.05+405235.7	00 41 53.04	+40 52 35.6	19.714	0.495	0.244	0.649	A-type star
J004158.62+405338.6	00 41 58.61	+40 53 38.5	19.440	0.713	-0.767	1.153	RSG+B binary
J004158.87+405316.7	00 41 58.86	+40 53 16.6	18.416	0.743	-0.184	0.532	B-type star
J004204.77+411340.8	00 42 04.76	+41 13 40.7	19.799	1.158	0.518	0.720	RSG
J004205.41+412826.0	00 42 05.40	+41 28 25.9	18.700	0.137	-0.482	0.484	B-type star
J004205.57+413345.8	00 42 05.56	+41 33 45.7	19.633	0.880	-0.363	0.694	RSG+B binary
J004209.69+411340.7	00 42 09.68	+41 13 40.6	19.605	0.517	0.208	0.693	RSG+B binary

Table 3.1 (cont'd)

LGGS ID	α_{2000}	δ_{2000}	V	$B-V$	$U-B$	$R-I$	Classification
J004211.64+412341.2	00 42 11.63	+41 23 41.1	19.944	0.809	0.098	0.807	A-type star
J004217.21+411743.2	00 42 17.20	+41 17 43.1	18.421	0.533	-0.152	0.501	A-type star
J004229.89+412034.6	00 42 29.88	+41 20 34.5	19.913	0.218	-0.790	0.509	B-type star
J004238.73+405349.9	00 42 38.72	+40 53 49.8	19.692	1.234	-0.143	1.073	RSG+B binary
J004239.82+412054.7	00 42 39.81	+41 20 54.6	19.730	1.246	0.714	0.613	RSG
J004241.27+413156.8	00 42 41.26	+41 31 56.7	19.397	0.883	0.055	0.601	A-type star
J004243.97+411344.9	00 42 43.96	+41 13 44.8	19.583	0.511	0.218	0.773	RSG+HII
J004246.20+411232.8	00 42 46.19	+41 12 32.7	19.692	0.385	-0.625	0.709	RSG
J004246.22+411309.1	00 42 46.21	+41 13 09.0	19.908	0.642	0.389	0.800	RSG
J004247.66+405810.6	00 42 47.65	+40 58 10.5	19.262	0.576	0.354	0.624	A-type star
J004253.28+411246.4	00 42 53.27	+41 12 46.3	19.673	0.336	0.118	0.587	RSG+B binary
J004253.29+411010.8	00 42 53.28	+41 10 10.7	19.898	0.960	-0.173	0.768	RSG+B binary
J004254.31+412700.5	00 42 54.30	+41 27 00.4	19.268	1.439	0.337	0.788	RSG+B binary
J004256.79+410230.5	00 42 56.78	+41 02 30.4	19.878	0.755	-0.452	0.512	B-type star
J004259.35+410211.0	00 42 59.34	+41 02 10.9	19.619	0.899	-0.115	0.573	B-type star
J004313.97+411119.7	00 43 13.96	+41 11 19.6	19.167	0.688	-0.441	0.938	A-type star
J004314.06+410844.9	00 43 14.05	+41 08 44.8	19.485	0.523	0.260	0.739	A-type star
J004327.01+412808.7	00 43 27.00	+41 28 08.6	17.668	0.224	-0.599	0.665	RSG+B binary
J004328.81+411854.9	00 43 28.80	+41 18 54.8	19.377	0.807	-0.713	0.811	RSG+B binary
J004332.50+412205.7	00 43 32.49	+41 22 05.6	19.708	0.361	0.136	0.572	B-type star
J004338.56+412511.6	00 43 38.55	+41 25 11.5	19.936	1.107	0.355	0.610	RSG
J004339.23+412443.5	00 43 39.22	+41 24 43.4	17.809	1.201	0.502	0.605	B-type star
J004344.53+411104.6	00 43 44.52	+41 11 04.5	19.753	0.996	0.042	0.934	RSG+B binary
J004345.11+410946.7	00 43 45.10	+41 09 46.6	19.952	0.542	0.283	0.571	A-type star
J004345.75+411451.7	00 43 45.74	+41 14 51.6	19.829	1.086	0.202	0.663	B-type star
J004348.91+411629.2	00 43 48.90	+41 16 29.1	19.794	0.793	-0.354	0.573	RSG+B binary
J004351.83+411431.7	00 43 51.82	+41 14 31.6	19.337	0.759	-0.326	0.566	RSG+B binary
J004352.80+410957.9	00 43 52.79	+41 09 57.8	18.098	1.219	-0.532	0.915	B-type star
J004359.63+411853.8	00 43 59.62	+41 18 53.7	19.804	0.798	-0.249	0.802	RSG
J004405.80+411937.4	00 44 05.79	+41 19 37.3	19.726	0.691	-0.181	0.821	RSG+B binary
J004410.28+411757.6	00 44 10.27	+41 17 57.5	19.570	1.460	0.309	0.847	RSG+B binary
J004428.15+411002.0	00 44 28.14	+41 10 01.9	19.731	0.428	0.185	0.676	RSG+B binary
J013209.23+302614.8	01 32 09.20	+30 26 14.7	19.873	1.760	0.401	0.703	RSG
J013224.33+303155.5	01 32 24.30	+30 31 55.4	19.547	1.808	-0.437	0.865	RSG
J013232.81+302855.7	01 32 32.78	+30 28 55.6	19.794	0.705	-0.523	0.631	B-type star

Table 3.1 (cont'd)

LGGS ID	α_{2000}	δ_{2000}	V	$B-V$	$U-B$	$R-I$	Classification
J013250.80+303507.6	01 32 50.77	+30 35 07.5	19.940	0.468	-1.047	0.792	RSG+B binary
J013253.33+303943.7	01 32 53.30	+30 39 43.6	19.889	1.643	0.467	0.797	RSG
J013254.01+303858.0	01 32 53.98	+30 38 57.9	18.649	0.448	-0.534	0.656	RSG+B binary
J013254.95+302411.1	01 32 54.92	+30 24 11.0	19.150	0.589	-0.719	0.879	RSG+B binary
J013256.23+302752.1	01 32 56.20	+30 27 52.0	19.293	1.012	-0.521	0.847	RSG+B binary
J013256.84+302347.9	01 32 56.81	+30 23 47.8	19.327	0.712	-0.338	0.658	RSG+B binary
J013259.82+303231.5	01 32 59.79	+30 32 31.4	19.799	1.306	-0.528	0.829	RSG+B binary
J013301.02+303500.7	01 33 00.99	+30 35 00.6	19.108	1.238	-0.321	1.066	RSG+B binary
J013303.54+303201.2	01 33 03.51	+30 32 01.1	18.878	2.177	-0.528	1.405	RSG
J013306.83+303039.5	01 33 06.80	+30 30 39.4	19.600	1.357	-0.179	1.061	RSG+B binary
J013309.52+303410.7	01 33 09.49	+30 34 10.6	19.963	0.206	0.041	0.560	A-type star
J013312.20+304849.4	01 33 12.17	+30 48 49.3	18.871	2.097	-0.625	1.054	RSG
J013314.45+302615.2	01 33 14.42	+30 26 15.1	19.832	1.232	-0.262	0.891	RSG+B binary
J013315.30+302248.3	01 33 15.27	+30 22 48.2	19.514	1.032	-0.451	0.796	RSG+B binary
J013320.17+304655.0	01 33 20.14	+30 46 54.9	19.827	1.302	0.026	0.764	RSG+B binary
J013323.19+304016.2	01 33 23.16	+30 40 16.1	19.937	0.711	-0.236	0.749	RSG+B binary
J013323.64+302836.8	01 33 23.61	+30 28 36.7	19.905	0.742	-0.590	0.767	RSG+B binary
J013324.56+304908.3	01 33 24.53	+30 49 08.2	19.923	1.022	-0.063	0.999	RSG+B binary
J013328.78+303002.5	01 33 28.75	+30 30 02.4	19.889	0.290	-0.442	0.527	B-type star
J013339.51+304316.6	01 33 39.48	+30 43 16.5	18.875	0.382	-0.878	1.200	RSG+B binary
J013342.45+304237.2	01 33 42.42	+30 42 37.1	19.890	0.952	-0.136	0.892	RSG+B binary
J013342.55+305309.6	01 33 42.52	+30 53 09.5	18.985	0.750	-0.880	1.117	RSG
J013343.22+303547.9	01 33 43.19	+30 35 47.8	18.750	0.411	-0.945	0.936	RSG+B binary
J013345.91+303915.6	01 33 45.88	+30 39 15.5	19.357	0.113	-0.757	0.680	B-type star
J013347.51+304154.9	01 33 47.48	+30 41 54.8	19.972	1.769	-0.708	1.418	RSG+B binary
J013347.82+304324.9	01 33 47.79	+30 43 24.8	18.436	0.237	-0.421	0.564	RSG+B binary
J013349.94+302928.8	01 33 49.91	+30 29 28.7	18.102	0.983	-0.842	1.098	RSG+B binary
J013351.13+303922.0	01 33 51.10	+30 39 21.9	19.897	0.242	-0.797	0.481	B-type star
J013352.45+305425.6	01 33 52.42	+30 54 25.5	18.830	1.466	0.280	0.723	RSG+B binary
J013355.62+304116.6	01 33 55.59	+30 41 16.5	19.916	1.217	-0.236	1.147	RSG+B binary
J013356.09+303834.5	01 33 56.06	+30 38 34.4	19.376	0.686	-0.613	1.257	RSG+B binary
J013358.33+302216.5	01 33 58.30	+30 22 16.4	19.698	1.138	-0.173	0.744	RSG+B binary
J013358.53+304754.7	01 33 58.50	+30 47 54.6	19.971	0.923	-0.506	0.921	RSG+B binary
J013359.54+303200.4	01 33 59.51	+30 32 00.3	19.733	0.575	-0.480	1.083	RSG+B binary
J013359.67+304940.2	01 33 59.64	+30 49 40.1	19.869	0.109	-0.526	0.486	B-type star

Table 3.1 (cont'd)

LGGS ID	α_{2000}	δ_{2000}	V	$B-V$	$U-B$	$R-I$	Classification
J013401.67+304050.7	01 34 01.64	+30 40 50.6	19.935	1.687	-0.301	1.045	RSG+B binary
J013402.58+304310.1	01 34 02.55	+30 43 10.0	19.265	0.613	-0.733	1.002	RSG+B binary
J013403.54+304201.9	01 34 03.51	+30 42 01.8	19.414	0.883	-0.194	0.512	B-type star
J013403.85+303911.0	01 34 03.82	+30 39 10.9	19.965	1.477	0.367	0.708	B-type star
J013404.04+304804.7	01 34 04.01	+30 48 04.6	17.817	1.246	0.355	0.639	B-type star
J013404.56+302459.9	01 34 04.53	+30 24 59.8	19.820	0.780	-0.022	0.748	RSG+B binary
J013405.62+304142.8	01 34 05.59	+30 41 42.7	19.994	0.855	-0.275	0.809	RSG+B binary
J013408.10+304616.3	01 34 08.07	+30 46 16.2	19.971	0.875	0.020	0.650	RSG+B binary
J013408.17+304813.6	01 34 08.14	+30 48 13.5	19.719	0.308	0.047	0.647	A-type star
J013409.66+304721.9	01 34 09.63	+30 47 21.8	19.578	0.569	0.266	0.596	B-type star
J013413.98+302759.0	01 34 13.95	+30 27 58.9	18.592	1.034	-0.188	1.134	RSG+B binary
J013413.99+305035.5	01 34 13.96	+30 50 35.4	19.888	0.386	0.081	0.530	B-type star
J013414.05+310450.4	01 34 14.02	+31 04 50.3	19.856	1.294	0.336	0.819	RSG
J013415.32+303804.3	01 34 15.29	+30 38 04.2	18.916	0.756	-0.776	1.238	RSG+B binary
J013424.81+310456.4	01 34 24.78	+31 04 56.3	19.045	1.867	0.155	0.879	RSG
J013431.25+304538.8	01 34 31.22	+30 45 38.7	19.023	0.216	-1.022	0.980	RSG+B binary
J013431.85+305400.8	01 34 31.82	+30 54 00.7	19.525	0.498	-0.645	1.038	RSG+B binary
J013436.97+304514.9	01 34 36.94	+30 45 14.8	19.786	1.273	-0.415	1.284	RSG+B binary
J013439.43+304551.4	01 34 39.40	+30 45 51.3	19.193	1.596	-0.520	1.391	RSG+B binary
J013448.91+303140.4	01 34 48.88	+30 31 40.3	19.961	0.990	-0.277	0.967	RSG+B binary

Note. — All photometry from Massey et al. 2006.

3.1.4 Contaminants

While 42% (63/149) of the observed stars were RSG+B star binary systems, the remaining 58% were contaminants. Below we detail the types of contaminants including the single RSGs, blue stars, and other interesting stars. Within each section we discuss how to remove such contaminates in future surveys.

Potentially Single RSGs

As is shown in Figure 3.3, 11% (17/149) of the observed candidates showed strong TiO bands but no upper Balmer lines. However, a few of them show strong signal in the blue but no upper Balmer lines. This could be due to a few possibilities. The first is that there is a B-type star companion but the S/N simply isn't high enough to detect weak Balmer lines. Another possibility is that we are seeing the effects of dust scattering (similar to what is seen in normal reflection nebula). Many RSGs have extra extinction compared to their OB star neighbors; these stars also show upturns in their UV spectra (Massey et al., 2005; Levesque et al., 2005). As mentioned previously, RSGs have high mass-loss rates. As the mass is expelled, the dust grains absorb the red light while reflecting the blue light (Jura & Jacoby, 1976). Thus, some RSGs show what appears to be a blue reflection nebula. This has been seen in such RSGs as VY CMa and μ Cep (Shenoy et al., 2016). Higher resolution and UV data is needed to either confirm or deny the existence of such a feature.

Given that the majority of these TiO-band spectra show upturns in the blue, we wouldn't exactly call these contaminates. Thus we would rather get additional data to either confirm or deny the presence of a binary companion or reflection nebula as opposed to removing them from our list of candidates.

Blue Stars

There were additionally quite a few stars that showed strong Balmer lines but no TiO bands. These stars comprised 28% (41/149) of the sample. The majority of these stars were B-type stars ($28/41 = 68\%$) but there were a few A-type stars as well ($13/41 = 32\%$). Their locations in color-color space are shown in Figure 3.3 as cyan dots (B stars) and magenta stars (A stars). Note that the majority of them are clustered around the lower-most R-I colors (R-I ~ 0.5) but across a wide range of U-B color-space. Since we are preferentially finding single blue (B and A) stars at low R-I colors, we believe we have adequately sampled that region of color-space for binary RSGs and we would not find any more RSG+B star binaries at

lower R-I colors. With the exception of two of the A-type stars, the rest were pushed into our region of interest due to high reddening ($B-V>0.5$) values as determined from LGGS photometry (Massey et al., 2006).

Within a small region of color-color space (at low R-I colors), there are 27 A and B-type stars and only 2 RSG+B star binaries. So, if we are interested in completeness, it is still necessary to sample this region. However, 93% of this region was contaminated by A and B-type stars. To maximize the number of RSG+B star binaries found from the minimum number of spectroscopic follow-up observations, this region should be sampled last.

Other Contaminants

Although our program was highly successful in identifying RSG with early-type companions, there were invariably some "losers." Twenty-four spectra fell into this category, an interesting hodgepodge. About half of these are likely foreground stars and are of no further interest here. Two others proved to be RSGs that were located in regions of strong nebulosity. The remainder, however, proved quite interesting in their own right. Twelve objects turn out to be previously unknown background QSOs and galaxies, and is discussed in a short companion paper (Massey et al., 2019).

Removing this assortment of contaminants is quite difficult since they span the entire range of color-color space. However, some of them could have been removed using the original LGGS (Massey et al., 2006) images. The galaxies are not quite point sources on the images (although the QSOs are) and thus could have been eliminated by their fuzzy structure. But for the remaining point-sources, there is no easy way of removing them from the list of targets.

J004032.98+404102.8 - A Symbiotic RSG?

One contaminant star, J004032.98+404102.8, stands out in particular. Its spectrum is shown in Figure 3.5. We find Balmer emission with an extremely strong decrement, along with numerous low-excitation Fe lines, primarily Fe II. We were unable to find any forbidden Fe

lines, although the nebular lines [S II] $\lambda\lambda 6716, 31$ are weakly present, as is the [N II] $\lambda 6583$. Very weak [O III] $\lambda 5007$ may be present.

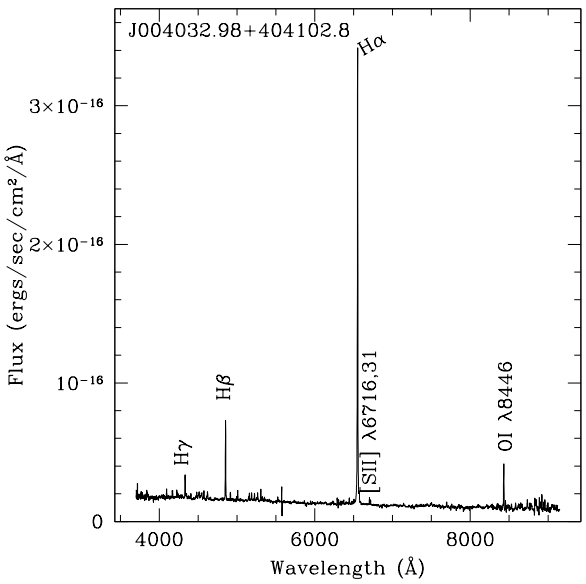

Figure 3.5 - The spectrum of J004032.98+404102.8. The weak, unlabeled lines below 5000Å are predominantly Fe II. © AAS. Reproduced with permission from Neugent et al. (2019).

What is the nature of this unusual find? We are indebted to our colleague Dr. Howard Bond for helping us answer this. The object was detected both by the *Swift* Ultraviolet / Optical Telescope (UVOT), and by the Wide-field Infrared Survey Explorer (WISE), indicating both hot and cool components. This is a classic description of symbiotic stars providing the first strong evidence that they consisted of a red giant and a white dwarf (see, e.g., Boyarchuk 1985). An inspection of the atlas of symbiotic stars by Munari & Zwitter (2002) reveals a near identical match between the optical spectrum of V3929 Sgr (their Fig. 75) and that of our M31 star.

However, there is still a mystery. J004032.98+404102.8 is clearly a member of M31, as its radial velocity (measured via the Balmer lines) is -543 ± 2 km s^{-1}, consistent with that expected given its location in M31's disk, -531 km s^{-1} using the assumptions laid out in Massey et al. (2009). Thus, the star has a high visual luminosity, $M_V \sim -5.1$. The cool components of symbiotic stars are typically M giants, or at most bright giants (see, e.g., Keyes & Preblich 2004); these should have absolute visual magnitudes near 0 (Cox, 2000).

A value of -5 is more typical of a red *super*giant.

Putting together these findings suggest that this may actually be another successful detection of a RSG binary, albeit in an unexpected form. We propose that this object is some sort of high-mass analog of a normal symbiotic star. In a normal symbiotic system, the red giant dumps material onto a white dwarf, and in the process creates an accretion disk. "D-type" symbiotics usually contain a Mira variable and are surrounded by optically thick dust, obscuring the donor star (Mikołajewska, 2007). Based upon the absolute magnitude, we suspect that this is a RSG+OB companion pair, with the matter transfer creating both the accretion disk and contributing to the obscuration of the donor star. The OB star is exciting some nebula emission, but high obscuration leads to a strong Balmer decrement and the near invisibility of the [O III] line. The Fe emission would presumably arise from the accretion disk. It would be worthwhile to monitor this star to see if its spectrum or brightness vary, as one finds with many symbiotics. Although it has been previously identified as a "miscellaneous" variable (V2285) by Mochejska et al. 1999, its amplitude is not much larger than the errors.

3.1.5 Understanding the Completeness of our Survey

The average S/N of our spectra around the upper Balmer lines (3700-4000Å) was 25 ± 9 per 2Å resolution. While this S/N is sufficient to detect the upper Balmer lines of most OB companions, in Chapter 2 we found that a S/N of $\sim$100 per 2Å resolution element in the blue was needed to detect the upper Balmer lines in the most extreme cases of a faint BV companion. Thus, in order to conclusively prove whether the RSG has a B star companion, we needed a much higher S/N than what we obtained. It should also be noted that the spectral resolution of the MMT data was 5Å and thus not adequate for detecting the weakest lined Balmer lines even with a high enough S/N. So, of the 14 RSGs that did not show upper Balmer lines, it cannot be ruled out that they have B star companions with weak upper Balmer lines. Data with a higher S/N and resolution are needed.

We also must consider the likelihood that RSG+B star binaries exist outside of the targeted search area within color-color space. This number is difficult to quantify and many

of our confirmed RSG+B star binaries fall on the dividing line as shown in Figure 3.3. Considering the increasing contamination of B and A stars near the lower values in R-I, we believe that region of color-color space has been adequately explored. However, we cannot rule out there being more RSG+B star binaries in the redder regions (hypothenuse of the triangle). Sadly, these systems are not rare. They are comprised of RSG + B star binaries where the Balmer lines are quite weak compared to the flux from the RSG. This most commonly occurs with a RSG + BV pair or a binary where the B star has high reddening and thus the Balmer lines have been slightly "filled in." Given the weakness of the Balmer lines in these spectra, we would need a higher S/N (much closer to ∼100, as discussed above) to detect such stars. At this point, the S/N and resolution requirements become almost prohibitive towards large-scale spectroscopic follow up and we may need to devise another method to identify such binaries. In Chapter 5, the RSG binary fraction is investigated in much greater detail and at that point, concrete completeness limits are discussed.

3.2 Newly Confirmed Small Magellanic Cloud RSG+B Star Binaries

In addition to our M31 and M33 observations, we obtained spectra of four RSG+B star binary candidates in the SMC. As was described in Chapter 2, 25 out of 598 previously observed RSGs in the Magellanic Clouds showed evidence of upper Balmer lines (the coordinates and magnitudes of these stars are listed in Table 3.2). Ten additional RSGs in the sample also showed potential upper Balmer absorption but had a S/N that were too low (around 20 per 2Å resolution) for this to be conclusive. We re-observed four of these low-S/N candidates that were chosen as a representative sample using the 6.5-m Magellan Echellette (MagE) on the Baade Magellan telescope at Las Campanas. We confirmed all four of them as RSG+B star binaries due to the presence of upper Balmer lines. We additionally made a very interesting discovery – the first known RSG+Be star binary!

Table 3.2. Coordinates and Magnitudes of Confirmed MC RSG+B Star Binaries

ID	α_{2000}	δ_{2000}	V	$U-B$	$V-B$
J00464984-7313525	00 46 49.84	-73 13 52.5	13.599	0.043	-1.313
J00513280-7205493	00 51 32.80	-72 05 49.3	13.096	-0.061	-1.238
J00522647-7245159	00 52 26.47	-72 45 15.9	12.496	-0.341	-1.348
J00531861-7242074	00 53 18.61	-72 42 07.4	13.486	0.549	-1.518
J00532528-7215376	00 53 25.28	-72 15 37.6	13.296	0.549	-1.448
J00532655-7212033	00 53 26.55	-72 12 03.3	13.700	0.847	-1.355
J00534451-7233192	00 53 44.51	-72 33 19.2	13.226	0.099	-1.238
J00535739-7313335	00 53 57.39	-73 13 33.5	13.879	0.193	-1.432
J00543483-7229512	00 54 34.83	-72 29 51.2	13.732	1.549	-1.754
J01014357-7238252	01 01 43.57	-72 38 25.2	13.076	-0.041	-1.288
J01023794-7235547	01 02 37.94	-72 35 54.7	13.376	0.109	-1.198
J01024076-7217173	01 02 40.76	-72 17 17.3	13.516	-0.071	-0.438
J01033730-7158448	01 03 37.30	-71 58 44.8	13.096	0.529	-1.388
J04595731-6748133	04 59 57.31	-67 48 13.3	13.176	-0.211	-0.888
J05030232-6847203	05 03 02.32	-68 47 20.3	13.612	-0.133	-1.097
J05043378-6806235	05 04 33.78	-68 06 23.5	13.536	-0.71	-0.754
J05065284-6841123	05 06 52.84	-68 41 12.3	14.469	-0.659	-0.707
J05083180-6853372	05 08 31.80	-68 53 37.2	14.253	0.152	-1.594
J05263040-6948033	05 26 30.40	-69 48 03.3	14.683	1.9	-1.402
J05274747-6913205	05 27 47.47	-69 13 20.5	12.736	0.229	-1.528
J05275113-6910460	05 27 51.13	-69 10 46.0	12.596	0.319	-1.398
J05292143-6900202	05 29 21.43	-69 00 20.2	12.016	-0.711	-0.548
J05300119-6956382	05 30 01.19	-69 56 38.2	13.406	0.655	-1.222
J05353280-6904191	05 35 32.80	-69 04 19.1	13.126	0.299	-1.508

Note. — SMC photometry from Zaritsky et al. 2002 and LMC photometry from Zaritsky et al. 2004.

3.2.1 Observations and Reductions

All four stars were observed under clear conditions with 0.7" to 1.0" seeing using a 1" slit. Exposure times ranged from 300s (to obtain an unsaturated spectrum of the Be star) to 1800s. MagE provides coverage from 3100Å to 1μm at a resolving power R of 4100. Thus, we were able to observe the wavelength regions of both the upper Balmer lines and the TiO bands at high resolution. Spectrophotometric standards taken throughout the night allowed for flux calibration before the orders were combined. The data were extracted using a combination of the IRAF echelle package and the 'mtools'[2] IRAF routines originally designed by Jack Baldwin for the reduction of MIKE spectra.

3.2.2 The First RSG+Be Star Binary System

One of the four SMC stars we observed shows strong upper Balmer lines in addition to TiO bands, making it a RSG+B star binary. However, the spectrum also shows emission lines within the core of each upper Balmer line making it different from any of our previously observed binary spectra. Based on these emission lines, we classify the B star component as a Be star. Figure 3.6 shows a spectrum of this star including a subset of the upper Balmer lines with the emission and absorption line components. While Be stars themselves are not rare (in the Milky Way, $\sim 20\%$ of all B stars are thought to be Be stars; see Zorec & Briot 1997), this is the first known RSG+Be star binary system.

As defined, Be stars are B stars that show emission within their Balmer lines. This emission is thought to form from material being ejected due to a star's rapid rotation. This material then forms an outwardly diffusing gaseous Keplerian disk. Usual rotational velocities of Be star rapid rotators are around 300 km s^{-1}. However, based on the widths of the absorption lines of this newly discovered RSG+Be star binary, it has a rotational velocity of around 150 km s^{-1}, much less than a normal Be star. One explanation, as suggested by Doug Gies (private communication) is that this is a Be star with a pole-on orientation so that

[2]'mtools' is available for download from the Las Campanas Observatory web page.

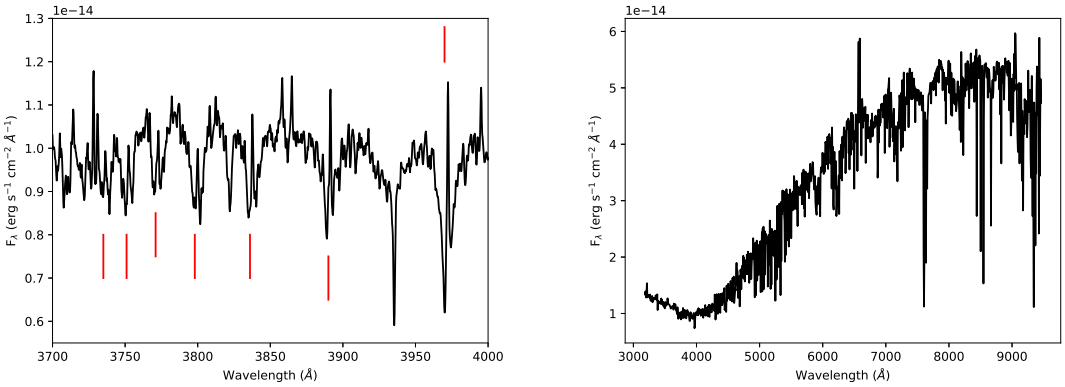

Figure 3.6 - Spectrum of RSG+Be star binary. The figure on the right shows the entire spectrum including the strong TiO bands coming from the RSG. Also note that Hα is in emission near the center of the spectrum. This is indicative of a Be star. The figure on the left shows the emission lines within the cores of the upper Balmer lines. The Balmer lines are marked by red lines. © AAS. Reproduced with permission from Neugent et al. (2019).

the rotational velocity we're measuring is much smaller than the actual rotational velocity. This has been seen before, but such stars aren't common. One such example is χ Oph which has a rotational velocity of around 140 km s^{-1} (Tycner et al., 2008). If we take these two systems to be similar, the inclination of the disk to the line of sight is small, less than 18° for the star to not be rotating faster than the breakup velocity.

Another difference from the more traditional Be star is that the emission lines are quite strong and narrow, though this may be due to the small rotational velocity discussed above. Generally they are wider and double-peaked (compare to Figure 1 in Chojnowski et al. 2018). However, Be stars are known to be variable on timescales over a few minutes and the emission has even been seen to disappear and reappear over the timescale of decades (Rivinius et al., 2013). Thus, we plan on re-observing this interesting object to see if there are any significant spectral changes over the period of a few years.

Using the strength of the He I λ3819 line to the surrounding Balmer lines, we classify this star as an early BV. Lesh (1968) expanded the MK spectral type to include subtypes for Be

stars. Based on Hβ being in emission, the higher Balmer lines having emission cores, and Fe II lines being present but not dominating the spectrum, we classify this Be star as a Be_3V. There are other, more recent, classification systems that take into account various shapes of the Balmer lines and polarization, but the Lesh (1968) system is still commonly used. In terms of further classifying either the absorption or emission components of the Be star, our spectra does not have a high enough S/N to identify the prominent classification lines such as He I / Mg II λ4481. Radial velocity measurements confirm that both the absorption and emission lines have the same radial velocities and thus they are forming in the same region.

3.3 Modeling the Spectra

With the MMT data obtained, we now have 63 confirmed RSG+B star binaries in M31 and M33 as well as 24 confirmed RSG+B star binaries in the SMC and LMC (see Chapters 2 and 4 for more information on the Magellanic Cloud binaries) bringing the total number of RSG binaries to 87. While our spectra of these stars are low resolution, they can still be used for basic modeling. Here we describe our efforts to model the RSG component of the binary using the TiO bands in the red and model the B star component of the binary using the upper Balmer lines in the blue.

3.3.1 MARCS RSG Modeling

To model the RSG star within the binary system, we used the MARCS models with surface gravities of $\log g = 0.0$, as this is typical of RSGs (Levesque et al., 2005). We adopted the solar-metallicity models; the differences in the RSG models between an LMC (0.5 solar) and M31(1.5-2$\times$ solar) are slight; see Figure 5 in Massey et al. (2009). We fit the spectral features and continuum to the MARCS models by eye by changing the temperature of models after smoothing the models so they were at a resolution comparable to the observed spectra. As the temperature of the RSG decreases, the strength of the TiO bands increase because it becomes easier for molecules to form at cooler temperatures. Thus, the TiO bands are very prevalent in M stars but the lines can still be used to estimate temperature in mid-Ks,

especially the λ5167 and λ6158 TiO lines. The MARCS models we used to fit the observed spectra ranged from 3000 K to 4500 K in increments of 100 K. Considering the matches we obtain for different temperatures, we estimate our errors are on the order of 50 K for the M stars and mid-to-late K stars. For the earlier K stars where the TiO bands are the weakest we believe our errors are on the order of 100 K. This process is very similar to the one used by Levesque et al. (2006) when modeling a different set of Magellanic Cloud RSGs. An example best fit model of an early K star and late M star are shown in Figure 3.7. Note the increase in the strength of the TiO bands for the later type stars thus allowing for a more precise fit.

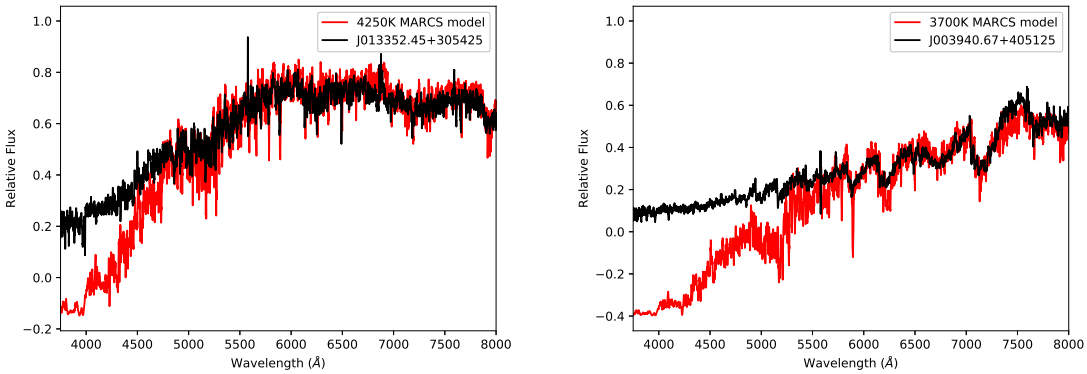

Figure 3.7 - Example fits of MARCS models to observed RSG+B star binary spectra. The figure on the left shows a warm mid-K supergiant spectrum modeled with a 4250 K MARCS model. Notice the weak TiO bands in contrast to the stronger TiO bands in the figure to the right. The figure on the right shows a cool M supergiant with a 3700 K MARCS model over plotted. In both cases, the spectra deviate in the blue because of the presence of the B star adding additional flux in the blue. © AAS. Reproduced with permission from Neugent et al. (2019).

3.3.2 BSTAR06 B-Star Modeling

To model the B star component within the binary system we relied on the BSTAR06 models. The strength of the spectral lines depends on the temperature of the star with cooler temperatures producing stronger lines. The width of the spectral lines depends on the luminosity class of the star with dwarfs producing thicker lines than supergiants. Due to the poor resolution of our spectra, the widths of the lines were difficult to accurately measure. It was generally possible to differentiate between a supergiant (very narrow lines) and a dwarf (broad lines) but nearly impossible to distinguish between those two extremes and giants. Thus, degeneracies exist between luminosity classes and temperatures. For example, a star might be adequately fit by both a 19000 K BV and a 17000 K BIII. Thus, for this project we eschewed the giant subclass and only considered the two extremes of dwarf vs. supergiant. Overall, the temperatures for the giants were 2000 K cooler than that of the dwarfs and 3000-4000 K hotter than the supergiants. As is shown in Table 1.1, all of the previously known Galactic binaries have BV companions, and thus we believe it is reasonable to preferentially select the BV results over that of a BIII temperature.

To fit the Balmer lines of the B stars we first normalized the spectrum using a 5th order cubic spline. We restricted the wavelength range to 3700 - 4200 Å in order to avoid attempting to normalize the strong TiO bands of the RSG. This allowed us to better fit the strengths of the upper Balmer lines of the B star. An example fit is shown in Figure 3.8. Note that both the strength and width of the lines are well matched by the 25000 K BV BSTAR06 model.

To double-check our results, we compared the spectral modeling luminosity classes with the absolute magnitude in U, making the assumption that the extinction of these stars was typical of OB stars, and that the flux at U is dominated by the B star component. We found excellent agreement for the stars we called supergiants, except for the hottest one, J013405.62+304142, whose luminosity is more consistent with a dwarf than a supergiant. For the cooler "dwarfs," the U-band flux is more consistent with them being giants rather

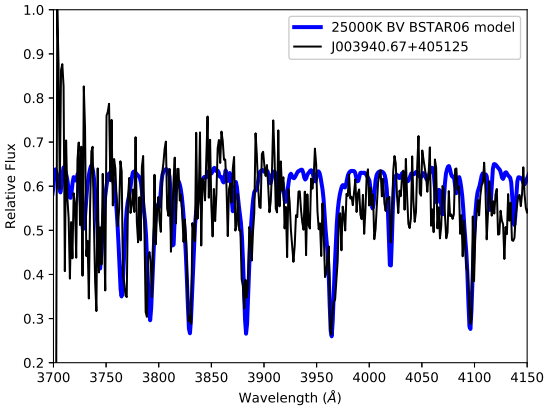

Figure 3.8 - Example fit of BSTAR06 model to observed RSG+B star binary spectra. This figure shows a 25000 K BV model fit to J003940.67+405125. Note the good match between both the strength of the lines (due to the model's temperature) and the width of the lines (due to the model's luminosity class). © AAS. Reproduced with permission from Neugent et al. (2019).

than a dwarfs, but they are not as luminous as supergiants. The warmer dwarfs have U-band luminosities that are consistent with that designation, again indicating that our method worked quite well. There were two notable exceptions, J013254.01+303858 (20,000 K) and J013343.22+303547 (22,000 K), whose U-band luminosities suggest they are supergiants instead, unless the RSG or reflection nebula is adding to the flux. We have retained the spectroscopic designations but indicated the three discrepant stars with a footnote in Table 3.3.

Table 3.3. Modeled Physical Parameters of Confirmed RSG+B Star Binaries

ID	B-star $T_{\rm eff}$ (K)	B-star luminosity class	RSG $T_{\rm eff}$ (K)
J003940.67+405125.4	19000	V	3700
J003942.08+405221.4	17000	V	4000
J003950.51+405307.4	17000	I	3900
J004021.42+404035.7	16000	V	4000
J004030.12+404502.3	20000	V	3900
J004033.98+404429.9	17000	V	4000
J004059.48+410229.4	18000	I	3900
J004106.51+404848.8	26000	V	4000
J004117.43+410837.5	21000	V	3800
J004134.79+411418.1	16000	I	4250
J004145.25+411229.4	16000	V	4000
J004149.73+405300.1	20000	V	4000
J004151.42+411804.7	16000	I	3900
J004158.62+405338.6	22000	V	3800
J004205.57+413345.8	21000	V	4000
J004209.69+411340.7	18000	I	4250
J004238.73+405349.9	25000	V	4000
J004253.28+411246.4	21000	V	4000
J004253.29+411010.8	26000	V	4000
J004254.31+412700.5	30000	I	4000
J004328.81+411854.9	30000	I	3900
J004344.53+411104.6	21000	I	4250
J004348.91+411629.2	30000	I	4250
J004351.83+411431.7	24000	I	4250
J004405.80+411937.4	26000	V	4100
J004410.28+411757.9	30000	I[a]	4000
J004428.15+411002.0	27000	V	4000
J004649.84-731352.	17000	V	4250
J005132.80-720549	25000	V	3800
J005226.47-724515	23000	I	3800
J005318.61-724207	17000	V	4000
J005325.28-721537	19000	V	3800
J005326.55-721203	22000	V	3800
J005344.51-723319	17000	I	3900
J005357.39-731333	17000	V	3900

Table 3.3 (cont'd)

ID	B-star $T_{\rm eff}$ (K)	B-star luminosity class	RSG $T_{\rm eff}$ (K)
J005434.83-722951	20000	V	3800
J010143.57-723825	17000	I	4250
J010237.94-723554	20000	V	4250
J010240.76-721717	19000	V	3900
J010337.30-715844	19000	V	3900
J013250.80+303507.6	30000	I	4250
J013254.01+303858.0	20000	V[b]	3900
J013254.95+302411.1	18000	I	3800
J013256.23+302752.1	24000	I	3900
J013256.84+302347.9	22000	V	4000
J013259.82+303231.5	30000	I	4250
J013301.02+303500.7	30000	I	3900
J013306.83+303039.5	26000	I	3800
J013314.45+302615.2	20000	V	3700
J013315.30+302248.3	28000	V	4000
J013320.17+304655.0	28000	I	4100
J013323.19+304016.2	24000	V	4000
J013323.64+302836.8	21000	V	4000
J013324.56+304908.3	26000	V	3700
J013339.51+304316.6	24000	I	3700
J013342.45+304237.2	23000	V	3900
J013343.22+303547.9	22000	V[b]	3900
J013347.51+304154.9	18000	I	3800
J013347.82+304324.9	20000	V	4000
J013349.94+302928.8	27000	I	3800
J013352.45+305425.6	27000	V	4250
J013355.62+304116.6	29000	V	3800
J013356.09+303834.5	20000	V	3800
J013358.33+302216.5	15000	V	4000
J013358.53+304754.7	17000	I	3700
J013359.54+303200.4	30000	V	3800
J013401.67+304050.7	21000	I	3800
J013402.58+304310.1	25000	V	3800
J013405.62+304142.8	27000	I	3900
J013408.10+304616.3	21000	I	4000

Table 3.3 (cont'd)

ID	B-star $T_{\rm eff}$ (K)	B-star luminosity class	RSG $T_{\rm eff}$ (K)
J013413.98+302759.0	19000	V	3700
J013415.32+303804.3	30000	V	3700
J013431.25+304538.8	17000	I	3800
J013431.85+305400.8	20000	I	3700
J013436.97+304514.9	21000	I	3700
J013439.43+304551.4	18000	I	3700
J013448.91+303140.4	25000	I	3800
J045957.31-674813	16000	V	3700
J050302.32-684720	16000	V	4000
J050433.78-680623	18000	V	3900
J050831.80-685337	17000	V	3700
J052630.40-694803	15000	V	3700
J052747.47-691320	17000	I	3600
J052751.13-691046	23000	V	3700
J052921.43-690020	20000	V	3800
J053001.19-695638	17000	V	3800
J053532.80-690419	20000	V	3400

[a]U-band luminosity suggests V.

[b]U-band luminosity suggests I.

Note. — Errors on B star $T_{\rm eff}$ are 1000K. Errors on RSG $T_{\rm eff}$ are temperature dependent. If $T_{\rm eff} > 3800$K, the error is 100K, for cooler RSGs the error is 50K.

3.3.3 Spectral Energy Distribution Modeling

The modeling described above made one key assumption – that the flux of the binary was unaffected by the B-star component at the TiO bands and was unaffected by the RSG component at the upper Balmer lines. If this isn't the case, it is possible that the B-star flux filled in the TiO bands causing the temperature to be overestimated. Conversely, the flux from the RSG may have filled in the strengths of the upper Balmer lines causing the temperatures to be overestimated as well. The amount the temperature was overestimated will vary from star to star. If the RSG is particularly dusty, the upper Balmer lines will be

filled in more than a system with a small amount of dust. The physical separation between the two stars might also alter the overestimate with stars that are closer together being more overestimated than stars that are farther apart. However, there is no easy way to separate the two spectra and thus this is an assumption we've made.

We originally hoped to model the overall SED of the combined RSG+B star binary. However, after further investigation we determined that the number of free parameters made any resulting fits unreliable.

The first complication deals with the mass of the individual components. For the RSG, we used a $15M_{\odot}$ supergiant as used in the MARCS models; however, given the 8-$25M_{\odot}$ mass range of the RSG population and the effects of the initial mass function this is likely to be an over-estimate for most of the RSGs in our sample. For the B star we used the BSTAR06 models that span a range of masses depending on the type of star (dwarf, giant, supergiant). However, the BSTAR06 models do not take into account that a giant might be $10M_{\odot}$ or even $60M_{\odot}$ but still have the same 20,000 K temperature. Changing the mass of the B star will drastically change the shape of the SED. While it is possible to estimate the temperature and spectral type of the B star using the line depths and widths (as discussed above), it is not possible to use this method to estimate the mass of the star. Thus, we are unable to accurately describe the SED without knowing the mass of the B star. While further observations (both spectroscopic and photometric) would hypothetically allow us to determine the masses of these stars, this is well outside the scope of this current project.

The other complication is the reddening of the system. From the observed spectra alone we know very little about the dust surrounding the system. We can make the basic assumption that the reddening around the B star is either equal to or less than the reddening around the RSG however it is not possible to determine the ratio. This value will additionally change based on the distance between the two stars (a B star in a close binary system should have a higher reddening than a B star in a wide binary system). While we would ideally like to place constraints on the A_Vs of the systems, the poor flux calibration stemming from multi-fiber spectra does not allow for any estimates. To learn more about the reddening of

both components, and thus the dust production of the RSG, we would need additional data in both the UV (for the B star) and the NIR (for the RSG).

3.4 Discussion

Table 3.3 contains an overview of observational and modeling results for each system including the adopted temperatures and luminosity classes for the B-type stars and temperatures for the RSGs.

3.4.1 Overall Trends

All of the previously known (Galactic) RSG binaries have B dwarfs as their companions (Table 1.1), but here we have discovered RSG with B supergiant companions as well. We expect B supergiant companions to be rarer given their shorter lifetimes, and our sample of newly discovered RSG+B pairs is a factor of ∼9 times larger than all of the previously known RSG binaries. We find that 66% of our newly identified RSG sample contain B dwarfs, and 34% contain a B supergiant. Note that, as discussed above, we were not able to distinguish between a dwarf vs. giant or giant vs. supergiant so we've simplified the classifications into just dwarfs and supergiants. There does not seem to be a correlation between temperature or subtype for either the B stars or the RSGs. The average temperature for the B star (for both dwarf and supergiant) is 21000 K with a standard deviation of 4000 K. The average temperature for the RSG (both when paired with a dwarf or supergiant) is 3900 K with a standard deviation of 150 K. These values are reasonable for both RSGs and B-type stars. We would expect to see some change in RSG and B star temperatures from galaxy to galaxy as the metallicity changes but small number statistics prevent us from seeing this trend.

3.4.2 Variability

RSGs are variable on the timescales of days all the way up to years (Szczygieł et al., 2010). Almost all are variable on the order of 1 magnitude or higher while some pulsate between 80

to 3500 days (Guo & Li, 2002). Convective cells and hot spots transverse their surface adding additional photometric variations to any observed light curve (Chiavassa et al., 2011; Baron et al., 2014; Stothers, 2010). Additionally, episodic mass loss events cause non-periodic outbursts such as what occurred with V838 Mon in 2002 (Tylenda et al., 2011). These variations all add to the complexity of searching for binary companions using light curves.

Despite these difficulties, we investigated the variability of LMC and SMC RSG+B star binaries using the All-Sky Automated Survey for Supernovae (ASAS-SN) (Shappee et al., 2014; Kochanek et al., 2017). Out of the 24 confirmed binaries, five of them were previously identified as variable by ASAS-SN but none of them showed periodic variability. Three additional stars were variable but had not been catalogued as variable by ASAS-SN and the remaining 15 did not appear to vary significantly (less than 0.05 mag) over a period of 1000 days. We were a little surprised by this outcome. The known RSG binaries have periods on the order of years and thus with a baseline of 1000 days we expected to see some indication of variation due to binarity. However, this was not the case. In the future we plan on investigating this issue further by searching for small variations within the periods that might indicate binarity and extending this search to the M31 and M33 binaries using iPTF data but that is outside the scope of this current work.

We've now observationally shown that it is possible to select RSG+B star binary candidates using photometry alone. Using such photometry we have confirmed 87 new RSG+B star binaries in the Local Group galaxies of M31, M33, the LMC and the SMC. We additionally discovered the first known RSG+Be binary system. Using the BSTAR06 and MARCS model atmosphere codes we estimated temperatures and luminosity classes for the B stars as well as temperatures for the RSGs and found that there is no correlation between luminosity class and temperature for either RSGs or B stars.

Chapter 4

THE RSG BINARY FRACTION IN THE LARGE MAGELLANIC CLOUD

Our next step is to understand the overall binary fraction of RSGs. To do this we need to obtain a statistically significant sample of both single and binary RSGs within a galaxy. Determining this within our own Galaxy is difficult given reddening and our location within the disk, but the galaxies of the Local Group provide excellent test beds for such research. At this point we are able to place direct constraints on the RSG binary fraction in one of the galaxies we have surveyed, the LMC. We've chosen to focus our efforts on this one galaxy first for several reasons: excellent near infrared (NIR) photometry from 2MASS combined with proper motion estimates from *Gaia* allows us to identify a complete sample of RSGs within the galaxy down to a reasonable luminosity cutoff of $\log L/L_{\odot} = 4$; the LMC is well covered with both *GALEX* and the U, B, V, I photometric catalog of Zaritsky et al. (2004) and the resulting near ultraviolet (NUV) and optical colors allow us to identify possible B star companions; it has a well known and understood metallicity (unlike much of M31 and M33); and we've completed several extensive observing runs spectroscopically confirming RSG+B star binaries over a wide range of color-color space such that we understand our completeness rates. Here we provide a first look at the binary fraction of RSGs at the sub-solar metallicity of the LMC.

Our survey was designed to primarily be sensitive to RSG+OB star companions (though we expect to find few O stars due to their short lifetimes) given the reasoning discussed above. We then rely on the Binary Population and Spectral Synthesis (BPASS) models (v2.2.1; Eldridge et al. 2017; Stanway & Eldridge 2018) to estimate the model-dependent, but small, correction factors to the RSG binary fraction which we are not observationally

sensitive. This method is purposefully not sensitive to RSG+protostars and additionally lacks sensitivity to RSGs in systems with other RSGs and the even shorter lived YSGs; however, based on evolutionary timescales, these pairings should be rare.

4.1 Identifying Red Supergiants

To calculate the binary fraction of RSGs in the LMC, we first needed to identify a parent sample of all LMC RSGs, aiming to be as complete as possible in order to make the statistics robust. We will then later determine what fraction of these have binary companions. Our goal was to select a complete sample of RSGs down to $\log L/L_{\odot} = 4$ which corresponds to a minimum initial mass of around $9M_{\odot}$ (see Fig. 2 in Ekström et al. 2012). Such a sample will be contaminated both by Galactic foreground stars (nearby red dwarfs) and by the brighter asymptotic giant branch (AGB) stars in the LMC. We eliminated these using the same procedure that we recently used for M31 RSGs (Neugent et al., 2020b)[1]: foreground stars were removed using *Gaia* data, and AGB stars were separated from RSGs using cuts in a ($J - K_s$, K_s) color-magnitude diagram (CMD), following the pioneering work of Yang et al. (2019). In order to select a sample of RSGs that was unbiased by the presence of a hot companion, we chose to rely upon 2MASS J and K photometry as the near-IR (NIR) colors will be relatively insensitive to the presence of a hot companion. Thus, our selection criteria allows us to determine a complete sample of all RSGs, binary and non-binary alike.

4.1.1 Selecting Red Stars From 2MASS

We began by selecting sources from the 2MASS point-source catalog (Skrutskie et al., 2006) within 210' of the center of the LMC, taken to be $\alpha_{\rm J2000}$=05:18:00 and $\delta_{\rm J2000}$=-68:45:00, chosen to match the same field used for the recent survey for WR stars in the LMC (Massey et al., 2014; Neugent et al., 2018b) and encompassing the entire optical disk of the galaxy. We kept only objects with the best 2MASS photometry, i.e., with quality flags of "AAA,"

[1]In order to present this work more logically in this thesis, this work appears here later in Chapter 7.

and "artifact contamination" flags of "000." Our initial selection was restricted to stars with $K_s \leq 13$, and $J - K_s \geq 0.5$. This left us with a sample of 87,637 stars.

These magnitude and color limits were chosen to be extremely generous. A $K_s = 13$ star in the LMC would have $\log L/L_\odot \sim 3.0 - 3.3$, adopting a distance to the LMC of 50.0 kpc, and the equations given in Table 4.1. This is much smaller than our completeness goal of $\log L/L_\odot \sim 4.0$. Similarly, a lightly reddened $J - K_s = 0.5$ star will have an effective temperature ($T_{\rm eff}$) of 5000 K (using equation 1 from Neugent et al. 2012b), much warmer than the $\sim$ 4200 K upper temperature limit for RSGs we will employ below.

In Figure 4.1(a) we show the CMD of the sample of 87,637 stars. In the next two sections we will demonstrate how we refine these to select out only the RSGs.

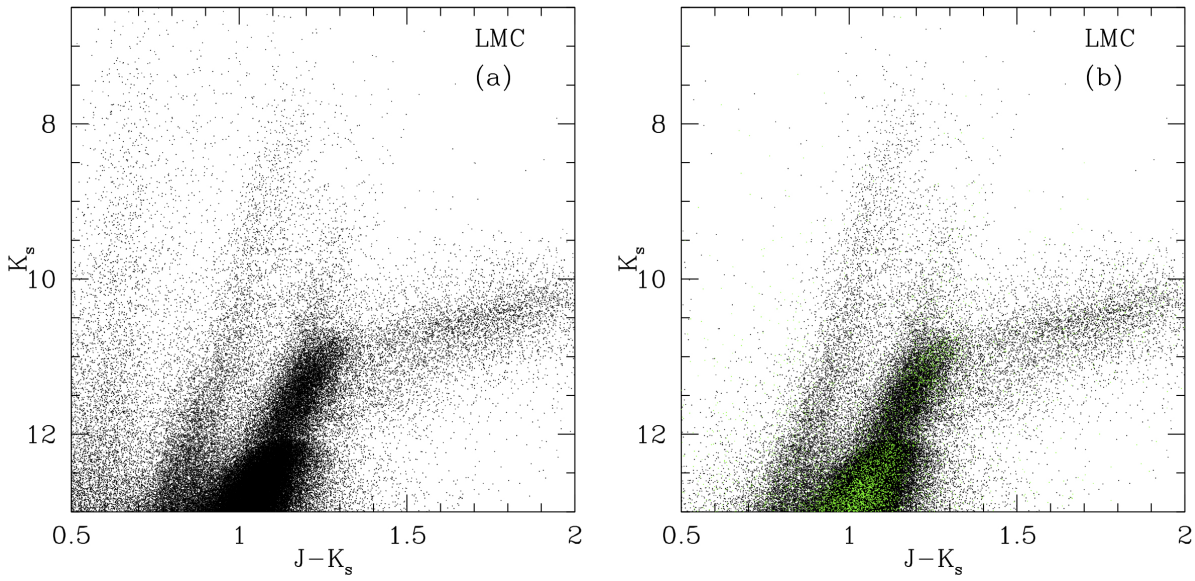

Figure 4.1 - The CMD for our sample. (a) The CMD is shown for all 87,637 stars in our initial sample obtain from 2MASS. (b) The same as (a) but now with probable foreground stars removed. The green points denote the stars either without any *Gaia* data or without *Gaia* parallax data. © AAS. Reproduced with permission from Neugent et al. (2020a).

4.1.2 Removing Foreground Stars

The majority of the very red stars in the LMC will be members, as previously shown by radial velocity studies (see, e.g., Neugent et al. 2012b), but a few will be foreground, and as we approach the warmer temperatures and yellower colors, there will be increasing contamination from Galactic stars. Indeed, in the color regime for YSGs, Galactic contamination becomes even more overwhelming. Fortunately, *Gaia* data (Gaia Collaboration et al., 2018) provides the means to identify these foreground objects through the judicious analysis of proper motions and parallaxes. We say "judicious," as there is a known systematic offset in *Gaia* DR2 astrometric measurements and the formal uncertainties provided do not represent the total error (Lindegren et al., 2018).

To assess the probability of LMC membership, we adopted a procedure similar to that described in Gaia Collaboration et al. (2018). First, we select a large set of highly-probable LMC stars in order to define the distributions of astrometric parameters that are expected for true members. We initially select all sources overlapping the LMC with *Gaia* G < 18 mag. In order to minimize any foreground contamination in this baseline sample, we then exclude all sources with either yellow colors ($0.7 \text{ mag} < G_{bp} - G_{rp} < 1.1$) or parallax measurements greater than 4σ as well as any remaining sources whose parallaxes or proper motions deviated from the rest of the sample by $>4\sigma$. The red 2MASS stars identified above are then compared to this sample in order to assess their consistency with the kinematics of the LMC. If the proper motions and parallax of a given star fall outside the region that contains 99.5% of the comparison sample, we flag it as a probable foreground star. Conversely, if a star falls within the region that contains 75% of the comparison sample, we consider it a likely LMC member. Stars that fall in between are flagged as having "ambiguous" membership based on astrometry alone. Further details of our application of this method can be found in Aadland et al. (2018). Figure 4.2 shows where our LMC members, probable foreground stars, and ambiguous results fall in proper motion and parallax space.

There were eight photometrically selected RSGs (as defined below) whose proper motions

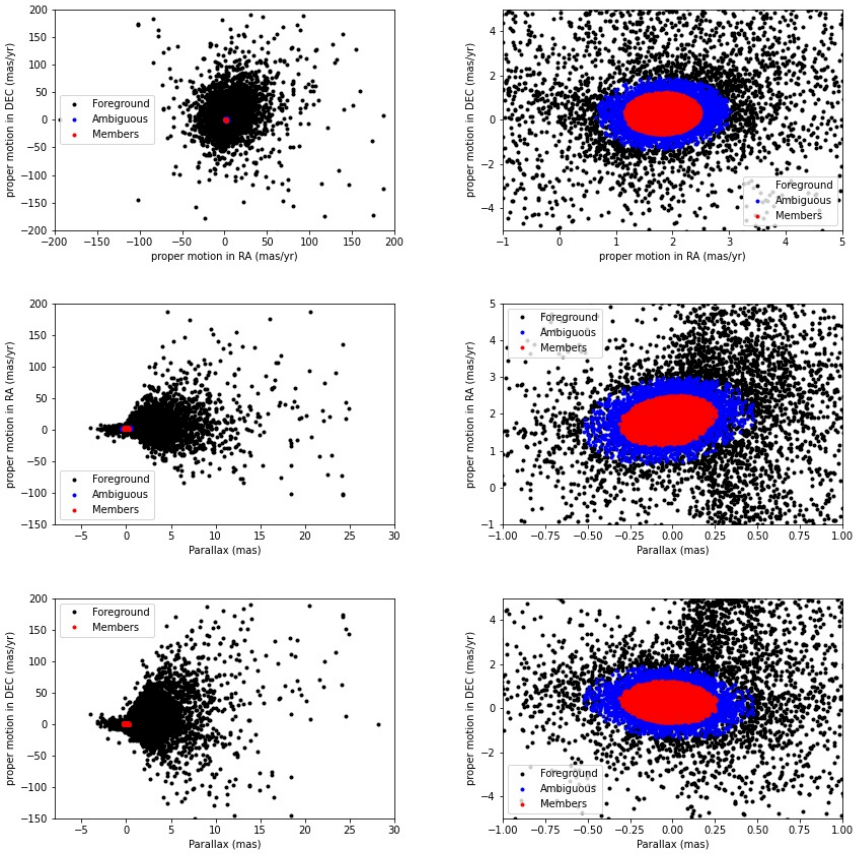

Figure 4.2 - *Gaia* information on LMC members, probable foreground and ambiguous stars. The top two figures show the proper motions in both right ascension (RA) and declination (DEC) plotted for all of the stars shown in Figure 4.3's CMD with the top right figure showing in a zoomed in version that better differentiates the differences between the three classification categories. The middle two figures show the proper motion in RA plotted against the parallax with again the bottom right figure showing a zoomed in version. The bottom two figures show the proper motion in DEC plotted against the parallax with again the bottom right figure showing a zoomed in version. Note that these figures were not used to *select* candidates, but rather simply show the results of our selections. © AAS. Reproduced with permission from Neugent et al. (2020a).

were consistent with LMC membership, but have quoted *Gaia* DR2 parallax measurements that are more negative than our comparison sample of LMC stars. A large negative parallax is nonphysical, but suggests that these objects may not be foreground stars. We therefore retained these stars in our sample, but changed their status from "probable foreground" to "ambiguous" results. This included one star, 05300119-6956382, that had been previous identified in Neugent et al. (2019) (Chapter 3) as a RSG+B star binary.

Two other RSG+B binaries from the work discussed in Chapter 3, 05274747-6913205 and 05292143-6900202, would have also been dismissed as non-members were it not for the spectroscopic information. In the case of 05274747-6913205, the Gaia parallax of 0.5561±0.0746 mas has a quoted significance of $>7\sigma$ and is consistent with a distance of 1.8 kpc (Bailer-Jones et al. 2018), but the proper motions and radial velocity (280 km s^{-1}) are in excellent agreement with membership in the LMC. The spectrum is that of a cool star with strong TiO bands, consistent with its J-K colors; Balmer lines are clearly present. We retain this star, but flag the *Gaia* results as ambiguous. As for 05292143-6900202, *Gaia* does not robustly detect a parallax (0.4757±0.1604); the proper motions are slightly outside the accepted spread we have adopted for membership, but the errors are large. Both its ground-based and *Gaia* radial velocities (also 280 km s^{-1}) suggest membership in the LMC. The spectrum is consistent with its colors, a late K or early M, with clear upper Balmer lines. We also retain this star, describing its membership as ambiguous. We note that *Gaia* parallaxes can be impacted by both binarity and variability, both of which may be common in our sample.

One other star labeled as a RSG+B binary in Chapter 3, 05065284-6841123, shows up as a foreground star. Further inspection of the unpublished AAT spectrum showed that there were reduction problems, and we no longer consider this star a RSG binary.

After cross-matching with *Gaia* (and making these small adjustments), out of the 87,637 red stars, 73,361 (83.7%) were probable members; 3,585 (4.1%) had ambiguous results; 9,651 (11.0%) were probable foreground stars; and 1,040 (1.2%) either had no match with *Gaia* or did not have *Gaia* parallax data that could be used to determine membership.

At this point, we removed the probable foreground stars from our sample but left the

probable members as well as those with either ambiguous results or incomplete *Gaia* data. How the addition of the ambiguous results might alter our calculated binary fraction is discussed below. In Figure 4.1(b) we show the CMD after the foreground stars were removed. Note that the vast majority of these stars were those with lower $J - K_s$ values, consistent with our statement above that the contamination in our sample is primarily at the warmer temperatures. The green points are the stars for which there were incomplete or no *Gaia* data.

4.1.3 Filtering Out AGBs and Red Giants

Contamination by AGBs has long been the bane of RSG population studies. AGB stars are evolved low- to intermediate-mass stars which are in their He- and H-shell burning phase. These stars overlap in luminosity with RSGs below $\log L/L_{\odot}$ of 4.9 as noted by Brunish et al. (1986). Using optical photometry, one's only recourse was to limit RSG population studies to higher luminosities.

However, AGBs are cooler than RSGs since the Hayashi limit shifts cooler at lower masses (Hayashi & Hoshi, 1961). Yang et al. (2019) used a ($J - K_s$, K_s) CMD to separate RSGs and AGBs in the SMC following the work of Cioni et al. (2006) and Boyer et al. (2011). We adapted this method for our recent identification of RSGs in part of M31, as discussed later in Chapter 7. We found that the color of the AGB/RSG boundary shifted in M31 relative to that of the SMC in the manner expected from the shifting of the Hayashi limit to cooler temperatures at higher metallicities demonstrating that cuts must be established for each galaxy separately.

Here we repeat the same process for the LMC. Figure 4.3 shows the same CMD as shown previously, but now with the sequences labeled and probable foreground stars removed. The tip of the red giant branch (TRGB) is striking at $K_s = 12$, or about $M_K = -6.5$[2]. The location of the oxygen-rich, carbon-rich, and "extreme" AGBs are shown, based upon the

[2]In contrast, the CMD shown by Neugent et al. 2020b for M31 (their Figure 8) goes to $K_s = 17$, or $M_K \sim -7.6$, and so doesn't extend down as far as the TRGB. This work will appear in Chapter 7.

nomenclature of Boyer et al. (2011); see, in particular, their Figure 4, based on a combination of 2MASS and Spitzer data.

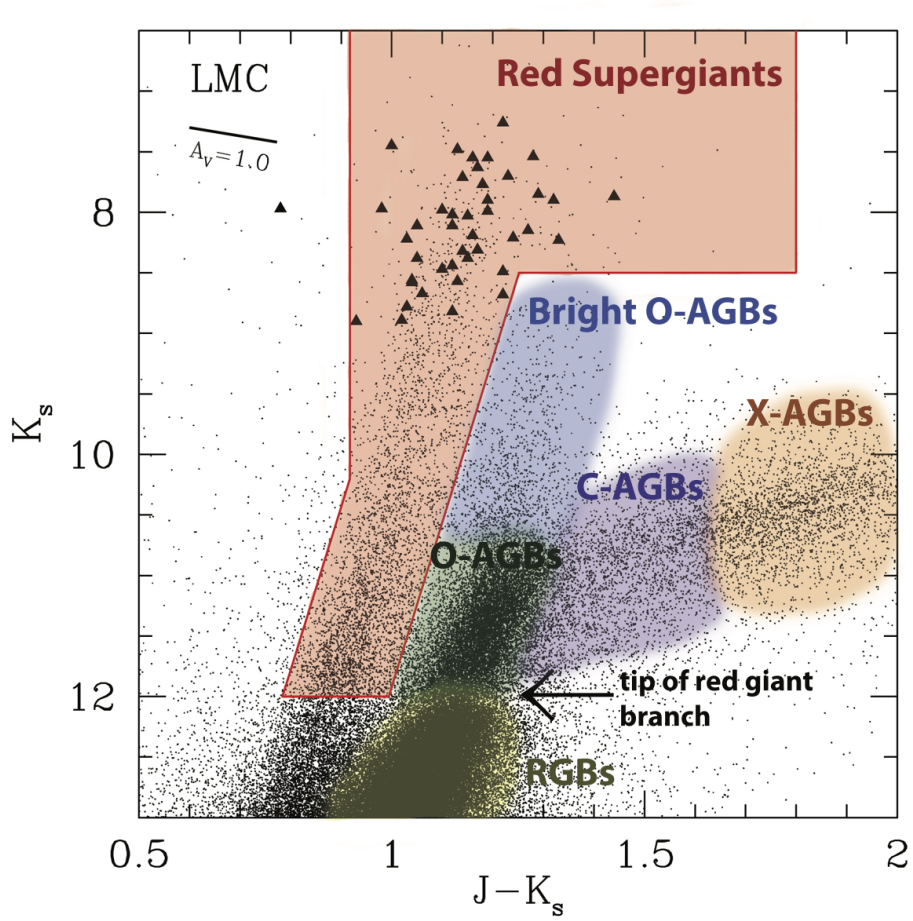

Figure 4.3 - The CMD for cool members of the LMC. The various AGB branches (Boyer et al., 2011) and red giant branch (RGBs) are labeled, along with the tip of the red giant branch. (Note that the division between the carbon-rich AGBs [C-AGBS] and extreme AGBs [X-AGBs] is somewhat arbitrarily denoted in this diagram, as the actual definition was based upon $J-K$ colors Boyer et al. 2011.) The triangles show red supergiants analyzed from our previous work (Levesque et al., 2006, 2007, 2014). The reddening vector corresponding to $A_V = 1.0$ mag is also indicated. © AAS. Reproduced with permission from Neugent et al. (2020a).

The realm of the RSGs is fairly easy to separate from these other stars, and we have drawn in the envelope of what we consider to be the RSG sequence. The locations are intermediate in color between what Yang et al. (2019) adopted for the SMC and what Neugent et al. (2020b) adopted for M31 (as seen in Chapter 7); this is consistent with the LMC having a metallicity that is intermediate between the two. (Note that the SMC and LMC metallicities are usually taken to be 1/3 and 1/2 solar, respectively; see Russell & Dopita 1990, while M31's metallicity is about 1.5× solar; see Sanders et al. 2012.) In Table 4.1 we provide the color relationships we use to define the RSG region of the LMC CMD. Next we'll describe how we defined our K_s and $J - K$ cuts.

The red giant branch (RGB) and the RSG sequences begin to merge at $K_s = 12.5$ and fainter which corresponds to $\log L/L_\odot \sim 3.3$. Since these diagrams go much fainter than our desired completeness limit of $\log L/L_\odot = 4$, we cut our RSGs at $K_s = 12$, roughly the TRGB, similar to the approach adopted by Yang et al. (2019) for the RSGs in the SMC. This still allows completeness to $\log L/L_\odot \sim 3.6$ using the transformations in the next section, still considerably lower than the lowest luminosity we're concerned about.

After defining a faintness limit for K_s, we next investigated the best way of determining the lower value for $J - K$ as a function of K_s. When selecting RSGs in M31, we chose to make their low (yellow) $J-K_s$ limit parallel to the high (red) $J-K_s$ limit following previous studies (e.g., Boyer et al. 2011). In that case, there were a substantial number of yellow stars without *Gaia* data and they were concerned with removing yellow foreground contamination. However, here we do not have this issue and placing similar cuts would impose unrealistic requirements on the temperatures of the brightest stars. Using the transformations in the next section, a $T_{\rm eff}$ of 4200 K corresponds to an observed $J - K_s = 0.917$, where we assume a visual extinction $A_V = 0.75$ mag as argued below. We therefore have modified the low (yellow) $J - K_s$ limit as shown in Figure 4.3 compared to what we used in M31, and as documented in Table 4.1. The scarcity of stars to the left of the low $J-K_s$ line is consistent with evolutionary theory: stars zip across the HRD to the RSG phase, spending very little time as YSGs, of order tens of thousands of years (see discussion in Drout et al. 2009 and

Table 4.1. Adopted and Derived Relations for LMC

Relation	Source
Adopted Distance:	
LMC: 50 kpc	1
Reddening Relations:	
$A_K = 0.12A_V = 0.686E(J-K)$	2
$E(J-K) = A_V/5.79$	2
RSG Photometric Criteria:	
$10.20 < K_s \leq 12.0$: $K_s \geq K_{s0}$ and $K_s \leq K_{s1}$	3
$K_s \leq 10.20$: $J - K_s \geq 0.917$ and $K_s \leq K_{s1}$	3
$K_s \leq 8.5$ and $(J-K_s) \leq 1.8$: $J - K_s \geq 0.917$	3
$K_{s0} = 22.62 - 13.542(J-K_s)$	3,4
$K_{s1} = 25.46 - 13.542(J-K_s)$	3,4
Adopted Extinction:	
$K_s > 8.5$: $A_V = 0.75$	3
$K_s \leq 8.5$ and $K_s \leq K_1$: $A_V = 0.75$	3
$K_s \leq 8.5$ and $K_s \geq K_1$: $A_V = 0.75 + 5.79 \times \Delta(J-K_s)$	3
$\Delta(J-K_s) = (J-K_s) - (24.04 - K_s + 0.686(J-K_s))/14.228$	3
Conversion of 2MASS (J, K_s) to Standard System (J, K):	
$K = K_s + 0.044$	5
$J - K = (J - K_s + 0.011)/0.972$	5
Conversion to Physical Properties (Valid for 3500-4500 K):	
$T_{\rm eff} = 5606.6 - 1713.3(J-K)_0$	3
$\mathrm{BC}_K = 5.495 - 0.73697 \times T_{\rm eff}/1000$	3
$K_0 = K - A_K$	...
$M_{\rm bol} = K_0 + \mathrm{BC}_K - 18.50$	1
$\log L/L_\odot = (M_{\rm bol} - 4.75)/-2.5$	...

References. — 1–van den Bergh 2000; 2–Schlegel et al. 1998; 3–Neugent et al. 2020a (Chapter 4); 4–Cioni et al. 2006; 5–Carpenter 2001

Neugent et al. 2012b). The tilt of this line at lower luminosities in essence says that higher luminosities RSGs are cooler than those of lower luminosities; this is consistent with what the evolutionary tracks say as well (Ekström et al., 2012; Stanway & Eldridge, 2018).

Finally, we decided to relax the color requirement on the upper $J - K$ values at the brightest magnitudes, as there should no longer be any AGB contamination. Again, this is consistent with what we did in M31, as is discussed in Chapter 7, and Yang et al. (2019) did for the SMC. This allows for the fact that the higher luminosity RSGs could be more heavily reddened by circumstellar dust, an effect confirmed by us in Chapter 7 for M31.

4.1.4 Transformations

To put our derived binary fraction in context, it is helpful to understand the physical properties of the stars probed; in addition, our LMC RSG sample will likely be used by ourselves and others for a variety of studies. We therefore provide here the transformations from the CMD to the physical HR diagram of $T_{\rm eff}$ and the log of the luminosity relative to that of the Sun ($\log L/L_{\odot}$). Our procedure closely parallels the one we describe for M31 in Chapter 7.

The typical OB star in the LMC has an extinction in the visual bandpass of $A_V = 0.40$ mag (Massey et al., 2007b), but in general, RSGs have larger extinction due to circumstellar dust (Levesque et al., 2005; Massey et al., 2005). The typical A_V for RSGs in the LMC is 0.75 mag based upon the spectrophotometric fits of 36 stars done by Levesque et al. (2006). This is the same as we adopted for RSGs in M31 as described in Chapter 7 based upon the spectrophotometric fits of Massey et al. (2009). In M31 we found a clear trend in A_V with luminosity for the highest luminosity stars, not surprising given that those stars are likely to suffer higher mass loss (see, e.g., Ekström et al. 2012) as they approach the Eddington limit or develop late-stage pulsations at high luminosities (van Loon et al., 2005; Bonanos et al., 2010; Davies et al., 2008). Thus, we adopt $A_V = 0.75$ for the entire sample except for the few brighter stars ($K_s < 8.5$). For those stars, we determine the extra extinction in such a way to match the average K_s vs $J - K_s$ relation along a reddening vector. The relevant equations are given in Table 4.1. These higher reddenings affected only

45 stars in our sample of 4090 RSGs (1.1%), and had values that ranged from $A_V = 1.34$ mag to 3.37 mag. RSGs with considerably larger amounts of circumstellar extinction are known both in the Galaxy (Massey et al., 2005) and the LMC (Levesque et al., 2009). The impact of these higher extinction values on the derived luminosities is relatively minor: as noted in Table 4.1, the equivalent A_K values are only 12% of the A_V values, and at most the extra extinction we deduce increases $\log L/L_\odot$ by 0.1 dex. Given the luminosity dependence on these higher mass loss events, we do not believe we are missing a population of lower luminosity RSGs with higher than expected reddening values.

Before applying any extinction correction, we first transform the 2MASS $J-K_s$ colors and K_s brightness to the standard $J-K$ and K system (Bessell, 1990) using the transformations determined by Carpenter (2001); these equations are given in Table 4.1. The transformation from $J-K$ to $T_{\rm eff}$ is then determined by first de-reddening the color assuming $E(J-K) = A_V/5.79$ (Schlegel et al., 1998), and then using the MARCS stellar atmosphere models (Plez et al., 1992) computed for LMC metallicity described by Levesque et al. (2006) to relate the intrinsic $(J-K)_0$ colors to $T_{\rm eff}$. The typical errors on $T_{\rm eff}$ are 150 K, where this value is dominated not by the photometric uncertainties but rather by assuming an uncertainty of ± 0.5 mag on our value for A_V. The relationship is quite linear over the relevant color range. To determine the bolometric luminosity, we first correct the K-band photometry for extinction ($A_K = 0.12 A_V$, Schlegel et al. 1998). The bolometric correction then comes from the adopted $T_{\rm eff}$, and we determine the bolometric magnitude using a distance modulus of 18.50 (50 kpc; van den Bergh 2000). The relevant equations are given in Table 4.1.

We note explicitly that our reddening correction makes the assumption of a normal Cardelli et al. (1989) reddening law with a ratio of total-to-selective extinction $R_V = 3.1$. However, we also note that our use of NIR photometry makes this assumption relatively benign, and our results robust. We have used A_V to characterize the amount of reddening both for convenience and because the 0.75 mag value came out of fitting the optical spectrophotometry by Levesque et al. (2006). However, as shown in Table 4.1, we actually correct the photometry by A_K (for luminosity) and by $E(J-K)$ for effective temperature

and bolometric corrections to the luminosity. The relationships between these and A_V come from Schlegel et al. (1998), who adopted the Cardelli et al. (1989) law, which would be generally applicable in the optical and NIR to the interstellar dust found in the Milky Way and Magellanic Clouds. However, we know little about the dust properties of grains in the circumstellar environments of RSGs. As discussed by Massey et al. (2005), Galactic RSGs with abnormally large extinction compared to neighboring OB stars show a correspondingly large UV excess compared to stellar models, primarily indicative of scattering, but that large grains may also play a role. Indeed, the recent dimming of Betelgeuse seems like it was caused by a dust episode with grains that are so large that the extinction was nearly grey (Levesque & Massey, 2020). What we do know from multiple SED fittings, is that the CCM law works well at wavelengths beyond the near-UV; see, e.g., Levesque et al. (2005, 2006, 2007), even in cases of extremely high extinction, such as WOH G64 with $A_V = 6.8$ mag Levesque et al. (2009). Thus, the assumption that the circumstellar reddening in the optical and NIR is similar to that of interstellar dust appears to be borne out empirically. In addition, the use NIR photometry makes the issue of reddening relatively moot, given that the extinction in A_K is only 12% that of A_V, and thus an uncertainty even of 1 mag in A_V would affect our M_K value by only 0.12 mag. As mentioned above, such a mistake would affect the derived luminosity by 0.13 dex when the effect both on the extinction and bolometric correction were taken into account. It is indeed partially for this reason that we chose to use NIR photometry.

Table 4.2 contains the coordinates, 2MASS J and K colors, and derived temperatures and luminosities for the 4090 RSGs in the LMC. We note that the color limits imposed in the CMD require a $T_{\rm eff}$ as a function of $\log L/L_\odot$. For $4.0 \leq \log L/L_\odot \leq 4.25$, $T_{\rm eff}$ has a minimum of $5300 - 362 \log L/L_\odot$ and a maximum of $5333 - 362 \log L/L_\odot$. For $\log L/L_\odot > 4.25$, $T_{\rm eff}$ has a minimum of 4200 K and a maximum of $5333 - 362 \log L/L_\odot$.

Table 4.2. Red Supergiant Content of the LMC

2MASS	α_{2000}	δ_{2000}	K_s	σ_{Ks}	$J-K_s$	σ_{J-Ks}	Gaia[a]	Spect.[b]	A_V	$T_{\rm eff}[K]$[c]	$\log L/L_\odot$[d]
04393719-6856276	04 39 37.194	-68 56 27.63	10.816	0.019	1.033	0.031	0	0	0.75	4000	3.97
04394815-6935580	04 39 48.158	-69 35 58.01	11.825	0.024	0.937	0.033	0	0	0.75	4150	3.62
04395031-6846522	04 39 50.313	-68 46 52.28	11.619	0.021	0.903	0.032	0	0	0.75	4200	3.72
04395844-6849535	04 39 58.440	-68 49 53.58	11.994	0.021	0.903	0.032	3	0	0.75	4200	3.57
04400185-6916490	04 40 01.854	-69 16 49.04	10.977	0.023	0.949	0.035	0	0	0.75	4150	3.95
04401895-6941085	04 40 18.952	-69 41 08.57	11.857	0.023	0.999	0.035	0	0	0.75	4050	3.57
04402177-6835339	04 40 21.771	-68 35 33.95	11.379	0.023	0.973	0.032	0	0	0.75	4100	3.78
04404852-6822211	04 40 48.526	-68 22 21.15	11.242	0.023	0.876	0.035	0	0	0.75	4250	3.88
04405219-6804580	04 40 52.194	-68 04 58.00	11.014	0.019	1.064	0.030	0	0	0.75	3950	3.87
04410088-6840425	04 41 00.880	-68 40 42.53	11.833	0.023	0.821	0.033	2	0	0.75	4350	3.67

Note. — This table is published in its entirety in Neugent et al. 2020a. A portion is shown here for guidance regarding its form and content.

[a]LMC membership based upon *Gaia:* 0=member, 1=uncertain, 2=incomplete or no data, 3 = ambiguous.

[b]Spectroscopy used: 0=no spectra, 1=CTIO 4-m from Levesque et al. (2005), 2=Magellan data from Neugent et al. (2019) (Chapter 3), 3=Magellan data from Neugent et al. (2020a) (Chapter 4).

[c]Typical uncertainty 150 K.

[d]Typical uncertainty 0.05 dex.

4.2 Spectroscopically Confirming RSG+B Binaries

After selecting RSGs as described above, we next turned our attention towards identifying the subset of these RSGs that additionally have B star companions. To do this, we took a similar approach to the search for RSG binaries in M31 and M33 described in Chapter 3 and used photometry to identify a subset of candidates before heading to Las Campanas for spectroscopic confirmation.

Overall, we obtained spectra of 63 candidates in the LMC. Of these, 25 were single RSGs and the remaining 38 were RSG+B binaries. We additionally observed 22 new candidates in the SMC and confirmed 14 as single RSGs and 8 as new RSG+B binaries which will briefly be discussed in Chapter 4.2.4.

4.2.1 Selection Criteria

While 2MASS NIR colors are helpful for identifying RSGs, we needed additional information about the RSGs' flux in the bluer wavelengths to determine if they have B star companions. For this information we used Zaritsky et al. (2004), which contains U, B, V, and I photometry for most of our survey region of 4090 stars. After cross-matching our list of LMC RSGs with Zaritsky et al. (2004) using a 1" radius, we found that 3870 (95%) had U-band photometry, 3992 (98%) had both B and V, and 3579 (88%) had I. The remaining 98 stars had no match in Zaritsky et al. (2004), primarily due to crowding (over half of such stars were located in the inner bar).

Since RSGs with B star companions will have smaller $U - B$ colors (and thus higher flux at bluer wavelengths) than those without, we focused on observing RSGs with small $U - B$ colors. As discussed in Chapter 3, we previously identified RSG+B star binaries in the Magellanic Clouds using archival spectra. Of the 23 we identified, 8 have $U - B < 0$, and all but 2 have $U - B < 1$. Thus, as we'll discuss when we calculate the binary fraction, we believe that the majority of RSG+B star binaries have $U - B$ colors less than 1 so we focused the majority of our spectroscopic observing efforts on those stars. However, we still observed a few candidates with $U - B$ colors between 1 and 2 to better characterize the binary fraction at slightly higher $U - B$ values and attempt to define a $U - B$ color "cut-off" above which RSG+B star binaries aren't found.

Of the 95% of LMC RSGs with U and B photometry, 127 (3%) have $U - B < 0$, 388 (10%) have $0 < U - B < 1$, and 2870 (74%) have $1 < U - B < 2$. However, to maximize the number of stars observed, we focused on the brighter targets (generally those with U brighter than 16th). This decreased our initial target list to 107 stars with $U - B < 0$, 142 with $0 < U - B < 1$, and 25 with $1 < U - B < 2$. We then attempted to observe a subset of those with a wide range of $U - B$ values to determine the binary fraction as a function of $U - B$.

4.2.2 Observations and Reductions

Candidate RSG+B star binaries were observed with the Magellan Echellette (MagE; Marshall et al. 2008) instrument on the Baade 6.5-m telescope at Las Campanas Observatory over two dedicated observing runs in 2019 and 2020 and an engineering run in 2019. The first two night run occurred on UT 2019 September 07-08 when we observed both SMC and LMC targets and were plagued by atrocious seeing that varied between 2" and 4". We were still able to achieve adequate S/N by simply increasing our exposure times thanks to our objects' bright magnitudes ($U \sim 14.6, B \sim 14.3, V \sim 12.9$). The seeing was somewhat improved during our second run on UT 2020 January 14-15 with seeing that started out at 1" and degraded to 2.2". On the second run, just LMC targets were observed. Additionally, 14 LMC targets were observed with MagE during engineering time on UT 2019 September 12-13 with 1" seeing. On all runs we used a 1" slit and exposure times ranged between 300 for the brightest targets to 1200 for the dimmest targets obtained during poor seeing. The MagE instrument gives a wavelength coverage of 3400Å to 1 μm at R $\sim$ 4100 allowing us to observe both the upper Balmer lines between $3700 - 4000$Å and the TiO bands redwards of 6000Å simultaneously. We additionally observed spectrophotometric standards throughout the night to assist with flux calibration. The data were extracted using both the IRAF echelle package and *mtools* routines designed by Jack Baldwin for the reduction of spectra obtained with another one of Las Campanas' instruments, the Magellan Inamori Kyocera Echelle (MIKE).

4.2.3 The Observed Sample

Our goal when observing was both to spectroscopically confirm single and binary RSGs but also to get a sense of how the binary fraction might change with respect to increasing $U - B$ colors. To do this correctly, we had to be confident in our classifications and not, for example, mistakingly classify a single RSG as single when really we just hadn't observed long enough to detect the faint upper Balmer lines of its companion. Thus, our exposure times were

dictated by our desire to either observe or conclusively rule out the presence of the upper Balmer lines. Based on previous observations described in Chapter 2, we determined that a S/N greater than 100 at our spectral resolution of $R \sim 4100$ was needed to definitively rule out the presence of upper Balmer lines coming from the faintest possible B star (a 15000 K B dwarf; $M_V = -1.5$). We therefore first observed each target with a short (5-10 minute) exposure and checked the S/N of the spectra in real time. We additionally performed quick-look reductions which were completed just a few minutes after each spectrum had read out. If the star showed upper Balmer lines, we moved on. If it didn't, and the S/N was below 100, we continued observing the candidate until we either detected the upper Balmer lines, or the S/N reached 100. Given this observing strategy, we are confident that the stars we have labeled as single do not have hidden B-star companions with $M_V > -1.5$, which should encompass all B-type stars.

Overall, the photometry of the spectroscopically confirmed binary and single stars was as expected with stars with lower $U - B$ colors being binaries. We observed 27 candidates with $U - B < 0$ and 74% of them were RSG+B star binaries (the remaining 7 stars being single RSGs). We found a similar percentage of binaries (71%) for the 24 stars we observed with $0 < U - B < 1$. For the remaining 12 stars we observed with $U - B > 1$, only one was a RSG+B binary. As discussed extensively in Chapter 3.1.4, likely reasons for single RSGs having anomalously blue $U-B$ colors include the possibility of dust scattering that produces a blue reflection nebula or even the much simpler explanation of poor initial photometry.

4.2.4 Small Magellanic Cloud Observations

While our overall goal was to determine the binary fraction of RSGs in the LMC, our first observing run was scheduled in early September and the LMC wasn't above 2 airmasses until around half way through the night. Thus, we started off each night by observing a few candidates in the SMC based upon stars with $U - B < 1$ and U brighter than $\sim$ 16th from the RSG sample presented in Yang et al. (2019) and crossmatched with Zaritsky et al. (2002) for U, B, V, and I colors. Overall we observed 22 new candidates and confirmed 14 as single

RSGs and 8 as new RSG+B binaries. Because we weren't able to observe a statistically significant sample of candidates, we are not comfortable estimating a binary fraction for RSGs in the SMC yet. While we hope to be able to expand on this research more in the future, at this point we've chosen to simply include our findings on these 22 stars in Table 4.3. A further discussion on deriving the physical properties of these stars can be found in the Appendix of Neugent et al. (2020a).

4.3 Calculating the Binary Fraction

To calculate the binary fraction of RSGs in the LMC, we followed a multi-step process. We first estimated an initial binary fraction using a K-nearest-neighbor algorithm (k-NN; Cunningham & Delany 2020) that combined archival photometry with our spectroscopically observed single and binary RSGs. We then adjusted the fraction and corresponding error bars to account for the following biases: line-of-sight stars masquerading as binaries, binaries in eclipse not detected during the photometric survey, and RSGs in systems with non-B star companions. How we accounted for each of these biases is described below.

4.3.1 Initial Estimate

To produce the initial estimate of the binary fraction of RSGs with B-type companions based upon archival photometry and our spectroscopically observed LMC stars, we relied on a k-NN approach. This method is based upon the idea that stars with bluer colors and/or UV signal are more likely to be binary RSGs, which is something we've confirmed spectroscopically. The k-NN algorithm assigns probabilities of binarity to each of the remaining candidate stars that we did not spectroscopically observe by looking at how close they are in color-color space to the stars that have been spectroscopically confirmed. It follows that candidates with colors similar to known binaries are more likely to be binaries than those with colors similar to known single RSGs. This method allows us to calculate the percentage likelihood that each individual candidate is a binary RSG.

The input columns to the k-NN algorithm were all based on archival photometry including

Table 4.3. Spectroscopically Observed SMC Stars

2MASS	α_{2000}	δ_{2000}	K_s	σ_{Ks}	$J-K_s$	σ_{J-Ks}	U	B	V	Class.	RSG Component		
											$T_{\rm eff}[K]$	$\sigma_{T_{\rm eff}}$	Type
00473688-7304441	00 47 36.886	-73 04 44.18	8.319	0.024	1.147	0.033	15.603	14.734	12.736	RSG	3525	25	M2
00503842-7319359	00 50 38.420	-73 19 35.95	10.206	0.025	0.963	0.032	16.018	15.547	14.054	RSG+B	3825	100	K5-M0
00523496-7226017	00 52 34.968	-72 26 01.73	10.023	0.023	0.855	0.033	15.073	14.574	13.256	RSG	3875	100	K5-M0
00523564-7251053	00 52 35.650	-72 51 05.32	9.745	0.023	0.854	0.031	15.553	14.594	13.096	RSG	3875	100	K5-M0
00531772-7246072	00 53 17.729	-72 46 07.20	9.271	0.023	1.005	0.033	14.103	13.884	12.836	RSG	3800	100	K5-M0
00532528-7215376	00 53 25.290	-72 15 37.68	9.758	0.023	0.942	0.033	15.293	14.744	13.296	RSG+B	3850	100	K5-M0
00534156-7215268	00 53 41.563	-72 15 26.83	9.590	0.023	0.954	0.033	14.953	14.624	13.226	RSG	3900	100	K2-3
00534451-7233192	00 53 44.517	-72 33 19.21	9.462	0.020	1.021	0.030	14.563	14.464	13.226	RSG+Be	3725	25	K5-M0
00562532-7228182	00 56 25.324	-72 28 18.26	10.032	0.021	0.888	0.030	14.823	14.634	13.376	RSG	3950	100	K2-3
00585831-7213429	00 58 58.310	-72 13 42.93	9.837	0.021	0.923	0.032	13.463	13.894	13.066	RSG	3900	100	K2-3
00595187-7243351	00 59 51.870	-72 43 35.15	9.528	0.019	0.981	0.029	15.703	14.824	13.236	RSG+B	3875	100	K5-M0
01004445-7159389	01 00 44.454	-71 59 38.96	9.911	0.026	0.963	0.039	15.545	14.944	13.531	RSG+B	4050	100	K2-3
01012693-7201414	01 01 26.930	-72 01 41.43	9.235	0.024	0.991	0.034	14.863	14.434	12.926	RSG	3900	100	K2-3
01014357-7238252	01 01 43.579	-72 38 25.29	9.358	0.021	1.005	0.031	14.323	14.364	13.076	RSG+B	3900	100	K2-3
01020407-7226109	01 02 04.076	-72 26 10.90	9.420	0.023	1.035	0.033	14.623	14.614	13.286	RSG	3775	100	K5-M0
01024480-7201517	01 02 44.801	-72 01 51.75	9.386	0.021	0.954	0.030	15.613	14.634	12.986	RSG	3900	100	K5-M0
01033730-7158448	01 03 37.301	-71 58 44.88	9.598	0.020	0.962	0.030	15.013	14.484	13.096	RSG+B	3825	100	K5-M0
01033984-7239059	01 03 39.849	-72 39 05.93	10.362	0.021	0.969	0.032	16.065	15.436	13.955	RSG+B	3850	100	K5-M0
01034536-7207490	01 03 45.360	-72 07 49.03	9.639	0.025	0.959	0.034	14.963	14.764	13.386	RSG	3850	100	K5-M0
01061197-7214380	01 06 11.970	-72 14 38.00	10.072	0.019	0.901	0.029	14.633	14.484	13.346	RSG	4000	100	K2-3
01064766-7216118	01 06 47.669	-72 16 11.85	8.312	0.019	0.929	0.031			11.870	RSG	3750	25	K5-M0
01081478-7246411	01 08 14.787	-72 46 41.10	9.174	0.023	0.955	0.033	15.263	14.314	12.696	RSG	3850	100	K5-M0

Note. — J and K photometry from 2MASS. U, B, V photometry from Zaritsky et al. 2002.

U,B,V, and I photometry from Zaritsky et al. (2004) as well as the calculated $U-B$ and $B-V$ values. We opted not to include the 2MASS J and K photometry because the single and binary RSGs were evenly distributed throughout the CMD and thus the NIR colors did not provide any additional information that could help classify the stars. We additionally included a flag related to the brightness of the star in the NUV based upon survey data from the GALaxy Evolution EXplorer (*GALEX*) (Martin & GALEX Team, 2005; Morrissey et al., 2007; Bianchi, 2009). RSG+B star binaries should be bright in the UV given the B star companion while single RSGs should not. Thus, we hoped that the presence of NUV signal would help identify binaries. To determine whether the *GALEX* data is sensitive to the lowest luminosity B companions, we determined whether we would detect the flux of a reddened LMC A0V with a typical magnitude of 21.3 in the *GALEX* NUV filter. According to Simons et al. (2014), the *GALEX* NUV detection limit in the LMC is 22.7 mag and thus we are sensitive to even the lowest mass B star companions.

NUV images for each of the 4090 LMC RSGs were downloaded from the Mikulski Archive for Space Telescopes (MAST) and then simple aperture photometry was run to obtain an estimate of the star's brightness. The stars were then grouped into four categories based on their aperture photometry: no data at the specified coordinates (24%), data but no NUV signal detected (63%), dim NUV signal (6%), medium NUV signal (3%), and bright NUV signal (2%). The 76% with aperture photometry were then visually checked to confirm that the category (none, dim, medium, or bright) matched what was found in the images. While the *GALEX* data proved to be very useful when used in combination with the Zaritsky et al. (2004) photometry as part of the k-NN algorithm, it should be noted that there are issues present within the dataset. These are discussed in great detail in Simons et al. (2014) but revolve around the *GALEX* resolution being quite large at 5" and thus inadequate in the crowded OB associations. Thus, we've used the *GALEX* data as one small piece of our overall method of determining binarity, and not as the determining factor. Still, we do find that confirmed RSG+B star binaries are brighter in *GALEX* than the confirmed RSG single stars with 68% of the binaries with data showing either medium or bright NUV signal and

70% of the single RSGs showing either dim or no NUV signal. Additionally, as discussed above, not all photometry (including Zaritsky et al. 2004) is perfect. By using the k-NN approach and using inputs from different datasets in different passbands, we decrease the overall weight being placed on any individual measurement. Thus, we hope this will decrease erroneous results due to a single poor measurement of a star, for example.

To implement the k-NN algorithm, we relied on Python's SCIKIT-LEARN machine-learning package (Pedregosa et al., 2011). Our total number of spectroscopically confirmed RSG+B binaries included the 36 described here, as well as 10 discussed in Chapter 3, 4 found by Levesque et al. (2006) and 5 found by Dorda et al. (2018) bringing the total up to 55. For single stars, we included the 23 described here, as well as 217 other spectroscopically confirmed single RSGs described in Neugent et al. (2019); Levesque et al. (2006); Dorda et al. (2018) and our own unpublished AAT data described in Chapter 3. Thus, we had 295 stars we could use to both train and test our data. We first scaled our data using SCIKIT-LEARN's RobustScaler to account for the fact that our features (magnitudes/colors, and flags) are in different units. We then used k-fold cross-validation to train and test our model. We found that splitting our data up into 8 folds (as opposed to the default 5) achieved the highest accuracy when re-run against the test dataset. Thus, each of the 8 test sets contained around 7 binaries and 27 single RSGs. During testing, we found that we had the highest success using a k-NN search that looked at the nearest 26 neighbors weighted based on distance. Using this method, we achieved an accuracy of 93.5%.

We applied the k-NN algorithm to the 1457 stars in our sample with both $\log L/L_{\odot} > 4.0$ (our completeness limit) and a minimum of B and V photometry from Zaritsky et al. (2004). Figure 4.4 shows a color-color plot of both the original input sample of 295 spectroscopically observed stars and the results from the k-NN classification run. It has been color-coded to reflect the percent likelihood of each star being a binary with the bluer points representing binaries and the redder points representing single stars. Note that the "transitional-zone" is around a $U - B = 1$, which is what we had concluded empirically during our observations. Stars with $U - B$ colors smaller than 1 are more likely to be RSG binaries while stars with

Table 4.4. Percent Likelihood of Binarity

2MASS	U^a	B	V	I	$U-B$	$B-V$	NUV Flag[b]	Spec. Flag[c]	Binary %
04411972-6935466	18.17	16.33	14.55	12.87	1.85	1.78	0	0	0
04411983-7006575	17.71	16.08	14.48	12.84	1.63	1.60	0	0	0
04412336-6851303	17.88	16.09	14.45	12.77	1.80	1.63	0	0	0
04423661-6817567	16.87	15.61	13.77	11.49	1.26	1.84	3	0	14
04425441-6826500	16.27	15.82	14.21	12.31	0.45	1.62	4	0	23
04431303-6947187	18.37	16.54	14.93	13.03	1.84	1.60	4	0	3
04432439-6855342	17.64	15.54	13.78	11.84	2.09	1.76	4	0	0
04433893-6946464	18.09	16.23	14.50	12.89	1.86	1.73	0	0	0
04434250-6758042	17.64	16.19	14.15	11.54	1.46	2.03	4	0	0
04434290-6746555	17.35	15.68	13.82	11.92	1.67	1.86	4	0	0
04434579-6932204	17.55	15.37	13.74	11.88	2.18	1.62	4	0	0
04441164-6906054	17.46	15.22	13.45	11.67	2.24	1.77	0	0	0
04441474-6948013	17.95	15.98	14.23	12.57	1.96	1.75	4	0	0
04443117-7012430	17.77	15.43	13.64	11.93	2.34	1.80	0	0	0
04443612-7043022	16.24	15.36	13.80	···	0.88	1.56	4	0	46

Note. — This table is published in its entirety in Neugent et al. 2020a. A portion is shown here for guidance regarding its form and content.

[a] U,B,V, and I Photometry from Zaritsky et al. 2004.

[b] *GALEX* NUV brightness: 0 = n/a, 1 = bright flux, 2 = medium flux, 3 = dim flux, 4 = no flux.

[c] Spectra Flag: 0 = no spectra, 1 = spectra.

$U-B$ colors higher than 1 are more likely to be single RSGs. The input data and final percentage likelihoods for each star are shown in Table 4.4.

Since we assigned a percent likelihood of binarity to each individual candidate star, we could then get a first estimate of the binary fraction, before taking any biases into account. By simply summing up the percent likelihood of each star being in a binary system and dividing by the percent likelihood of each star being a single RSG we can estimate the binary fraction of RSG+B stars with $\log L/L_{\odot} > 4$ ($M >\sim 9M\odot$). After adding in the 295 spectroscopically confirmed stars, and taking the 93% accuracy rate of the k-NN algorithm into account, we arrive at a binary percentage of $13.5^{+7.56}_{-6.67}$% where the errors were calculated by assuming the most extreme scenarios given the 93% accuracy rate. However, as we discuss next, there are other factors to take into account that will increase this percentage slightly.

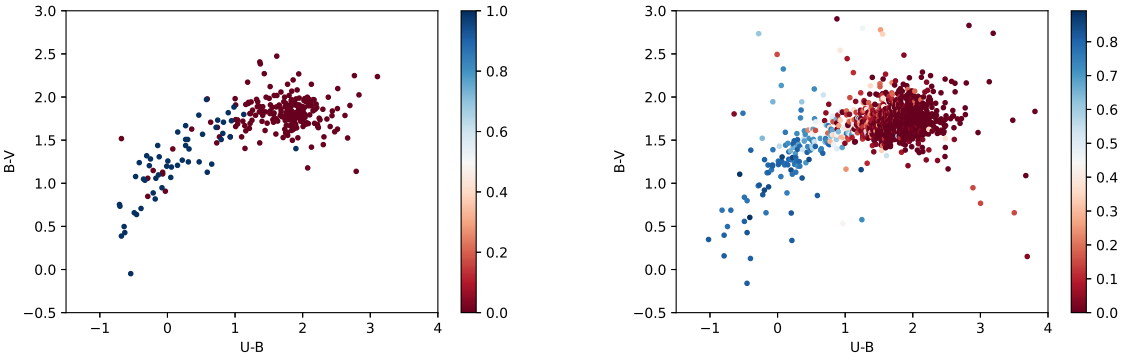

Figure 4.4 - Results from k-NN algorithm. The figure on the left shows the 295 spectroscopically confirmed single (red points) and binary (blue points) RSGs in color-color space. The figure on the right shows the results of the k-NN algorithm on the remaining candidate RSGs. The stars have been colored according to the percent likelihood of being a binary with the bluer points being more likely binaries and the redder points being more likely single RSGs. © AAS. Reproduced with permission from Neugent et al. (2020a).

4.3.2 Eclipsing Binaries

We additionally must consider eclipsing binaries since the majority of our binary fraction estimate is based upon single-epoch photometry. Take, for example, the Galactic RSG+B star binary system, VV Cep which has a 20.3 year orbit and is in secondary eclipse for 18 months, or around 7% of the time (Bauer & Bennett, 2000). If there are systems like VV Cep in our sample and the companion was behind the RSG when the photometry was obtained, these systems would not show up as binaries. Thus, we must account for this bias. If we had orbit determinations for our binaries, it would be possible to calculate this probability directly. However, since our classifications are based upon single-epoch spectroscopy, this is not possible. Instead we must make some assumptions about RSG binary systems and their orbits to determine what percentage of them are eclipsing at any given time. In the future, this calculation could hopefully be done independent of any modeling either by obtaining U,B, and V photometry at another epoch (in essence, repeating the work of Zaritsky et al.

2004), or a detailed analysis on the orbital parameters of our discovered RSG binaries. But at this point, this is outside the scope of the current work and thus can't be done observationally.

Instead, we turned to the BPASS models (v2.2.1) from Eldridge et al. (2017); Stanway & Eldridge (2018). We are grateful to J.J. Eldridge for help providing a program that allowed us to easily estimate the percentage of RSGs that would be in eclipse at any given moment. BPASS uses the findings of Moe & Di Stefano (2017) as initial conditions and then evolves the binary systems to populate appropriate binary companions to RSGs and determines (along with a host of physical properties) their periods, mass ratios, and separations at an LMC-like metallicity of $z = 0.008$. The maximum angle of inclination for eclipses is then computed based on the RSG's radius and the separation of the stars and then, for those that could possibly eclipse, the eclipse duration is determined. Simple Poisson errors were also estimated based on the number of eclipsing binaries. Based upon these calculations and the types of binaries we are sensitive to detecting, we estimate that $3.61 \pm 0.01\%$ of our targets that appear to be single RSGs are actually eclipsed binaries. (Note: Further information on how we ran BPASS to most closely align with our observations is discussed in Chapter 4.4.2). This increases the binary fraction slightly, but not substantially.

4.3.3 Line-of-Sight Pairings

One possible contaminant in our survey is line-of-sight pairings. These are stars where both the RSG and B star are genuine LMC members, but the B star isn't gravitationally bound to the RSG and instead just happens to exist in our line of sight to the RSG. In general, we expect these cases to be rare given the photometric quality checks we went through when selecting the original list of RSG candidates in 2MASS (stars with poor photometry flags, and thus possible visual pairings, were ignored), but the presence of a faint B star in the LMC foreground or background could still contribute Balmer lines to a spectrum. (For example, take LGGS J004453.06+412601.7 which Neugent et al. (2012a) classified as a WN+TiO. We originally thought this might be the first example of a RSG+WR binary system, but based on archival imaging we determined it is actually a M31 WR + foreground M dwarf

pairing). To determine the probability that each of our spectroscopically confirmed RSG+B star binaries are actually line-of-sight pairings, we ran a simple Monte Carlo simulation that took into account the OB star density around each of our confirmed RSG binaries.

Overall, the process worked as follows: for each of our confirmed LMC RSG+B star binaries, we found the locations of the OB stars within a 5' radius of the binary using B and V photometry from Zaritsky et al. (2004). We then ran a simulation that randomly placed a RSG within this region and checked to see if it fell within 1" of one of the OB stars. If it did, we flagged it as a line-of-sight pairing. The value of 1" comes from the size of our slit while observing on Las Campanas.

We opted to include both O stars as well as B stars in our simulation because, as described below, they are possible RSG binary companions, even if the likelihood is small. Also, given that we were relying on B and V photometry from Zaritsky et al. (2004), it is difficult to distinguish O and B stars from one another since their $B-V$ colors are nearly identical due to being on the tail end of the Rayleigh-Jeans distribution after having peak flux in the UV. To select the stars within the 5' radius of the binary, we removed everything redder than an A0V by using a cut at $(B-V) < 0.0$. We then took the average reddening of the LMC to be 0.13 from Massey et al. (2007b) and set the brightness limit of $V = 21$ since spectroscopically we wouldn't be able to observe the upper Balmer lines from OB stars fainter than that.

After running the simulation 10,000 times, we found that there was a $1.9 \pm 2.0\%$ chance that any of the observed RSG+B star binaries was actually a line-of-sight pairing (with 0% being the minimum and 10% being the maximum for any individual system). We additionally ran the program on the spectroscopically confirmed single RSGs and found a very similar distribution with a $1.6 \pm 1.7\%$ chance that any of the single RSGs could have a line-of-sight companion (again 0% was the minimum and 10% was the maximum). Given both the similarity between these two results and their low values, we believe that line-of-sight pairings have a negligible impact on the overall binary fraction.

4.3.4 RSGs+Other Companions

In Chapters 2 and 3, we argue that RSGs will primarily have B-type companions from an evolutionary point of view because longer-lived main sequence stars (A,G,K and M stars) won't have formed by the time a RSG is created. This same effect is seen observationally in clusters with well-studied stellar populations. For example, Hunter et al. (1995) surveyed R136, a bright star-forming region in the LMC, and found a large number of short-lived massive stars, but all stars with masses less than $2.8 M_{\odot}$ were still on the pre-main sequence. However, what about the shorter lived or non-main sequence stars such as O stars, YSGs, RSGs, WRs, etc.? From an evolutionary point of view, these systems are certainly possible. However, so far none have been observed and the lifetimes of such companion stars are so short that finding such a system is statistically unlikely. Here we delve deeper into each of these pairings and how their occurrence could alter our calculated RSG binary fraction.

The most likely system other than an RSG+B star binary is an RSG+O star binary, simply due to the longer duration of of an O star's time on the main sequence (a few million years) as compared to the later evolutionary stages (YSGs, RSGs, WRs, etc.) which last only tens to hundreds of thousands of years. Such a system would exist for a short period of time if two nearly equal mass stars were born together and one evolved into a RSG while the other was still on the main sequence. In terms of these stars biasing our calculated binary fraction, due to our photometric detection method, if any O star binaries do exist in the LMC, we've likely already detected them. The $U-B$ colors of O stars are nearly identical to that of B stars, so they would show up as candidates based on our k-NN algorithm (possibly even as higher likelihood candidates due to their lower $U-B$ values). We additionally would have been sensitive to them as spectroscopic candidates. Even though their upper Balmer lines have smaller equivalent widths, the stars themselves are brighter in U and their strong He I and He II lines would have shown up prominently. While none of our spectroscopically confirmed binaries appear to have O-type companions, our method of calculating the binary fraction is sensitive to such pairings.

Continuing on a massive star's evolutionary path are the even shorter-lived YSG and RSG stages. We admit that such systems would be difficult to detect and would likely only be observable if eclipsing or as a spectroscopic binary with some of the narrow metal lines (such as the Ca II triplet) appearing double. Again, since these pairings are statistically unlikely and have never been observed, we do not think they will effect our calculated binary fraction. However, we do point out that our method of detecting RSG binaries is not sensitive to such systems.

Next up are WR+RSG binary systems. We can confidently say that none of these have been detected in any of the nearby galaxies and furthermore, we don't expect to find any since the population of WRs in the LMC is thought to be complete (Neugent et al., 2018b). Since the discovery method for finding the WRs was based on their strong emission lines, any WR+RSG binaries would have been found as part of these galaxy-wide searches.

Finally, let's consider RSGs with neutron star or, in the case of more massive primaries, black hole companions. Such systems can occur if the RSG is originally the less massive of the two stars and the binary is not disrupted when the primary explodes as a supernova (SN). If the post-SN separation is too small, the systems will subsequently interact, potentially merging to create a Thorne-Żytkow object such as the candidate recently found in the SMC (Levesque et al., 2014). However, if the post-SN separation is wide enough, the secondary can expand into the RSG phase. While to the best of our knowledge only one RSG+compact object binary has been confirmed (Hinkle et al. 2020; discussed further in Chapter 5.3.3), and the majority of known high-mass X-ray binaries in the Magellanic Clouds have periods too short to allow the secondary to expand to the RSG phase (Haberl & Sturm, 2016; Antoniou & Zezas, 2016), there are a number of observational biases against detecting long-period systems. Indeed, RSGs have been identified as candidate counterparts/donor stars to several ultra-luminous X-ray sources (Heida et al., 2016; López et al., 2017) and recent high cadence time domain surveys are now facilitating the detection of non-interacting compact object systems (e.g. Thompson et al., 2019). Theoretically, both the rate of binary disruptions and the post-SN separation distribution are highly dependent on uncertain SN kick prescriptions

(e.g. Bray & Eldridge, 2018). However, using BPASS v2.2.1 using the methodology described in detail in Chapter 4.2.2, we estimate that $2.42 \pm 0.01\%$ of RSGs have compact object companions.

4.3.5 Final Binary Fraction

We are now in the position to estimate the final binary fraction of RSGs in the LMC. We initially planned our observations to be sensitive to RSG+B star companions given that B-type stars should dominate the sample based on evolutionary constraints. Though, we additionally point out that our selection criteria is sensitive to the less common O-type companions as well. Using the k-NN approach described above, we observationally estimate the RSG+OB star binary fraction as $13.5^{+7.56}_{-6.67}\%$. We then used BPASS to estimate both the fraction of eclipsing binaries ($3.61 \pm 0.01\%$) and RSG+compact companions ($2.42 \pm 0.01\%$) that we were not sensitive to in our search. Overall, we reach a final percentage of $19.5^{+7.6}_{-6.7}\%$ for RSGs with $\log L/L_{\odot} > 4$. These values are shown in Table 4.5. We stress that we are not including RSG+protostars in this calculation and that we are not sensitive to RSG+RSG or RSG+YSG systems, though from an evolutionary standpoint, these should be extremely rare. We expect from first principles that in order for a RSG+RSG system to exist even momentarily would require the two stars to be born with masses within 5% of each other; for the RSG+RSG to last for the majority of the RSG phase of the higher mass star, it would require an initial mass ratio q of 0.98-1.02. A more exact calculation is beyond the scope of the present work. In the next section we compare our results to expectations from BPASS for the total population as well as the binary fraction of other types of massive stars.

4.4 Discussion

Now that we've determined a binary fraction, we'd like to see where it fits within massive star observations and evolutionary theory. First we'll compare it to the binary fraction of other types of massive stars and discuss whether the number makes intuitive sense. Then we'll look at what the BPASS models predict, and finally we'll compare the physical properties

Table 4.5. Binary Fraction of LMC RSGs

Type of RSG Companion	Percent	Error
OB stars	13.5	+7.6/-6.7
in eclipse	3.6	±0.01
compact companions	2.4	±0.01
Total	19.5	+7.6/-6.7

of the single and binary RSGs before ending with a few words about our overall survey completeness.

4.4.1 Does this fraction match expectations?

As discussed in the Introduction, the binary fraction of long-period, non-interacting OB-star systems could be between 70-100% (Gies, 2008; Sana et al., 2012) with the short-period binary fraction being closer to 30-35% (Garmany et al., 1980; Sana et al., 2013). Since RSGs evolve primarily from OB stars, why is our calculated binary fraction of $19.5^{+7.6}_{-6.7}$% so much lower?

The key thing to remember is that RSGs have radii that are hundreds to even thousands of times the radius of the Sun. Two main sequence stars less than $30M_{\odot}$ in a binary system must have separations on the order of thousands of solar radii to not interact at some point before the more massive star turns into a RSG, thus creating a RSG binary system. As is discussed in Sana et al. (2012), binaries with orbital periods up to around 1500 days will exchange mass throughout their lifetime and, all except for one of the binary systems they measured had periods less than 1000 days (note: some of their rarity is a selection effect since long period systems are more difficult to detect spectroscopically but even in the "corrected"

sample set, there were few binaries with periods longer than 1000 days). Thus, the majority of these systems will interact before the more massive component turns into a RSG. When they interact, a few different things can occur. In close systems, RLOF will prevent the more massive star from ever turning into a RSG and a merger of the two OB-type stars might occur. In slightly more separate systems, the more massive star will turn into a RSG but then a merger between the evolved RSG and the un-evolved companion might occur.

In short period systems, the two stars will begin interacting as the more massive star evolves and grows in radius. However, RLOF will eventually occur and the more massive star will be stripped of its entire envelope, losing much of its original mass. The secondary will then gain mass and angular momentum but neither will evolve into the RSG stage. As is discussed in Sana et al. (2012), it is estimated that 40-50% of O-star binaries will have their evolution altered due to RLOF.

In the case of a merger at the RSG phase, the binary system starts off with two main sequence stars. Over time, the more massive star evolves first and eventually turns into a RSG with a companion. If the two stars are close enough, they will influence each other's orbits, begin spinning up, and transfer angular momentum. Once they merge, the RSG will photometrically appear single (though with a much higher rotational velocity). From photometry alone, a merged single star will generally be indistinguishable from an always-single star. While a RSG merger hasn't been directly observed, it has been hypothesized as an explanation for why one of the most famous RSGs is spinning so fast. Betelgeuse has a projected rotational velocity of around 15 km s^{-1}, much higher than that of a normal RSG. Wheeler et al. (2017) suggest that this increased velocity could be due to a past merger with a smaller mass companion. Sana et al. (2012) estimate that 20-30% of massive, apparently single stars, are actually the result of mergers.

Taking an initial O star binary fraction of 70% and considering both mergers (20-30% of binaries) and RLOF (40-50% of binaries), our estimated binary fraction of $19.5^{+7.6}_{-6.7}$% is well in accord with the broad model predictions done by Sana et al. (2012). Additionally, if we look at Fig. 1 (left) in Sana et al. (2012), we see that $\sim$ 15% of the O star systems have

periods longer than 1000 days, and thus would likely turn into RSG binary systems after the more massive star has evolved. This percentage is very well aligned with our findings.

4.4.2 Comparison with BPASS Models

As discussed earlier, we used BPASS v2.2.1 (Eldridge et al., 2017; Stanway & Eldridge, 2018) to calculate the percentage of eclipsing binaries and RSG+compact companions. Here we go into a bit more detail about these BPASS simulations and compare the binary fraction we found to the BPASS results.

To ensure a fair comparison between our results and that of BPASS, we used our photometric selection criteria transformed to $T_{\rm eff}$ and $\log L/L_{\odot}$ (as described in Chapter 4.1.4) to select model RSGs. We additionally placed a minimum mass constraint ($M > 8M_{\odot}$) on the RSG and minimum luminosity of $\log L/L_{\odot} > 4$. Using these two selection methods, we believe we've separated out the AGB stars in the BPASS models at least as well as we've done photometrically. Given these constraints, the BPASS models predict that 31% are single RSGs, 25% are merged RSGs, 2% are RSGs + compact objects (as discussed above), and the remaining 42% are RSG + main sequence star binaries (all percentages have Poisson errors $< 1\%$) at an LMC-like metallicity of $z = 0.008$. So, why the factor of 2 discrepancy?

The primary reason is that BPASS is a stellar evolution and population synthesis code and does not deal with star formation (yet!). Thus, all stars arrive on the zero age main sequence (ZAMS) at the same time, regardless of their mass. When taking the types of stars that might exist in binary systems with RSGs into account, BPASS uses the prescription given by Moe & Di Stefano (2017) without considering whether these stars would have arrived on the ZAMS by the time the RSG was formed. Due to the initial mass function (IMF) favoring lower-mass stars, this adds a significant number of low-mass companions.

Using the BPASS models, we can plot an HR diagram of the companions, as is shown in Figure 4.5. From Cox (2000) we know that a B8V has a $\log L/L_{\odot} \sim 2.5$ and an B0I has a $\log L/L_{\odot} \sim 5.5$. Thus, we can make cuts in the BPASS companions to determine the percentage of binaries with O, B and less luminous companions. We find that, as expected

based on lifetimes alone, O-type companions are exceedingly rare and make-up just 1% of the binaries. The majority (74%) are B-type stars, and the remaining 25% are stars that wouldn't have reached the ZAMS before the formation of an RSG. Thus, we can conclude that 25% of the RSG binaries estimated by BPASS are most likely single RSGs. This brings the BPASS-estimated binary fraction down to 32% which includes RSGs with O and B-type companions, compact companions, and eclipsing systems. Since our calculated fraction is lower, this may suggest (again) that either the merger fraction is underestimated or the initial OB binary fraction is overestimated.

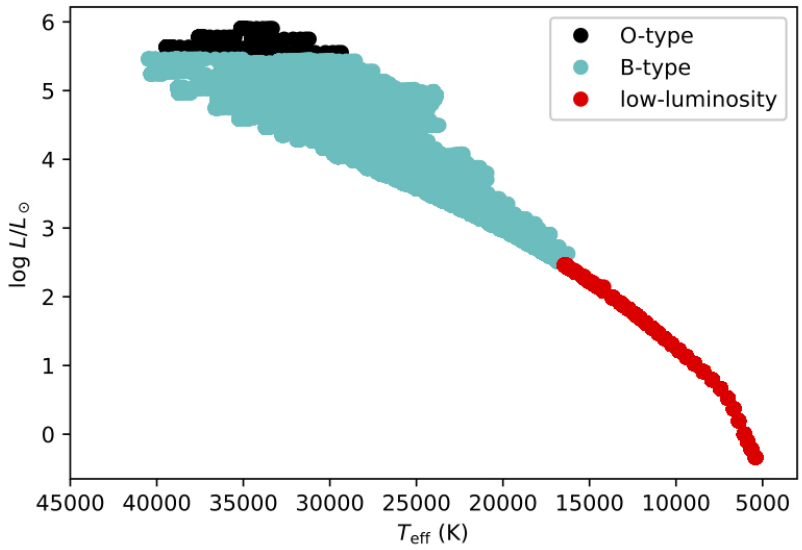

Figure 4.5 - HR Diagram of RSG binary companions from BPASS v2.2.1. The O-type stars (black dots) make up less than 1% of the sample, as is to be expected based on their short lifetimes while the B-type stars (cyan dots) make up the majority (74%) of the sample. The lower luminosity stars (red dots) below a $\log L/L_\odot = 3.5$ will not have reached the ZAMS by the time the lowest mass RSG has formed and thus do not make viable companions.

4.4.3 Completeness Issues

There were six additional stars we observed spectroscopically that were not included in the binary fraction calculations for various reasons. Each of these reasons points to a possible completeness issue (field size, 2MASS flag requirements, and color-cuts), which we discuss in detail below. However, we believe that each of these issues will simply lower our sample's overall completeness of RSGs in the LMC, but should in all cases impact binaries and single stars in the same manner, thus having negligible impact on our final binary fraction.

As described in Chapter 4.1.1, we chose to select RSGs within a well-defined region of the LMC centered on $\alpha_{\rm J2000}$=05:18:00 and $\delta_{\rm J2000}$=-68:45:00 and extending in radius by 210'. This region was chosen based on our previous survey of WRs in the LMC and because it covers the entire optical disk of the galaxy. However, while we believe this region encompasses the majority of RSGs within the LMC, there are certainly a few outside of this region. Two such examples are 2MASS stars 04415417-6727202, a confirmed RSG+B star binary, and 05535411-6647126 a single RSG. As discussed recently by Nidever et al. (2019), the size of the LMC is an ongoing topic with fainter stellar streams being found continuously. While our radius selection means that we've missed some of the RSGs on the outskirts, there is no physical reason why we would be missing single stars or binaries preferentially and thus, this doesn't alter the determined binary fraction.

When selecting candidates using 2MASS, we additionally only kept those with the best photometry (quality flags of "AAA," and "artifact contamination" flags of "000"). However, based on lists included in Dorda et al. (2018), we observed two candidates with lower quality flags. 2MASS star 05254453-6616228 had a flag of EAA and turned out to be a RSG+B binary and 05402532-6915302 had a "ddd" flag and is a single RSG. As with our size selection, our method of choosing flags will hinder our completeness since we will miss a few RSGs with sub-standard quality flags, but binaries and single stars will be equally incomplete and thus this will not change the binary fraction.

Finally, there are two stars that fell outside our color cuts in K and $J-K$. These cuts

are always going to be difficult to execute perfectly due to uncertain star-by-star reddening values and thus it is not unexpected that there will be a few RSGs a bit redder than our cut or even one or two a bit bluer, such as the early K-type stars. Two examples are the single RSG 05312818-6703228 which was slightly too blue with a $J-K$ of 0.916 instead of the required 0.917 and the binary RSG 05401638-6659303 which was a little too red. To verify that our $J-K$ cuts weren't altering our overall binary fraction, we measured the fraction as a function of $J-K$ and found it to be constant to within our errors.

We also wanted to assess whether the ambiguous *Gaia* data might have changed our completeness rate or the binary fraction. There were initially 3,585 stars in our sample with ambiguous results (4.1%). After filtering out AGBs, and making the appropriate color cuts, only 4 stars remained in our sample with $\log L/L_{\odot} > 4$. Two of them were spectroscopically confirmed LMC RSGs and the remaining two were classified as single RSGs by the k-NN algorithm. The classification of these two stars, even if they turn out to be foreground red dwarfs, will not change our final binary fraction.

4.5 Brief Summary

Here we observationally constrained the RSG binary fraction in the LMC to $19.5^{+7.6}_{-6.7}\%$ for stars with $\log L/L_{\odot} > 4$ corresponding to RSGs $> 9M\odot$. We did this by first identifying a complete sample of LMC RSGs using 2MASS NIR color-cuts and filtering out foreground stars using *Gaia*. In total we identified 4090 RSGs with $\log L/L_{\odot} > 3.5$ and 1820 with $\log L/L_{\odot} > 4.0$, which we believe to be our completeness limit. We then observed a sample of these spectroscopically to confirm their single vs. binary status. Since the binaries will have excess flux in the blue coming from the B star component, we then used photometry to determine binarity. Combining U, B, V and I photometry from Zaritsky et al. (2004) and NUV brightness from *GALEX*, we used a k-NN approach to estimate the binary fraction of RSGs using our spectroscopic sample as a training set. From this approach we calculated a base binary fraction of RSG+OB stars as $13.5^{+7.56}_{-6.67}\%$. Our observations were not sensitive to either binaries in eclipse or RSGs in systems with compact companions so we used BPASS

to calculate these percentages as $3.61 \pm 0.01\%$, and $2.42 \pm 0.01\%$, respectively. Overall, we reach a final percentage of $19.5^{+7.6}_{-6.7}\%$ for RSGs with $\log L/L_{\odot} > 4$. This percentage does not include RSGs in systems with protostars or the rare case of RSGs in systems with other RSGs or YSGs. We then compared our result to what was discussed in Sana et al. (2012) and BPASS v2.2.1 modeling results. Our results are consistent with the broad expectations based on Sana et al. (2012) binary fractions, but slightly lower than the 32% predictions by detailed calculations of BPASS. Next we will investigate the effect a changing metallicity has on the RSG binary fraction.

Chapter 5

THE RSG BINARY FRACTION IN M31 AND M33

To investigate the RSG binary fraction as a function of metallicity and extend the results from the last chapter further, I've focused my efforts on the RSG content of M31 and M33 for several reasons. First, these two galaxies are close enough that we can observe a *complete* sample of RSGs down to a limiting luminosity. This is something we are unable to do in our own Milky Way because our location within a spiral arm makes it impossible to observe the majority of the Galaxy's RSGs given high extinction within the Galactic plane. Secondly, we've recently obtained NIR photometry of both M31 and M33 that allows us to identify a complete sample of RSGs and thus accurately compute the binary fraction (Massey et al., 2021). Finally, and most importantly, the combination of M31 and M33 allow us to target a large metallicity range from $\log(O/H)+12 = 8.3$ in the outer regions of M33 (Magrini et al., 2007) to $\log(O/H) + 12 = 8.9$ in M31 (Sanders et al., 2012) (see a deeper discussion about the caveats behind these values in Chapter 6.3). This allows us to carefully investigate the effects of metallicity on the RSG binary fraction by just observing two galaxies.

While a large portion of this work focuses on the science related to identifying and confirming RSG binaries within M31 and M33, it would be impossible to determine the binary *fraction* without also understanding the total RSG content within each galaxy. Thankfully, Massey et al. (2021) recently used archival NIR photometry in M31 and M33 to identify a complete sample of RSGs down to a limiting luminosity of $\log L/L_{\odot} \geq 4.0$. Overall, they used a similar method to the one discussed in Chapter 4 when selecting LMC RSGs. They began by removing foreground stars using Gaia parallax and proper motion values (Gaia Collaboration et al., 2018) and then excluded asymptotic giant branch (AGB) stars due to their redder colors on the CMD and overall dimmer magnitudes. Finally, they transformed

the NIR colors to effective temperature and luminosities before creating a final list of 7585 and 3911 RSGs in M31 and M33, respectively. This catalog serves as a starting point to calculate the binary fraction of RSGs in these two galaxies.

5.1 Spectroscopically Confirmed RSG+B Binaries

We previously discovered 63 RSG+B star binaries in M31 and M33 as discussed in Chapter 3. Here I describe the selection of additional candidates, their followup spectroscopic confirmation, and the overall observed RSG binary sample used to determine the RSG+OB[1] binary fraction.

5.1.1 Selection Criteria

Overall, we expect RSG+OB binaries to have excess blue light originating from the OB star companion as compared to single RSGs. Thus, the spectral energy distribution (SED) of a binary RSG will appear flatter than that of a single RSG given the excess flux in the blue. This allows us to define a set of photometric color cuts that can be used to select RSG+OB binaries based on both observed single RSG and OB-type stars as well as synthetic RSG+OB star binaries modeled using the MARCS RSG spectral models (Plez et al., 1992) in combination with the BSTARS06 spectral models (Lanz & Hubeny, 2007). As discussed in Chapter 2, we used this information to define a set of color-color cuts in $U-B$ and $R-I$ that could be used for selecting RSG binaries.

Ideally, candidate RSG+OB binaries would have been selected as a subset of the M31 and M33 RSGs from Massey et al. (2021) that had excess flux in the blue. This is the method discussed in Chapter 4 that we used to select RSG binary candidates in the LMC. However, at the time of the 2019 spectroscopic observations (detailed below), the photometry

[1]So far, we've only detected *B-type* companions spectroscopically, but the method is also sensitive to RSG+O star binaries. However, due to the initial mass function, RSG+O star binaries should be much rarer as discussed above (also see discussion in Chapter 4). Still, I have tried to use RSG+B when explicitly discussing the binaries we've observationally detected but RSG+OB when discussing the sensitivity of the method.

described by Massey et al. (2021) was not available. Instead, I relied on photometry from a variety of photometric surveys to select RSG binary candidates. The methods used to select candidates therefore differed slightly based on the initial photometric catalog. In all cases, I set a limiting V magnitude of 20 (it is not possible to observe fainter RSGs spectroscopically with sufficient S/N), and removed the crowded stars as dictated by the "X" flag in the Local Group Galaxy Survey (LGGS, Massey et al. 2006, 2016).

The initial candidate list for M31 and M33 was described in detail in Chapter 2 and was selected only based on LGGS $U-B$ and $R-I$ photometry. It contained 138 potential binaries in M31 and 142 in M33. As discussed in Chapter 2, the assumption was that in this region of color-color space, contamination by other types of stars was small and all sources with these colors should be RSG+OB binaries. Follow-up observations of 149 of these candidates were discussed in Chapter 3 which lead to the discovery of 63 new RSG binary systems. They additionally identified a host of non-stellar contaminants such as QSOs and galaxies (Massey et al., 2019). However, the majority of the observed candidates were either RSGs, B-type stars or RSG+B type binaries. Thus, the remaining 131 candidates in M31 and M33 are included as candidates for spectroscopic confirmation.

Although the final selection of M33's RSGs described in Massey et al. (2021) had not been completed, preliminary results were used to select stars for spectroscopic follow-up. There were two main differences between the preliminary and the final lists of RSG candidates. First, the preliminary cut took the UKIRT WFCAM source classification flags more stringently, insisting that all sources be described as "stellar" on both the J and K_s list. Subsequent examination showed that these flags were not always consistent; i.e., the same object might be described as stellar on some but not all frames. Inspection of the frames revealed that this resulted in some valid sources being excluded in the preliminary list. Secondly, the position of the RSG region was refined in the color-magnitude diagram for the final list. In the UKIRT photometry of a few regions in M31 as discussed in Chapter 7, the blue cut-off line for RSGs was defined as parallel to the red cut-off line, following the same procedure used by Yang et al. (2019) for selection of RSGs in their SMC catalog. However,

as argued in Massey et al. (2021), there is no physical basis for this. Instead, the blue cutoff has been redefined as a vertical line. Foreground stars were removed using Gaia results in much the same way as ultimately used for the final list, although some refinements were made (Massey et al., 2021). After cross-matching this list of M33 RSGs with the LGGS, I opted to keep all RSGs with $U - B < 1$, similar to what was done for the LMC binary candidates in Chapter 4. This resulted in some of the RSG binary candidates falling outside the region of $U - B$ vs. $R - I$ color-color space initially defined for candidate selection. But, with the addition of NIR photometry, I was curious to learn more about the nature of these RSGs with excess blue flux. After these photometric cuts, 182 candidate RSG binaries remained in M33. Of these stars, 134 of them were new additions and the remaining 48 were duplicates from the candidates described in Chapter 2. Combined with the 63 additional candidates from Chapter 2, I identified 245 RSG binary candidates in M33.

Selecting RSGs in M31 was a bit more complicated as I did not yet have access to the NIR photometry as described in Massey et al. (2021). Instead, I relied on a combination of the RSGs identified using NIR photometry in a small portion of M31 as described in Chapter 7 and the 2MASS 6× "long exposure" M31 photometry which goes around 1 magnitude deeper than the standard 2MASS survey (Skrutskie et al., 2006). Both of these lists were cross-matched with Gaia to remove foreground stars using the method described in Chapter 7. Again, they were cross-matched with the LGGS and a cut was made for stars with $U-B < 1$. In total, we identified 214 new RSG binary candidates in M31. When combined with the remaining 36 candidates from Chapter 2, I identified 250 RSG binary candidates in M31.

The location of the 245 M33 candidates and 250 M31 candidates within $U - B$ vs. $R - I$ color space are shown in Figure 5.1. Additionally plotted are the known RSG binaries, single RSGs and single B-type stars previously spectroscopically confirmed and described in Chapters 2 and 3.

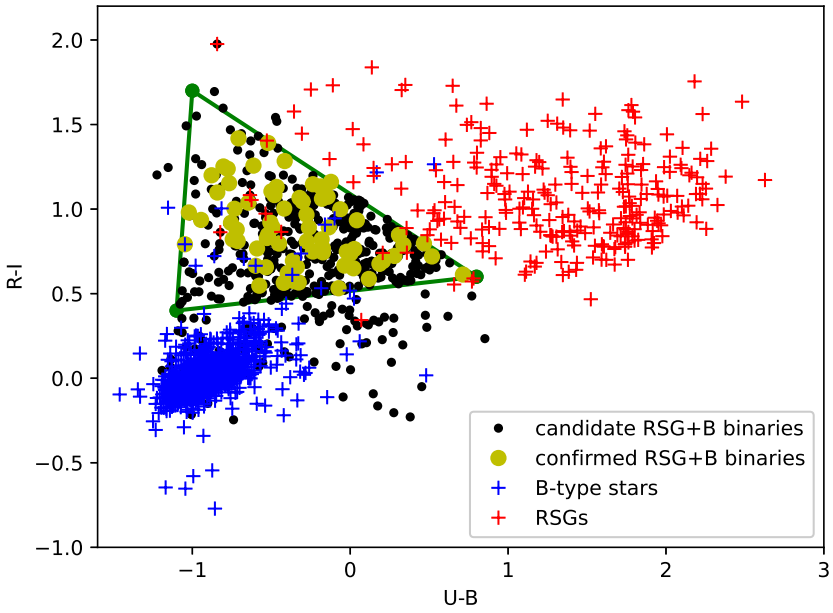

Figure 5.1 - $U-B$ vs. $R-I$ color-color plot of candidate RSG binaries in M31 and M33. The blue and red +s represent the LGGS photometry from spectroscopically confirmed B-type stars and RSGs, respectively. The yellow dots are the spectroscopically confirmed RSG+B star binaries discussed in Chapter 3. The green lines represent the region in $U-B$ and $R-I$ space that we based our initial candidate list off of using only the LGGS photometry. The vertices of the three green points in $U-B$ vs. $R-I$ color space are (-1.1,0.4), (0.8,0.6), and (-1,1.7). Finally, our candidate M31 and M33 RSG+B star binaries are shown as black points. For stars with NIR photometry that could be used to classify them as RSGs, we allowed all values of $R-I$ but restricted the candidates to those with $U-B<1$. This is why there are some candidates that fall outside of the green triangle.

5.1.2 Observations and Reductions

Observations were carried out using the multi-object, fiber-fed spectrograph Hectospec (Fabricant et al., 2005) on the 6.5-m MMT located near Tucson, AZ. Collaborator P. Massey and I were assigned 1.5 nights of queue-scheduled dark time in Fall 2019 through the Arizona Time Allocation Committee. However, due to poor weather and an instrument failure, only a single M31 and a single M33 configuration were observed (one third of what we were hoping to obtain). The M31 field was observed on UT 2019 September 5 and the M33 field was observed on UT 2019 October 22 through clear sky conditions with exposure times of 3×3000 seconds. The data were taken with the 270 line mm^{-1} grating that yields a spectral coverage from 3700 - 9000 Å. Each of the 300 fibers is 250 μm which provides a spectral resolution of 6Å. Reductions were carried out using v2.0 of the Hectospec REDuction (HSRED) code[2].

5.1.3 Results

As part of the Fall 2019 observing run, 203 of the 495 new RSG binary candidates were spectroscopically observed in M31 and M33. Of these, 124 (61%) of them turned out to be RSG+B star binaries (60 in M31 and 64 in M33), 38 (19%) are single RSGs (21 in M31 and 18 in M33), 20 (10%) only show upper Balmer lines (8 in M31, 12 in M33), and the remaining 21 (10%) were other accidental discoveries (3 QSOs, 7 H, II regions, and the remaining with poor S/N). Combining this with the sample discussed in Chapter 3, this brings the total number of RSG+B star binaries known in M31 up to 88 and in M33 to 94. Further information about these spectroscopically observed stars, their LGGS photometry, and classifications, can be found in Table 5.1.

5.2 Classifying RSGs as Single or Binary

Thanks to the recent work done by Massey et al. (2021), the RSG content of both M31 and M33 is now well defined. Here I describe how I used a k-NN algorithm to classify RSGs

[2]See, `http://www.mmto.org/hsred-reduction-pipeline/`.

Table 5.1. Spectroscopically Observed M31 and M33 Stars

LGGS Designation[a]	α_{2000}	δ_{2000}	V	$B-V$	$U-B$	$V-R$	$R-I$	Classification
J003744.37+400401.5	00:37:44.36	+40:04:01.4	19.783	1.528	0.384	0.675	0.578	RSG
J003848.43+400432.4	00:38:48.42	+40:04:32.3	19.169	1.571	0.380	0.481	-0.229	RSG
J004059.67+402049.6	00:40:59.66	+40:20:49.5	18.881	1.343	0.484	0.642	0.738	RSG
J004156.45+402004.5	00:41:56.44	+40:20:04.4	19.145	1.587	0.217	0.609	0.361	RSG
J004239.02+413643.2	00:42:39.01	+41:36:43.1	19.667	0.482	0.289	0.275	0.572	RSG+B
J004248.13+414714.5	00:42:48.12	+41:47:14.3	18.895	1.193	-0.367	1.091	1.177	RSG+B
J004248.94+414035.3	00:42:48.93	+41:40:35.1	19.532	0.966	-0.710	0.848	0.884	RSG
J004306.93+413808.1	00:43:06.92	+41:38:08.0	19.748	0.847	-0.228	0.535	0.545	OB
J004307.61+415103.8	00:43:07.60	+41:51:03.6	19.705	1.083	-0.489	0.823	0.798	RSG+B
J004307.87+413407.6	00:43:07.86	+41:34:07.5	19.196	1.038	0.415	0.728	0.690	RSG
J004315.34+414242.0	00:43:15.33	+41:42:41.8	19.966	0.276	-0.221	0.371	0.704	RSG+B
J004319.73+414033.3	00:43:19.72	+41:40:33.1	18.725	0.899	-0.115	0.523	0.546	OB
J004332.51+415232.0	00:43:32.50	+41:52:31.8	19.747	0.809	-0.425	0.711	0.766	RSG+B
J004334.40+414915.9	00:43:34.39	+41:49:15.7	20.243	0.841	-0.485	0.872	0.975	RSG+B
J004340.58+412550.0	00:43:40.57	+41:25:49.9	18.952	0.513	-0.322	0.476	0.525	RSG+B

Note. — This table is published in its entirety in Neugent 2021. A portion is shown here for guidance regarding its form and content.

[a]All photometry is from the LGGS; Massey et al. 2006

that were not observed spectroscopically as either single or binary following the procedure initially outlined in Chapter 4.

5.2.1 The Initial Sample

The initial set of RSGs was selected photometrically based on NIR colors as described by Massey et al. (2021). While the overall process of removing foreground stars using Gaia, and then defining appropriate J and $J-K$ color cuts was the same for both galaxies, the resulting datasets have their own slight differences and caveats. For this reason, I'll discuss both M31 and M33 separately below. One prominent difference between the initial sample used here for M31 and M33 vs. the initial sample discussed in Chapter 4 for the LMC is that the limiting luminosity has been changed from $\log L/L_\odot \geq 4.0$ to $\log L/L_\odot \geq 4.2$. This is primarily due to increased crowding in the inner regions of M31 (see further discussion in Massey et al. 2021). To keep the comparisons consistent across galaxies, I've thus adjusted all of the RSG lower luminosity completeness limits to $\log L/L_\odot \geq 4.2$, corresponding to a $\sim 10 M_\odot$ initial solar mass star.

M33

Starting with the list of M33 RSGs presented by Massey et al. (2021), and selecting those with $\log L/L_\odot \geq 4.2$, yielded 1970 RSGs. Since I later rely on LGGS photometry for the k-NN classification, I additionally selected M33 RSGs that were within the LGGS survey area. This limited me to the 1702 RSGs with $\rho < 1$ where ρ, the galactocentric distance, assumes a Holmberg radius of 30.8 arcminutes, an inclination of 56.0°, and a position angle of the major axis of 23.0°. At a distance of 830 kpc (van den Bergh, 2000), $\rho = 1$ corresponds to 7.44 kpc. These 1702 stars formed my initial list of M33 RSGs to classify as either single or binary.

After spectroscopically confirming 94 total RSG+B star binaries in M33, I was now left with 65 after removing 12 binaries with $\log L/L_\odot < 4.2$, 5 with $\rho > 1$, 6 that Gaia suggests as possible foreground stars, and 6 that are a bit too yellow to be classified as RSGs. Using

spectra from Drout et al. (2012); Massey (1998), and our own Hectospec data described above and in Chapter 3, I additionally classified 230 RSGs as single. Thus, 17% of our initial M33 RSGs have been spectroscopically confirmed as either binary or single.

Of these 1702 RSGs, 80% have LGGS counterparts and thus B, V, and R photometry. The remaining 218 stars are primarily in crowded regions where the LGGS was not able to accurately distinguish individual stars (see Massey et al. 2021 for more explanation). However, as described below, I was able to supplement the LGGS dataset with additional photometry to help classify many of the stars without LGGS data. Of the 1364 stars with LGGS photometry, 996 (73%) additionally have U photometry which greatly helps when classifying the stars as binary vs. single due to the excess blue flux.

M31

I followed a similar process for M31, but soon realized that the effects of crowding were much more pronounced in M31 than they were in M33 or the LMC. To reduce issues with crowding, I removed stars in the innermost portion of M31 with $\rho < 0.1$. I additionally limited stars to those with $\rho <= 0.75$ to constrain the survey area to approximately what was covered by the LGGS. In M31, ρ was computed assuming a Holmberg radius of 95.3 arcminuntes, an inclination of 77.0°, and a position angle of the major axis of 35.0°. At a distance of 760 kpc (van den Bergh, 2000), $\rho = 1$ corresponds to 21.07 kpc. After making the luminosity and ρ cuts, I was left with 1909 RSGs in M31.

Of the 88 spectroscopically confirmed RSG+B star binaries in M31, only 43 were in this subset. As with M33, the removals were due to $\log L/L_{\odot} < 4.2$ (11 stars), ρ out of limits (15 stars), foreground classification (5 stars), and outside RSG color limits (14 stars). The large number of spectroscopically confirmed binaries outside of the color range is due to excess reddening in M31, as discussed later. I additionally suspect the stars removed as foreground stars due to Gaia classifications are likely members based on Ca II triplet radial velocity measurements. However, these stars have still been removed from the binary fraction calculation for consistency's sake. An additional 183 spectroscopically confirmed single RSGs

from Massey (1998); Massey & Evans (2016), the Hectospec data described above and in Chapter 3 brought the total number of M31 RSGs with spectra to 226, or 12%.

Crowding and extinction issues in M31 also decreased the number of RSGs with LGGS counterparts. Out of the 1909 RSGs, only 76% have LGGS B, V, and R photometry. As I discuss later, high reddening in certain parts of M31 may lead to additional issues, and thus I later calculate the binary fraction of RSGs in M31 for both the entire galaxy and just in the less reddened regions.

5.2.2 UV Photometry

RSG+OB binaries should have strong flux in the UV compared to single RSGs which have relatively little signal at such short wavelengths. Thus, similar to what we did in Chapter 4 with the UV Galaxy Evolution Explorer (GALEX; Simons et al. 2014; Martin & GALEX Team 2005; Morrissey et al. 2007) data in the LMC, I cross-matched the M31 and M33 RSGs with photometry from the Panchromatic Hubble Andromeda Treasury (PHAT) dataset (Dalcanton et al., 2012) and the soon-to-be-published Panchromatic Hubble Andromeda Treasury: Triangulum Extended Region (PHATTER) dataset (Williams et al., 2021). Due to the vastly increased spatial resolution of the PHAT and PHATTER data compared to our ground-based NIR photometry, cross-matching was slightly more complicated than just taking the closest match in coordinates. Instead, I searched for the closest star within 0.5" that had a similar F110W magnitude to the RSG's J magnitude. While the HST F110W and 2MASS J bandpasses aren't identical, this method proved quite successful based off a visual check of a random set of around 100 RSGs.

By including both the PHAT and PHATTER data, I was able to add UV photometry to a set of stars that previously only had LGGS visible and NIR photometry. There were also a small number of RSGs without LGGS photometry that instead had PHAT or PHATTER photometry and thus could be classified as a single or binary RSG. In M31, 314 of our RSGs had matches in PHAT with 72 of them having no LGGS match. In M33, 696 had matches in PHATTER with 60 of them having no LGGS match. The number of stars with photometry

from each survey is shown in Table 5.2.

5.2.3 k-NN Classification

To calculate the observed RSG+OB star binary fraction, I relied on a k-NN approach, much as was done in Chapter 4 for the LMC RSGs. The rational behind this approach is that RSGs with OB star companions should appear photometrically different from single RSGs due to their increased flux in the blue. Using our spectroscopically confirmed RSG binaries and single stars and their corresponding photometry as inputs, the k-NN algorithm assigns a probability of binarity to each of the remaining RSGs. RSGs with colors similar to spectroscopically confirmed RSG binaries are assigned a higher probability of being a binary than RSGs with colors similar to spectroscopically confirmed single RSGs.

The k-NN algorithm was implemented using Python's SCIKIT-LEARN machine-learning package (Pedregosa et al., 2011). I trained and tested the data using k-fold cross validation of the spectroscopically confirmed stars mentioned above after scaling the data using SCIKIT-LEARN's RobustScaler. For both M31 and M33, there were essentially three different datasets to classify: those with just LGGS photometry, those with LGGS and HST (either PHAT or PHATTER) photometry, and those with just HST photometry. Then there were the remaining stars with neither LGGS or HST photometry that could not be classified using the k-NN algorithm. The input parameters for the k-NN algorithm (including the number of folds and neighbors used), star counts, and the accuracy rates (as determined by the SCIKIT-LEARN GridSearchCV scoring algorithm) are shown in Table 5.2.

A visual representation of the k-NN classification results is shown in Figure 5.2 where the individual points are color-coded based off their likelihood of having an OB-type companion (bluer points correspond to higher likelihood). The two figures on the left show the $U-B$ and $B-V$ colors of the initial spectroscopically confirmed RSG+B binaries and single RSGs for both M31 and M33. As expected, the RSG+B binaries show excess blue flux coming from the B-type companion and thus their $U-B$ colors are more negative. The two figures on the right show the results of the k-NN classification algorithm. Note that, as with the

Table 5.2. k-NN Parameters

Galaxy	LGGS	HST	# binary RSGs	# single RSGs	# unknown RSGs	# folds	# neighbors	Accuracy %
M31	✓	✓	43	186	209	4	10	91.0
M31	✓		43	186	1009	4	13	98.7
M31		✓	9	24	72	4	8	76.4
M31			...	...	390	...	...	...
M33	✓	✓	65	230	593	4	15	94.3
M33	✓		65	230	708	7	10	94.3
M33		✓	18	25	60	6	10	80.0
M33			...	...	46	...	...	...

LMC dataset described in Chapter 4, the "transition" period between a RSG having an OB-type companion is around a $U - B = 0$. RSGs with $U - B$ values higher than this are almost always single RSGs and those with $U - B$ values lower than this likely have an OB-type companion. An additional constraint can be made with $B - V$ values as RSGs with $B - V > 1$ appear much more likely to be single RSGs. An interesting aspect of the M31 plot to note is the cluster of classified RSGs with both $U - B$ and $B - V$ values between 0 and 1 (see upper right plot). Stars with these colors were not observed spectroscopically (see upper left plot) and yet a large number of them exist. This highlights the effect highly reddened regions can have on the photometry and the need to be careful when selecting stars to use to determine the overall observed binary fraction.

5.2.4 Completeness Issues

As with any observational survey, there are completeness issues that must be addressed. For this particular survey, there are two primary concerns. The first is that the survey didn't detect the correct total number of RSGs and the second is that the survey didn't detect the correct number of binaries. Here I discuss both concerns.

For this research, I am concerned with the binary *fraction* of RSGs in M31 and M33.

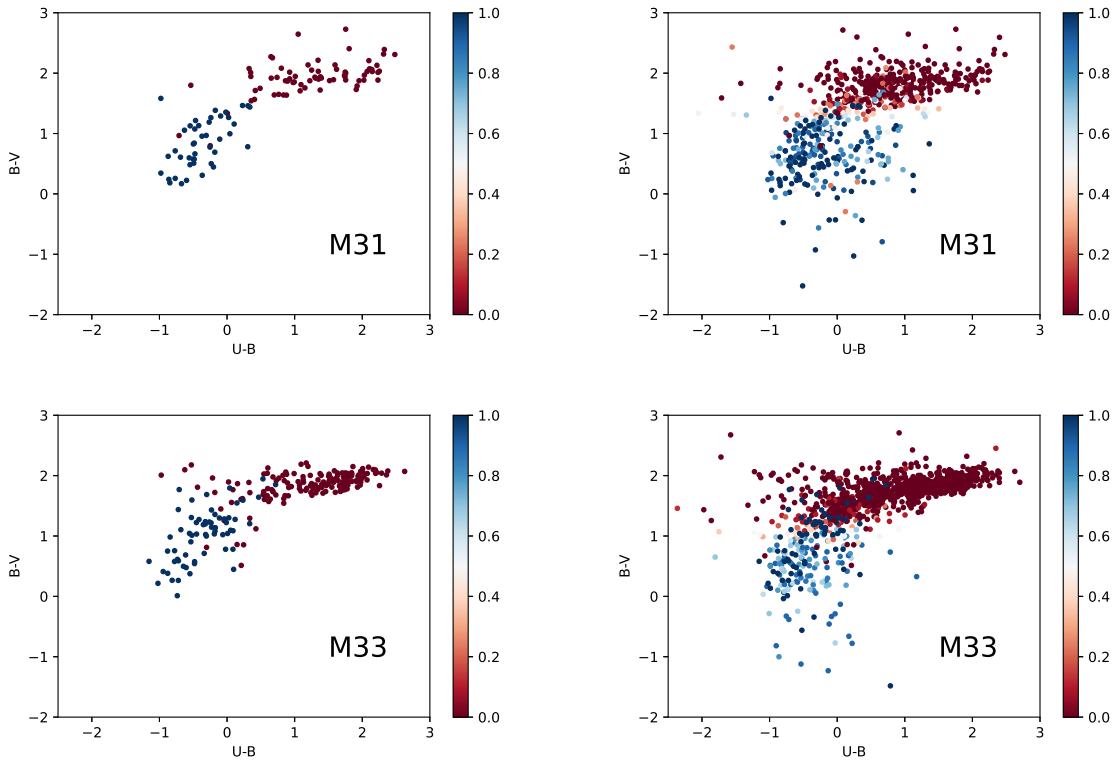

Figure 5.2 - Results of k-NN classification for M31 and M33. Figures on left show the locations in $U-B$ vs. $B-V$ color space of the spectroscopically confirmed RSG+B binaries and single stars in M31 (top) and M33 (bottom). Figures on the right show the k-NN classified RSGs as colored by their probability of binarity with bluer colors representing a higher probability of having a B-type binary companion and redder colors representing a higher probability of being a single RSG. As expected, RSG+B binaries have lower $U-B$ colors coming from the B-type star. Note the surplus of M31 RSGs in the color regime where both $U-B$ and $B-V$ is between 0 and 1 (top, right), and lack of such stars in the remaining three plots. As discussed here and in Massey et al. (2021), we believe these stars to be more highly reddened based on their location and thus their colors to be anomalous.

Thus, it is acceptable for the survey to be incomplete in some respects as long as it is incomplete equally for both the single and the binary RSGs. This is why, for example, I've made a cut in luminosity at $\log L/L_{\odot} \geq 4.2$. While, as detailed in Massey et al. (2021), RSGs with luminosities below this limit have been detected and spectroscopically confirmed, a *complete sample* for lower luminosity RSGs is not known due primarily to crowding and reddening. Another example deals with the cuts in ρ for both M31 and M33. As discussed earlier, I removed the inner bulge of M31 ($\rho < 0.1$) from the sample set due to crowding. While I was able to identify RSGs within M31's bulge, it was increasingly difficult to match them to their LGGS counterparts. However, I do not expect crowding to change the binary fraction of RSGs because it should equally effect both the binary and single stars.

The more serious concern is that the survey isn't sensitive to the faintest OB-type companions. When searching for RSG+OB binaries in the LMC, we were able to simply increase the exposure times in real time in order to achieve the S/N needed ($\sim$ 100 per 2Å at 4000Å as discussed in Chapter 2) to confidently rule out the presence of a faint OB-type companion. However, the Hectospec data taken in M31 and M33 were obtained in "queue" mode and exposure times could not be adjusted in real time. Additionally, while Hectospec's multi-fiber capabilities make it an ideal instrument for obtaining spectra of hundreds of stars at a time, it comes at the price of throughput, particularly in the blue where the upper Balmer lines reside. Finally, Hectospec has a spectral resolution of 5Å which is not small enough to detect the weakest lined B companions. Thus, the average S/N per 5Å spectral resolution element at 4000Å was $\sim$25 with a few spectra as low as 10 (though many as high as 40).

To determine the type of B companion that could still be hiding in the spectrum of our visually single RSGs, I turned back to the modeling work discussed in Chapter 2. We created a large set of synthetic spectra of RSG+B binaries by combining BSTAR06 (Lanz & Hubeny, 2007) models with MARCS RSG models (Plez et al., 1992) at various temperature and luminosity regimes. I took these models and degraded the resulting synthetic spectra to a S/N of 25 per Hectospec spectral resolution element. I then looked through the results to determine which spectra appeared to be single even though a binary companion was present.

I was relieved to find that all of the B-type giant and supergiants companions would still be detectable along with a sizable number of B dwarfs. The limiting spectral type was a B3 V with a temperature of 20,000K. With a S/N of 25, we cannot detect RSG+B star binaries where the B-type companion is fainter than a B3 V. However, as I discuss later on in Chapter 5.3.4, it is possible to quantify this completeness limit and take it into account when determining the errors.

We have a similar issue when it comes to the HST PHAT/PHATTER data in that the far-UV F275W photometry does not go deep enough to detect the faintest B dwarfs. This means that the k-NN algorithm might assign a lower probability of binarity to a RSG than it should. To investigate the extent of this issue, I considered two aspects. First, unlike with the GALEX photometry in the LMC where we only had one UV datapoint, the HST photometry provided photometric coverage across a wide wavelength range with two measurements in the UV, two in the Visible and two in the NIR. Thus, even if the bluest filter could not detect the presence of the faintest B dwarfs, the blue excess would still be detectable in the other UV filter (F336W) and the two Visible filters. Furthermore, I found that, given the limiting magnitude of the PHAT and PHATTER surveys in the F275W filter of 25th magnitude (Dalcanton et al., 2012), the surveys are sensitive down to a B5 V in either M31 or M33, or a B-type V with a temperature of 15,400K (Cox, 2000). However, after doing the same calculation for the F336W filter, even the faintest B dwarfs would be detectable with the M31 and M33 PHAT/PHATTER datasets. Thus, this does not add any completeness issues to the survey.

5.3 The Overall Binary Fraction

While the observations and surveys discussed above can provide an observed binary fraction, there are several observational biases that must be considered before a final binary fraction can be calculated for M31 and M33. The first set deals with biases present within the observations such as eclipsing binaries and line-of-sight pairings, while the second deals with the RSG binaries that the observations would not have been able to detect. To determine

Table 5.3. Binary Fraction

$\log(O/H)+12^*$	BPASS (Z)	Galaxy Region	RSG+OB (%)	eclipsing (%)	line-of-sight (%)	RSGs+CC (%)	Total (%)
8.29	0.004	M33 (outer)	$7.9^{+10.8}_{-1.7}$	1.84 ± 0.01	1.6 ± 0.8	4.73 ± 0.01	$15.9^{+12.4}_{-1.9}$
8.41	0.006	M33 (middle)	$15.2^{+6.1}_{-5.4}$	1.84 ± 0.01	1.6 ± 0.8	4.73 ± 0.01	$26.9^{+8.9}_{-5.5}$
8.72	0.008	M33 (inner)	$27.6^{+7.8}_{-7.3}$	1.84 ± 0.01	1.6 ± 0.8	4.73 ± 0.01	$41.2^{+12.0}_{-7.3}$
8.93	0.014	M31 (all)	$20.4^{+6.8}_{-6.3}$	1.84 ± 0.01	1.2 ± 0.6	4.73 ± 0.01	$32.7^{+10.1}_{-6.3}$
8.93	0.014	M31 (lightly reddened)	$22.5^{+5.2}_{-5.0}$	1.84 ± 0.01	1.2 ± 0.6	4.73 ± 0.01	$33.5^{+8.6}_{-5.0}$

*M31 oxygen abundance from Sanders et al. 2012; M33 oxygen abundances from Magrini et al. 2007

both the percentage of eclipsing binaries, and companions the survey was not sensitive to, I relied on the BPASS models v2.2.1 from Eldridge et al. (2017); Stanway & Eldridge (2018). BPASS uses (among other initial conditions) the recent results of Moe & Di Stefano (2017) to create a population of single and binary stars in various metallicity environments. At a given time step, it provides values for periods, mass-ratios, separations (of binaries) and a variety of physical properties such as temperature and luminosity (for all stars). For the work done here, I was able to select the BPASS models with temperature and luminosity criteria matching the RSG cutoffs used here and described by Massey et al. (2021) to form the M31 and M33 RSG catalog. I additionally used metallicity values appropriate to the various environments of M31 and M33. Final values for the binary fraction in the various environments of M31 and M33 are given in Table 5.3.

5.3.1 Eclipsing Binaries

The majority of the observed binary fraction estimate is based on single epoch photometry from LGGS or PHAT/PHATTER and thus it is important to consider the scenario when the OB companion is behind the RSG at the time of observation. An example system is VV Cep, the Galactic RSG+B star binary system with a 20.3 year orbit and 18 month secondary eclipse (Bauer & Bennett, 2000). A similar system in M31 or M33 would not be identified as a potential binary during secondary eclipse because the excess flux from the OB

companion would be masked. To determine the likelihood of such a positioning, I turned to BPASS. By examining the BPASS models at a single point in time (corresponding to single-epoch photometry), I used a script kindly provided by J.J. Eldridge to determine the maximum angle of inclination for eclipses based on the RSG's radius and separation and then further determined the likelihood of each system being in eclipse. Overall, the percentage of RSG+OB binaries in eclipse at any given time is $1.84 \pm 0.01\%$, and is given in Table 5.3.

5.3.2 Line-of-Sight Pairings

Line-of-sight pairings are increasingly a concern as we move to RSGs in more distant galaxies like M31 and M33. Such pairings exist when the RSG and OB star are both members of M31 or M33 but are not gravitationally bound and instead just exist on the same sight path. To estimate the number of spectroscopically confirmed RSG+B binaries that might be line-of-sight pairings instead of gravitationally bound companions, I used a Monte Carlo simulation much like the one discussed in Chapter 4 to determine the likelihood of line-of-sight pairings for the RSGs based on their local OB star densities. Overall, for each of the spectroscopically confirmed RSG+B star binaries, I used B and V photometry and coordinate information from the LGGS to determine the positions of OB stars that fell within a $5'$ radius of the binary. I then randomly placed the binary within this region and checked to see if it fell within 0.75" (the radius of a MMT Hectospec fiber) within one of the OB stars. If it did, it was flagged as a line-of-sight pairing. OB stars were selected based on having $(B-V) < 0.0$ corresponding to an A0V, V brighter than 22nd, and average $E(B-V)$ reddenings of M31 and M33 of 0.13 and 0.12, respectively (Massey et al., 2007a). Overall, I found a $1.2 \pm 0.6\%$ chance of a line-of-sight pairing in M31 and a $1.6 \pm 0.8\%$ chance in M33.

Adding in photometry will only make the situation improve. A large fraction of the RSGs (both single and binary) have HST photometry from PHAT / PHATTER (see Table 5.2) which provided images (and photometric catalogs) with milli-arcsecond resolution (see Dalcanton et al. 2012 and Williams et al. 2021 for details). Thus, the k-NN classification will not produce errors as high as those produced by spectroscopic confirmation. However, I still

adopt the higher line-of-sight error estimates for the entire sample as a "worst-case" scenario. Line-of-sight pairings are additionally discussed further in Chapter 5.3.2.

5.3.3 RSGs and non-OB Companions

The observational study outlined here is sensitive to RSGs with OB companions, which stellar evolution dictates are the most likely companions. However, it is important to consider the likelihood of other types of companions to RSGs. For stellar companions, this list includes evolved massive stars such as YSGs, other RSGs, and WRs. For non-stellar companions, this includes compact companions such as neutron stars and black holes. As a reminder, lower mass stellar companions are not on this list because they would still be in the pre-main sequence phase.

As discussed extensively in Chapter 4, we do not expect to find a large number of RSG+RSG or RSG+YSG systems simply due to the short lifetimes of stars in these phases (the YSG phase, for example, only lasts tens of thousands of years). However, it is important to point out that the study described here would not be sensitive to such systems. Such a pairing might be observable through high resolution spectroscopy of the Ca II triplet line and searching for changes over time but this is outside the scope of the current work. Extensive efforts have recently been done by Patrick et al. (2019) and Dorda & Patrick (2021) searching for RSG binaries using radial velocity variations (and is discussed more below) and it is possible that this path will allow for the identification of any RSG+RSG/YSG binary systems through further analysis and orbit determinations.

Turning to more evolved massive stars, there cannot be a large population of missing RSG+WR systems. The WR content of both M31 and M33 is thought to be complete (Neugent et al., 2012a; Neugent & Massey, 2011) and the optical spectra of the known WRs have been examined for the presence of TiO bands indicative of a RSG companion. One star, J004453.06+412601.7, was originally classified by Neugent et al. (2012a) as a WN+TiO, but PHAT imaging clearly shows the TiO as coming from an object other than the WR. Thus, there are no known RSG+WR systems expected to be discovered in M31 or M33.

While RSG stellar companions should primarily be OB stars, we do expect a small fraction of RSGs to have compact companions that are not detectable using the observational method described here. Such compact companion systems occur when the RSG is the initially less massive star in the system and the more massive star explodes as a supernova and leaves behind either a neutron star or black hole as the companion to the RSG. The first spectroscopic confirmation of such a system was recently presented by Hinkle et al. (2020) for Galactic X-ray binary 4U 1954+31. They found that the system contains a high mass M-type supergiant paired with a neutron star and present a promising first detection of RSGs with compact companions. Additional, albeit circumspect, evidence of possible RSGs + compact companions was presented by Dorda & Patrick (2021) and their radial velocity study of RSGs in the LMC. Three of the LMC RSGs they classified as binaries were additionally spectroscopically observed by us (and discussed in Chapter 4) and show no evidence of an OB companion. It is thus possible these RSGs could be the first extragalactic detection of RSGs with compact companions. However, either further spectroscopy (both for radial velocities and companion detection) or a targeted x-ray campaign is necessary. BPASS v2.2.1 gives the fraction of RSGs with compact companions as $4.73 \pm 0.01\%$, as is shown in Table 5.3 as RSG+CC (compact companion).

5.3.4 RSGs and Faint B-type Companions

As discussed in Chapter 5.2.4, the MMT spectra were not sensitive to B-type companions fainter than B3Vs because of S/N limitations. However, with BPASS v2.2.1, it is possible to determine the percent of RSG binaries with B-type companion less massive than a B3V (or $T_{\rm eff} < 20000$K). Using the same set of BPASS models described above, I was able to determine that at a given metallicity, 10% of RSG binaries will contain a B-type companion that is fainter than a B3V. Thus, for any given binary fraction, the errors in the direction of *increasing* the binary fraction have been made larger to account for potentially missing detected systems. The value has been included in the final binary fraction calculation included in Table 5.3. However, as with the line-of-sight pairings, this error only applies to the spec-

troscopically confirmed RSG binaries and not those classified through the k-NN photometric approach. Thus, this error is again taken to be a worst-case approximation.

5.3.5 Final Binary Fraction

To calculate a final binary fraction, the observed RSG+OB binary fraction calculated using the k-NN approach must be combined with corrections for the observational biases of our inability to detect companions fainter than B3Vs, eclipsing binaries at a single epoch, line-of-sight pairings, as well as RSGs with compact companions. Additionally, as alluded to in Chapter 5.1.1, calculating the overall RSG content of M31 was hampered by heavy reddening and thus I've calculated the binary fraction for all of M31 as well as just the less-reddened regions (as defined by Massey et al. 2021). The numerical results are presented as a function of metallicity in Table 5.3 with a further discussion in the next Chapter. Overall, as the metallicity decreases, so does the binary fraction. In the inner portion of M33, where the metallicity is the highest (around solar), the binary fraction is $41.2^{+12.0}_{-7.3}$%, while in the lower metallicity outer portion of M33, the binary fraction is the lowest at $15.9^{+12.4}_{-1.9}$%. In M31, where there is no metallicity gradient, the binary fraction remains constant at $33.5^{+8.6}_{-5.0}$% in the lightly reddened regions. Errors on the observed RSG+OB binary fraction using the k-NN approach were calculated assuming the most extreme scenarios following the given accuracy rates as given in Table 5.2. Errors for BPASS provided numbers were calculated using basic Poisson statistics. Final errors were added in quadrature after taking into account the 10% increase in the binary fraction caused by detection limits on faint B companions.

Chapter 6

RSG BINARY FRACTION AS A FUNCTION OF METALLICITY

Examining the binary fraction of RSGs in M31 and M33 makes it possible to place constraints on any metallicity dependence. While the exact values for the metallicities of M31 and M33 vary based on measurement method (discussed further in Chapter 6.3), all studies point to M33 having a clear decrease in metallicity with increasing ρ and M31 having little spatial metallicity dependence. Here I show that the RSG+OB binary fraction *also* decreases with ρ in M33 but stays relatively constant throughout all of M31, suggesting a metallicity dependence on the RSG+OB binary fraction.

6.1 A Clear Trend

As seen in Table 5.3, there is a clear trend in both the observed RSG+OB binary fraction (as computed using the k-NN approach) as well as in the final binary fraction with increasing metallicity in M33. As the metallicity approximately doubles between the outer and inner region of M33, so does the RSG+OB binary fraction. Figure 6.1 shows the change in the RSG+OB binary fraction as a function of ρ for both M31 and M33. For both galaxies, the binary fraction is plotted as a moving box-car average with each point on the plot representing the average binary fraction over the closest 400 stars in ρ value. The moving average shifts by 25 stars for each new datapoint. So, taking M33 as an example, the innermost point at $\rho \sim 0.1$ and RSG+OB binary fraction at $\sim 33\%$ represents the average binary fraction of the innermost 400 stars. The next point to the right represents the average RSG+OB binary fraction of the 25th - 425th innermost stars (at a $\rho \sim 0.15$ and binary fraction of $\sim 32\%$). Because each point represents 400 stars, the ρ value on the x-axis stops short of the largest

ρ values in the dataset (in M31, ρ stops at 0.75, but the stars extended to $\rho = 1$; in M33, ρ stops at ~ 0.65 but the stars extend out to $\rho = 0.75$). Both positive and negative errors are then shown by the shaded region.

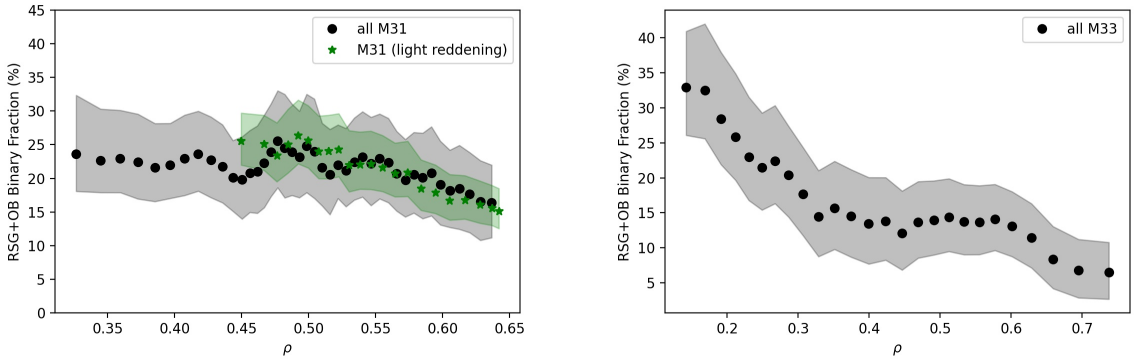

Figure 6.1 - RSG+OB Binary Fraction as a function of ρ (Galactocentric distance) in M31 (left) and M33 (right). The RSG+OB Binary Fraction was measured using the k-NN algorithm, as discussed in the text. Values were calculated using a moving box-car average where each point represents the average binary fraction of the closest 400 stars in ρ value. Each new point is a shift of 25 stars. The strong decrease in the RSG+OB binary fraction with respect to increasing ρ in M33 is due to the galaxy's strong metallicity gradient. Such a gradient does not exist in M31 and thus the binary fraction is relatively constant with increasing ρ. © AAS. Reproduced with permission from Neugent (2021).

Using this visualization method in M33, the striking metallicity dependence on the RSG+OB binary fraction becomes clear. In the innermost region of M33, where the metallicity is close to solar, the RSG+OB binary fraction is $\sim$ 33%. In the outermost region where the metallicity is 0.25× solar, the RSG+OB binary fraction has decreased to less than 10%. Conversely, in M31, where there is no strong metallicity gradient, the RSG+OB binary fraction stays relatively constant at around 23%.

Also interesting is the presence of a small (1%) bump in M31's RSG+OB binary fraction at $\rho \sim 0.5$. This traces the locations of the well-known star-formation ring where most of the

HI, OB associations, and Hα emission are located (see, e.g., Roberts 1966; van den Bergh 2000; Devereux et al. 1994, respectively). One criticism of the photometric/spectroscopic method I've employed is that it might be overly sensitive to line-of-sight pairings (Dorda & Patrick, 2021). As discussed in Chapter 5.3.2, I believe these introduce a $\sim 1\%$ error, which this plot supports. If a significant fraction of the RSG+OB binaries I've detected were actually line-of-sight pairings, the RSG+OB binary fraction would be *much higher* in the OB forming regions (such as at $\rho \sim 0.5$ in M31) where the majority of the OB stars exist. The RSG+OB binary fraction would then be much lower in the regions further away from any OB associations. However, as shown in Figure 6.1, this is simply not the case. The RSG+OB binary fraction in M31 is relatively constant and any small increase at $\rho \sim 0.5$ is within the errors. Thus, this lends further credence to the idea that line-of-sight pairings are not playing a large role in the detection statistics. Additionally, line-of-sight pairings due to crowding are also ruled out. If crowding were a significant issue, there would be a clear trend in the RSG+OB binary fraction in M31 with the more crowded inner regions having a higher binary fraction. While we see this general trend in M33, we can be confident it is not due to crowding both since M33 is much less crowded than M31, and such a trend is not present in the M31 data.

As discussed extensively in Massey et al. (2021), the determination of a *complete* RSG sample in M31 is partially hampered by reddening within M31. Since we observe the galaxy at a significant tilt instead of face-on, some stars are redder and fainter due to us looking through extra dust. Massey et al. (2021) attempted to trace the regions of increased reddening by looking for RSGs with matches in the LGGS. If RSGs have matches in the LGGS, this means they were detected in *B, V,* and *R*, suggesting that they are lightly reddened. RSGs without matches in the LGGS were not detected in B due to the large amount of dust obscuring our view and making them non-detections in the B filter. Figure 9 in Massey et al. (2021) shows spatially the RSGs with NIR colors that also have matches in the LGGS and the resulting image matches up nicely with extinction maps of M31, notably Draine et al. (2014). Using only the RSGs in less-reddened regions (the bright regions in Figure 9 in Massey et al. 2021),

I calculated a revised RSG+OB binary fraction. While the overall percentage doesn't change much (20.4% for all of M31 and 22.5% for the lightly reddened regions), the uncertainties decrease by a percentage on each side due to the increased number of RSGs with LGGS colors.

6.2 Possible Explanations

The results shown in Figure 6.1 and Table 5.3 are quite striking – there is a clear dependence of the RSG+OB binary fraction on metallicity, with higher metallicities corresponding to an increase in the binary fraction. I can first try to explain this trend by considering how the metallicity of an environment affects stellar evolution and the physical properties of RSGs. As discussed in the introduction, the metallicity of an environment has a lasting impact on the evolution of massive stars. Elias et al. (1985) first noted that as the metallicity increases, so does the average temperature of the RSGs. This was further investigated by Levesque et al. (2005) by determining the physical properties of a sample of RSGs in the Magellanic Clouds and confirming that as the metallicity increases, so does the average effective temperature. Their Figure 10 shows the evolutionary tracks as a function of metallicity and the resulting shift of the Hayashi limit. As the metallicity decreases, the Hayashi limit shifts to cooler temperatures, leading to a decrease not just in the overall effective temperatures of the RSGs, but also a decrease in their maximum sustainable radii. Is this decrease in radius with metallicity significant enough that it could change the binary fraction?

As the average RSG radii increases with increasing metallicity, one might naively expect the number of RSG+OB binaries to decrease since more of them will have merged due to the increasing size of the RSG. However, this goes in the *opposite* direction of what we observe. To answer this question a bit more carefully, I took a look at the predications given by the BPASS v2.2.1 models. Overall, BPASS does not predict any significant change in the RSG+OB binary fraction as a function of metallicity. Instead, much like the value presented for BPASS in Chapter 4, it provides a RSG+OB binary fraction of $\sim 34 - 35\%$ regardless of metallicity. Since BPASS *does* take into account the average change in RSG as a function

of radius, but still does not predict a changing RSG+OB binary fraction, this leads me to believe the shift in Hayashi limit (and resulting change in physical properties) is not the main reason for the metallicity dependence.

Instead, I believe the answer lies in the formation of these stars. Little work has been done on the metallicity dependence of large populations of un-evolved OB stars as a function of metallicity. While the overall binary fraction of these stars is thought to be quite high (Sana et al., 2012, 2013), there have been no large-scale studies to show whether their binary fraction is metallicity dependent. Given that BPASS assumes a constant OB binary fraction as a function of metallicity, it then directly follows that a metallicity trend would not be revealed in the results. While there is still much work left to be done, I believe this points to a strong suggestion that the change in the RSG binary fraction with metallicity is not due to the physical properties of the RSGs changing, but rather due to metallicity changes with their parent population of OB stars either in terms of their binary fraction or the orbital separations between such systems.

6.3 Comments on the Metallicities of M31 and M33

So far, I've discussed the metallicity gradient of M33 and the relatively high metallicity of M31 but I only briefly mentioned actual values in the introduction and Table 5.3. This is because the precise values are still open to debate and change pretty significantly based on measurement technique. There are two main methods of measuring the oxygen abundance in H II regions. The first is the "direct" method where the the electron temperature is measured, usually from the auroral [O III] λ4363 line while the second is the "strong-lined" method (or "R_{23}") which uses the ratio of the sum of [O II] and [O III] over Hβ. In Table 5.3, I've given the values using the R_{23} method from Sanders et al. (2012) and Magrini et al. (2007) for M31 and M33, respectively. However, care should be taken when considering these *exact* values as opposed to the values in a relative sense.

Based on the clear trend of decreasing RSG+OB binary fraction with ρ in M33 and lack of any such trend in M31, I feel confident that this is a metallicity effect. While the exact values

for the metallicity of M31 and M33 might be under some debate, there is general agreement that M33 has a strong gradient with ρ while M31 does not (Esteban et al., 2020; Toribio San Cipriano et al., 2016). Additionally, the overall LMC RSG binary fraction of $19.5^{+7.6}_{-6.7}$% discussed in Chapter 4 (with a metallicity somewhere between the inner and middle regions of M33) fits nicely in with the results shown in Table 5.3. Somewhat surprisingly, the M31 RSG binary fraction is somewhat lower than expected if all of M31 has a higher metallicity than that of the inner region of M33. But, some measurement techniques suggest that the inner regions of M33 could be higher than M31 (Zaritsky et al., 1994), and thus further studies are needed. Overall, while the exact values of the metallicities for these galaxies are unknown, the trend is clear.

6.4 Summary

These are the first results of the RSG binary fraction as a function of metallicity using the RSG content of M31 and M33. In M33, the overall RSG binary fraction appears to range between $41.2^{+12.0}_{-7.3}$% in the inner (higher metallicity) regions of M33 to $15.9^{+12.4}_{-1.9}$% in the lower metallicity outer regions. In M31 where there is no metallicity gradient, the overall RSG binary fraction of the lightly reddened regions is $33.5^{+8.6}_{-5.0}$%. These values were determined by first using the recent work of Massey et al. (2021) to determine a complete sample of RSGs in M31 and M33 down to a limiting $\log L/L_{\odot} \geq 4.2$ and then spectroscopically confirming candidate RSG+OB binaries that had been selected based on their excess blue flux. Using archival LGGS and HST photometry, I then using a k-NN approach to estimate the binary fraction of RSG+OBs using the spectroscopically confirmed single and binary RSGs as a training set. The binary fraction was then corrected for observational biases (such as eclipsing systems and line-of-sight pairings) and systems the detection method may have missed (such as RSGs with companions that were either fainter than B3Vs or compact companions). The overall binary fractions for M31 and M33 are shown in Table 5.3 and present a clear decreasing trend with metallicity. I believe this trend is due to a dependence on the binary fraction of un-evolved OB stars with metallicity, but this is still an active area of research

and one that will be difficult to tackle without a targeted spectroscopic survey.

These results fit in well with previous studies of the RSG binary fraction in other environments such as in the LMC ($\log(O/H) + 12 = 8.4$, similar to the middle region of M33; Russell & Dopita 1990) where we found a value of $19.5^{+7.6}_{-6.7}\%$ using a similar method to the one described here. Additionally, recent radial velocity studies done by Patrick et al. (2019) and Dorda & Patrick (2021) placed an upper limit of the RSG binary fraction at 30% in the LMC's 30 Doradus and a lower limit of $15 \pm 3\%$ in both Magellanic Clouds. While such studies are more sensitive to shorter period systems, they allow for the direct detection of RSGs with compact companions. Hopefully a combination of the photometric method described here as well as the radial velocity method taken by Patrick et al. (2019) and Dorda & Patrick (2021) will lead to an overall better understanding of the binary fraction of RSGs.

Chapter 7

TWO COMPLEMENTARY PROJECTS: MASS-LOSS RATES AND MERGERS

While the majority of this thesis focuses on the RSG binary fraction as a function of metallicity, I additionally worked on two complementary RSG projects. The first, which focused on measuring the mass-loss rates of RSGs in M31, was completed and published in Neugent et al. (2020b). The second involves searching for merged RSGs and has grown to a larger-than-anticipated scale and will thus encompass a large portion of my postdoctoral work. However, the motivation for the project is discussed here.

7.1 Project #1: Measuring the Mass-Loss Rates of M31 RSGs

As discussed in the Introduction, the existence of a companion can dramatically alter the evolution of a massive star. For one, all massive stars are known to experience significant mass-loss throughout their lifetimes. However, being in an interacting binary system can enhance these mass-loss rates since the companion can additionally strip the primary through Roche-lobe overflow. Up until now, it has not been possible to investigate differences in mass-loss rates between binary and single RSGs because a large enough population of binary RSGs was not known. However, by determining a population of binary RSGs in the Local Group galaxies, the groundwork has now been done. Preliminary work on determining the mass-loss rates of RSGs was done by Neugent et al. (2020b) for a sample of both binary and single RSGs in M31, as described in the remainder of this section. Future work will involve a similar study across both differing metallicity regimes and comparing binary and single RSGs.

7.2 Mass-Loss in Red Supergiants

The evolution and final fate of RSGs is heavily influenced by their mass-loss rates which are quite large (as high as $10^{-4} M_{\odot}$ yr^{-1} compared to the Sun's mass-loss rate of $10^{-14} M_{\odot}$ yr^{-1}) and episodic. Ekström et al. (2012) significantly revised the mass-loss prescription for RSGs for the Geneva evolutionary models, based upon the newer measurements of Sylvester et al. (1998) and van Loon et al. (1999), as discussed in Crowther (2001). The differences with the older de Jager et al. (1988) relation are small, except for the highest luminosity RSGs. They found that for RSGs above some certain mass limit of $15 M_{\odot}$, the outer layers of the star would exceed the Eddington luminosity, and in this situation increased the mass-loss rate by an additional factor of 3 for the duration of the event. The net result of these changes is that the time-averaged mass-loss rate of a $20 M_{\odot}$ RSG at solar metallicity was a factor of 10 greater than that obtained by the previously adopted de Jager et al. (1988) relationship traditionally used in the older evolutionary models (see, e.g., Schaller et al. 1992). The implications of this change were many and varied, and include the result that the mass limit for stars to becoming Wolf-Rayets (WRs) is decreased and more stars go through a second YSG phase after becoming RSGs rather than exploding directly as supernova. As suggested by Ekström et al. (2012), this later difference could explain the so-called "RSG problem," the lack of observed high-luminosity RSG progenitors to Type II-P SNe (Smartt et al., 2009). The older Geneva evolutionary models had done a poor job in predicting the relative number of YSGs as a function of luminosities (Drout et al., 2009; Neugent et al., 2010), but after this revision to the RSG mass-loss rates (as well as many other improvements), the newer models reproduced the observations very well (Drout et al., 2012; Neugent et al., 2012b). However, until now there has been no other observational tests of the revised mass-loss rate prescription during the RSG phase.

This revision in the RSG mass-loss rate was profound for the higher mass RSGs, but the direct measurements of the mass-loss rates do not preclude even larger changes (Meynet et al., 2015), and there is no direct constraint based upon stellar atmosphere modeling. Because

these stars have such low surface gravities ($\log g \sim 0$) and escape velocities (< 100 km s^{-1}), Stan Owocki (private communication, 2006) has argued that it's a little like walking across the room with a glass of water filled to the brim: even a small jiggle can lead to dramatic increases in the mass loss for a RSG. Mass-loss rates have only been directly measured for around 50 stars and the results are highly inconsistent (Mauron & Josselin, 2011; van Loon et al., 2005; Beasor & Davies, 2016) (see Meynet et al. 2015, Figure 1 for a comparison to the Geneva model mass-loss rate prescriptions). In addition, the mass-loss rates themselves are uncertain: to measure the mass-loss rate of individual RSGs, all we can do is measure the dust production rate and then infer a total mass-loss rate by multiplying by an uncertain large number (100-500$\times$) depending on what we assume for the gas-to-dust ratio. And even this idea of a "standard" mass-loss rate is questionable. For one, what we measure today might not relate to the time-averaged mass-loss rate. For instance, Smith et al. (2001) demonstrated that VY CMa, an extremely luminous RSG, underwent a period of enhanced mass loss 1000 years ago (Decin et al., 2006). It is unknown how often these outbursts occur and what fraction of the measured mass-loss rates might be caused by an outburst. Meynet et al. (2015) and Georgy & Ekström (2015) have argued that the actual time-averaged mass-loss rates could be a factor of 10 or even 25 times higher than what is currently adopted.

Here we follow up on the suggestion of Meynet et al. (2015) and Georgy & Ekström (2015) of using the RSG luminosity function as an observational test of the time-averaged RSG mass-loss rates. As RSGs evolve and go through core helium fusion, their effective temperatures barely change but their luminosity increases as the helium core grows. Increased mass-loss rates (whether as single or binary stars) shorten the RSG lifetimes of these stars by removing their outer layers since as more mass is removed, the envelope to core ratio will change. Once the core represents a certain fraction of the star, the star will evolve back blue-ward. So, the more mass lost, the faster the blue-ward evolution will occur. The more luminous RSGs will lose more mass than the less luminous RSGs because mass-loss rates are luminosity-dependent. Thus, as mass-loss rates increase, the ratio between the number of higher luminosity RSGs to the number of lower luminosity RSGs will decrease. This is

shown in Figure 7.1. As the luminosity increases, the relative number of RSGs decrease in all the models, due to the decreasing number of higher mass progenitors (all assume a Salpeter IMF). For a given number of total stars, the Geneva high mass-loss models (10× and 20× models) predict far more low luminosity RSGs, and fewer high luminosity RSGs (Georgy et al., 2013; Ekström et al., 2012). The BPASS 2.2.1 binary and single-star models (Eldridge et al., 2017) predict a very similar luminosity function as the standard Geneva model, except at the higher luminosity end, where they predict significantly more stars[1]. The BPASS 2.2.1 models adopt the de Jager et al. (1988) prescription for mass-loss during the RSG phase, although of course the binary versions also include mass-loss driven by the companions (Eldridge et al., 2017; Stanway & Eldridge, 2018).

7.3 The Need for New Near-Infrared Data

Obtaining a useful luminosity function of RSGs has three requirements. First we must compute luminosities at the 0.05 dex level for a sample down to $\log L/L_{\odot} \sim 4.0$ in order to create a well-sampled histogram. Fainter than this runs the risk of contamination of faint red foreground stars as shown in Sec. 7.5.2. Requiring luminosities at a 0.05 dex precision level ruled out using RSGs in the Milky Way due to uncertain distances in the pre-*Gaia* era. Additionally even in the post-*Gaia* Data Release 2 (DR2) era, it is messy and uncertain to identify a volume-limited sample in the presence of large and variable reddenings. This luminosity requirement drove us to the near-infrared (NIR) rather than the optical, as detailed below. Secondly, as our goal is not only to obtain an observationally robust luminosity function, but to compare to current model predictions for mass-loss rates, we currently require stars that have metallicities of solar and above ($1 - 1.8Z_{\odot}$), ruling out using RSGs in the LMC or Small Magellanic Cloud (SMC) as the lower metallicity single-star Geneva Evolutionary grids do not produce high luminosity RSGs. Thirdly, we need a large enough sample (several hundred stars) so the luminosity function is not dominated by

[1]We are indebted to J.J. Eldridge for kindly computing the expected RSG luminosity distributions for us from her latest BPASS models.

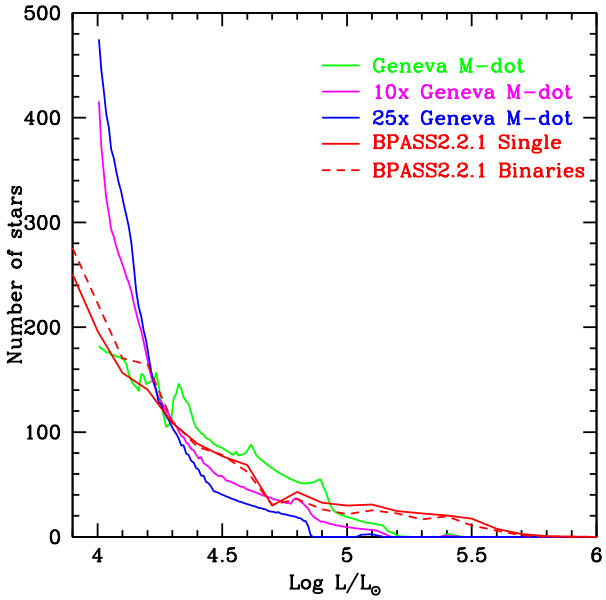

Figure 7.1 - The dependence of the RSG luminosity function on the assumed mass-loss rate. The theoretical predictions have all been scaled to a sample of 1000 RSGs with $\log L/L_{\odot} \geq 4.0$ and analyzed with 0.1 dex bins, similar to the sample we analyze here. The green line comes from the Geneva mass-loss prescriptions described in Ekström et al. (2012), which are in accord with more modern estimates of the observed rates as described in the text. The magenta and blue lines show the luminosity functions for enhancing this rate by a factor of 10 and 25, respectively. All of these Geneva predictions were computed using SYCLIST (Georgy et al., 2014a). We also include the luminosity functions (red) from the BPASS 2.2.1 models (Stanway & Eldridge, 2018) both for single stars (solid) and with binaries (dashed); we are grateful to J. J. Eldridge for providing these predictions. Although the effect of binaries is to reduce the number of RSGs by a factor of $\sim$2 for a given star-formation rate, it has almost no effect on the *shape* of the luminosity function. Note in particular the good agreement between the Geneva and BPASS 2.2.1 predictions.

stochastic, small-number statistics at the bright end. These three considerations lead us to M31's RSG population, as the galaxy is nearby with a well-determined distance (760 kpc, van den Bergh 2000 and references therein), low reddening ($A_V \sim 1.0$ mag for the RSGs, Massey et al. 2009; Massey & Evans 2016), and a suitable metallicity that is about 1.5× solar (Sanders et al., 2012).

The NIR is preferable to the optical for three main reasons. First, we are less sensitive to the reddening than in the optical; the extinction at K_s is only 12% of what it is at V ($A_K = 0.12 A_V$; see, e.g., Schlegel et al. 1998), meaning that uncertainties in the extinction have a much smaller effect on the derived luminosity[2]. Similarly, $J - K$ colors are less affected by reddening than are optical colors; while $E(B-V) = A_V/3.1$, $E(J-K) = A_V/5.8$ (Schlegel et al., 1998). This is particularly an issue for RSGs, as they suffer from circumstellar extinction due to their dust production. The typical OB star in M31 has A_V of 0.5 mag (Massey et al., 2007b), while the RSGs in our sample typically have an average A_V of 1.0 mag (Massey et al., 2009); we see a similar effect when we compare Galactic RSGs to OB stars in the same clusters; see Massey et al. (2005). (We will delve into the reddening issue more exactly in Sec. 7.6.)

Second, the bolometric corrections (BCs) at K are much less sensitive to the determination of effective temperatures than at V. The effective temperatures of RSGs are ∼3500-4100 K (Levesque et al., 2005); as a result, their flux F_λ peaks in the far red (7000-8000Å). Over this temperature range BC_V varies from −2.2 to −0.8 mag (i.e., by 1.4 mags), while BC_K varies from +2.9 to +2.5 (i.e., by 0.4 mag); see Levesque et al. (2005). At the same time, $(J-K)_0$ is quite sensitive to the effective temperature, changing from 1.20 (3500 K) to 0.86 (4100 K), a difference $\Delta(J-K)_0 = 0.34$, according to the MARCS models used by Massey et al. (2009). For comparison, $(V-R)_0$ changes by almost the same amount, from 1.09 to 0.76 ($\Delta(V-R)_0 = 0.33$), although it is more affected by reddening. Thus for the same photometric precision, the uncertainty in the BC will be 3.5× smaller using NIR colors than

[2]For convenience, we have included the various relations we've adopted or derived throughout this Chapter in Table 7.4.

in the optical, even in the absence of reddening, due to the smaller change in the BC over a similar range in color and temperature.

The third factor driving us to the NIR is that RSGs are photometrically more variable at V than at K. Levesque et al. (2006) found that the typical V-band variability during a year was 0.9 mag, while K-band variability amongst RSGs is $\sim$0.15 mag (Josselin et al., 2000; Massey et al., 2009). This irregular variability is due to several causes, including variable dust production (producing increased circumstellar extinction), and the existence of large convective zones on the surface of these stars that have high contrast between the hotter and cooler spots in V than at K.

Massey & Evans (2016) use the Two Micron All Sky Survey (2MASS) photometry to construct the H-R diagram shown in Figure 7.2. As above, accurate J-K colors and K-band magnitudes are needed to determine good bolometric luminosities. The 2MASS photometry is complete (at 10σ) only to $K = 15.0$ for the 6x catalog (Cutri et al., 2012), which included coverage of M31. We indicate this completeness limit by the black band. This completeness is purely photometric, and ignores issues of crowding, which causes increasing losses at fainter magnitudes in crowded fields such as found in M31; this is especially true given the 2" resolution of 2MASS. Thus we are currently limited to $\log L/L_\odot \sim 4.8$ by the lack of good NIR photometry, while from Figure 7.2 we see we really would like to go down to $\log L/L_\odot$ of $\sim$4.0 to include $\sim 9 M_\odot$, say[3] . This corresponds to $K \sim$16.2-16.7 for a cool (3500 K) and warm (4100 K) RSG, respectively.

Given the reasons detailed above, we set out to obtain new near-IR photometry of RSGs within M31. It is important to note that the NIR M31 photometry described in this Chapter predates the work mentioned previously in Chapters 5 and 6 done by Massey et al. (2021). It is described chronologically out of order to keep the main emphasis on describing the RSG binaries.

---

[3]There is some mismatch between the tracks and the locations of the points in Figure 7.2; in our analysis here we will use an improved relation between temperature and color, and also treat the reddening in a better manner than did Massey & Evans (2016).

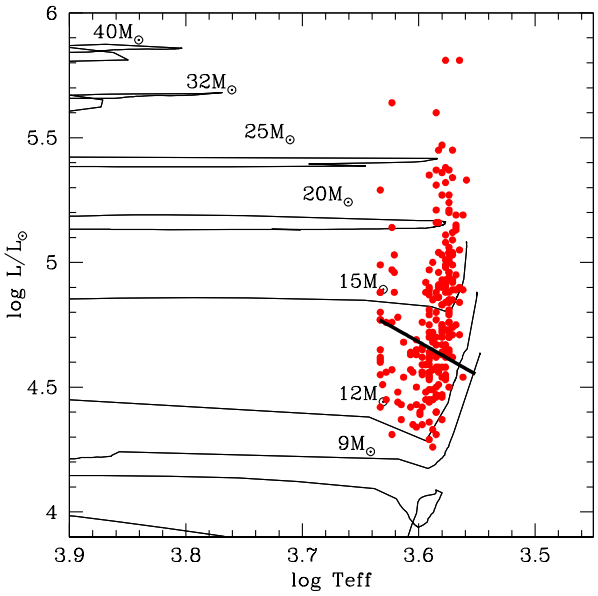

Figure 7.2 - H-R Diagram of red supergiants in M31 based on 2MASS data. The evolutionary tracks of Ekström et al. (2012) for $z = 0.014$ are shown along with the (initial) masses. The black line near $\log L/L_{\odot} \sim 4.8$ denotes the completeness limit of the 2MASS K-band photometry. Adapted from Massey & Evans (2016). © AAS. Reproduced with permission from Neugent et al. (2020b).

7.4 Observations and Reductions

All the J and K photometry comes from new images taken with the Wide Field Camera (WFCAM) on the 3.8-meter United Kingdom Infrared Telescope (UKIRT) located on Mauna Kea, Hawai'i. The data were obtained as part of the UKIRT Service Program (Proposal U/17B/UA03); UKIRT is owned by the University of Hawai'i (UH) and operated by the UH Institute for Astronomy; operations are enabled through the cooperation of the East Asian Observatory. Observing time was granted through the Steward Observatory Telescope Allocation Committee.

We selected two M31 fields and one nearby "control" field[4] as shown in Figure 7.3 and Table 7.1. The scientific requirement was to achieve an uncertainty of 0.05 dex in $\log L$, or roughly 0.1 mag, at $\log L/L_{\odot}$~4.0. We aimed for a S/N of 30 at K=17.0 and J=18.0, about 0.5 mag deeper than needed to assure completeness. This gives us an error of <0.05 mag in $J-K$ for our faintest stars, leading to an uncertainty of <100 K in the effective temperature

[4]As we discuss in Chapter 7.5.1, our control field was unfortunately a tad *too* "nearby."

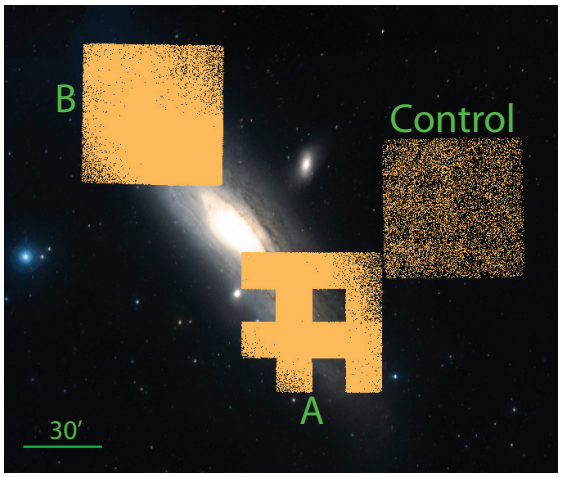

Figure 7.3 - Location of our fields in M31. The three UKIRT fields (A, B, and control) are shown (see Table 7.1) by indicating all of the stars with photometry as yellow points. The non-square shape of field A is due to the planned dithers not being executed properly. © AAS. Reproduced with permission from Neugent et al. (2020b).

Table 7.1. UKIRT Imaging

Field	α_{2000}	δ_{2000}	UT Date of Obs.		Final Area (deg^2)	# stars[a]
			Visit 1	Visit 2		
A	0:40:12	+40:42:00	2017 Dec 08	2017 Dec 11	0.54	116,498
B	0:45:36	+42:00:00	2017 Dec 30	2018 Jan 06	0.72	132,623
Control	0:35:24	+41:24:00	2017 Dec 12	2017 Dec 28	0.72	11,057

[a]Includes some saturated stars that were removed in the analysis.

scale (similar to what we achieve by fitting models to our optical spectrophotometry; see Levesque et al. 2005), or an error of 0.08 mag in the BC at K. The reddening at V varies by 0.5 mag at the faint end (Massey et al. 2009 and discussed in depth below in Sec. 7.6); at K this introduces another 0.06 mag uncertainty. Add these together with the uncertainty of 0.03 mag in the K-magnitude itself, and we achieve an uncertainty of 0.10 mag, or 0.04 dex in $\log L$. It is not clear what effect the $\sim$0.15 mag variation in K has. Perhaps it is compensated for changes in temperatures. But, even if we add this in, we achieve an error of 0.07 dex in $\log L$, not much worse than our 0.05 dex goal.

To make our observations more compatible with UKIRT's queue scheduling, we split each of the three fields into two "visits," which were separated by days or weeks as shown in Table 7.1. WFCAM consists of four Rockwell Hawaii-II (HgCdTe 2048×2048) arrays, each covering 13.65' on the sky, and separated by 12.83' gaps. The scale is 0.4" per pixel. (For further details, see Casali et al. 2007.) For each visit, we planned a sequence of exposures starting with a set of 10 individual 10-sec exposures in J. The individual exposures were co-added in order to build up the signal-to-noise. The process was then repeated in K_s, using 36 individual 10-sec exposures. The telescope was then offset by 795" (13.25') and the process executed three more times in order to fill in the gaps between the chip. The entire sequence was then executed again during the second visit on a different night. Had everything gone according to plan, each field would have been observed twice in J and K_s covering a 51' × 51' area with some overlap between the dithers. However, there was no motion between dither position 1 and dither position 2 on the first visit to Field A, resulting in a 25% loss of areal coverage for that field. The second visit was executed as planned.

The images were processed by the Cambridge Astronomical Survey Unit (CASU) and made available via the WFCAM Science Archive, part of the Wide Field Astronomy Unit hosted by the Institute for Astronomy, Royal Observatory, Edinburgh. An overview is given by Hambly et al. (2008), with complete details given at the CASU web site[5]. The data products include the calibrated chip-by-chip ("detector frame") stacked images and the corresponding chip-by-chip source catalogs with coordinates, instrumental magnitudes, aperture corrections, and photometric zero-points. The latter are based upon 2MASS stars observed throughout the night. Thanks to these expert pipeline products, our task was primarily book-keeping rather than calibration or photometry. Our process was to first transfer the FITS catalog tables into something more usable, and produce calibrated photometry for each source adopting the pipeline's "aperture 3" values, which correspond to the "core" flux, defined as a radius of 5 pixels (2.0"). According to the source catalogs, the typical (median)

[5]http://casu.ast.cam.ac.uk/surveys-projects/wfcam

seeing was 4.0 pixels (1.6"), and ranged from 3.1 pixels (1.2") to 6.5 pixels (2.6"). Correspondingly the typical (median) aperture correction was -0.21 mag, ranging from -0.14 mag to -0.48 mag.

For each field we then had 64 catalogs: 2 visits $\times$ 2 filters $\times$ 4 chips $\times$ 4 dithers. Our next task was to match detections in the J and K_s exposures for each chip/visit/dither, keeping only stars that were detected in both filters. That reduced the burden to 32 catalogs containing K_s and $J-K_s$ photometry for each chip/dither/visit. For each visit and dither we then combined the photometry of the four chips to produce 8 source catalogs of photometry. We then combined the data of the four dithers, averaging the photometry for stars in common in the regions of overlap. That resulted in two source catalogs, one for each visit. Finally, we insisted that stars be detected in each of the two visits (using a 0.5" matching criterion), producing a single catalog of objects for each field, with the photometry from the two visits averaged. (Note that this eliminated one-quarter of the coverage we would otherwise have had for field A, as one of the dithers was missing.) Thus, each star was observed at least twice in both J and K_s.

Comparing our combined photometry to the 2MASS values showed that there was invariably very little difference in the K_s-band values, but typically a $+0.025$ mag difference in the J-band photometry, with the 2MASS values being higher. We restricted the comparison to the standard 2MASS point source catalog (not the x6x version) and for stars with J and K_s values between 12.0 and 14.0 and quality ratings of "AAA." Fainter than this, the scatter in the 2MASS data were too large; brighter than 12 we found that the UKIRT magnitudes showed larger and larger differences for increasingly brighter sources, characteristic of a non-linearity or saturation effect. We thus removed any UKIRT data for stars with $J \leq 12$ or $K \leq 12$ (after correcting for the median difference compared to 2MASS), and supplemented the catalog with 2MASS sources at the brighter end. Care was taken for the 2MASS additions to Field A to make sure they fell in the same areas as the other stars were observed.

We show the final error plots in Figure 7.4. We have drawn lines corresponding to our

goal of a S/N of 30 (error 0.03 mag) at $J = 18.0$ and $K_s = 17.0$, and see that we have achieved this nicely. The 2MASS data at the bright end have larger errors, but this is somewhat deceptive as the uncertainties are not dominated by photon statistics. However, for our purposes these are moot as they are much brighter than any of the actual RSGs in our sample but are foreground objects.

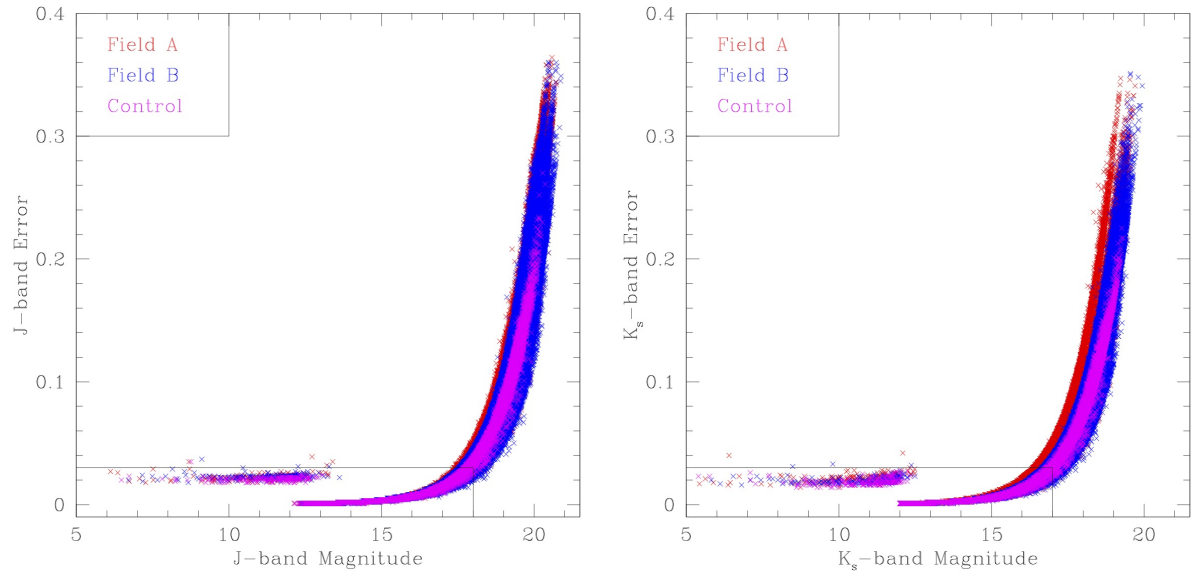

Figure 7.4 - Error plots for the photometry. The brighter stars come from the 2MASS survey (Skrutskie et al., 2006); at a given magnitude their errors will be higher than that of our deeper UKIRT data. The lines show our goal of a S/N of 30 (error 0.03 mag) at $J = 18$ and $K = 17$. © AAS. Reproduced with permission from Neugent et al. (2020b).

7.5 Identifying the Red Supergiants

Our total sample consisted of 116,692 stars in Field A, 132,837 stars in Field B, and 11,254 stars in the control field, for a total of 260,783 stars with J and K_s photometry. (We provide the full photometry lists in Tables 7.2 and 7.3.) We expect the RSG population to be a tiny fraction of this sample. This section describes how we went about identifying it.

Table 7.2. UKIRT Photometry M31 Fields A and B

α_{2000}[a]	δ_{2000}	J	σ_J	K_s	σ_{K_s}	$J-K_s$	σ_{J-K_s}	Mem[b]
00:37:50.46	+40:59:42.4	18.258	0.047	17.355	0.040	0.903	0.062	3
00:37:50.62	+40:54:45.4	18.479	0.075	16.683	0.028	1.796	0.080	3
00:37:50.65	+40:58:56.8	17.805	0.042	16.508	0.024	1.297	0.048	3
00:37:50.68	+40:53:17.7	18.930	0.089	17.997	0.079	0.933	0.119	3
00:37:50.82	+41:06:16.2	19.392	0.154	18.020	0.080	1.372	0.173	3

Note. — Table 2 is published in its entirety in Neugent et al. 2020b. A portion is shown here for guidance regarding its form and content.

[a]Stars with α_{2000} less than 00:43 are in Field A; those with larger values are from Field B.

[b]Membership flag based upon our analysis of the *Gaia* DR2 results. 0=member; 1=uncertain; 2=non-member; 3=no *Gaia* data available.

Table 7.3. UKIRT Photometry M31 Control Field

α_{2000}	δ_{2000}	J	σ_J	K_s	σ_{K_s}	$J-K_s$	σ_{J-K_s}	Mem[a]
00:33:01.37	+41:39:01.0	13.935	0.002	13.334	0.002	0.601	0.003	2
00:33:01.49	+41:38:28.6	18.494	0.055	17.793	0.064	0.701	0.084	3
00:33:01.74	+41:45:13.4	15.769	0.006	15.111	0.006	0.658	0.008	2
00:33:01.81	+41:35:33.7	16.309	0.009	15.749	0.011	0.560	0.014	2
00:33:02.02	+41:38:37.4	16.650	0.012	16.124	0.015	0.526	0.019	2

Note. — Table 3 is published in its entirety in Neugent et al. 2020b. A portion is shown here for guidance regarding its form and content.

Note. — The brightest stars are taken from the 2MASS catalog. See text.

[a]Membership flag based upon our analysis of the *Gaia* DR2 results. 0=member; 1=uncertain; 2=non-member; 3=no *Gaia* data available.

In Fig. 7.5 we show the color-magnitude diagrams (CMDs) for each of the three fields. RSGs typically have effective temperatures of 3500-4100 K, corresponding to unreddened colors $0.85 < (J-K)_0 < 1.20$ at M31's metallicity (Levesque et al., 2006). Massey et al. (2009) has measured the temperatures of 16 M31 RSGs using spectral fitting of the TiO bands employing a new generation of the MARCS stellar atmospheres (Gustafsson et al., 1975; Plez et al., 1992), finding typical $A_V \sim 1$ mag, corresponding to an $E(B-V) \sim 0.3$ or $E(J-K) \sim 0.2$. (We will delve more deeply into the reddening issue in Chapter 7.6). Thus, *roughly*, we would expect to find the RSGs between $J-K_s$ of 1.0 and 1.3 (warm/cool). As argued above, we would like to extend our detection down to $K_s \sim 16.2-16.7$ (cool/warm). The most luminous RSGs have $\log L/L_\odot$ of 5.5 (see Fig. 7.2 here and Fig. 3 in Levesque et al. 2005 corresponding roughly to $K \sim 12.5-13.0$ (cool/warm). We have outlined the relevant region in the CMDs in red. We see that the actual sequence of RSGs is a bit tilted with respect to this parallelogram, but it adequately guides the eye to the correct section of the CMD.

There will be two sources of contamination that we must concern ourselves with. The first of these is that of foreground stars; the second is that due to M31's own asymptotic giant branch (AGB) stars. We deal with both of these in the next two sections.

7.5.1 Cleaning the Sample by Removing the Foreground Stars

The first contaminant to deal with is foreground stars: red dwarfs in the Milky Way's disk, and red giants in the Milky Way's halo, can have magnitudes and colors like those of M31's RSGs (see discussion in Massey et al. 2009). *Gaia* astrometry—both proper motions and parallaxes—provides us the tools for removing the first of these; the second of these is a negligible constituent as we show below.

We can gather a quick visual impression of where foreground contamination is significant by comparing the number and location of stars in the control field to that of the two M31 fields in Figure 7.5. Few, if any, foreground stars are to be found in the region of the RSGs, while slightly warmer stars will be dominated by foreground stars. This warmer sequence is

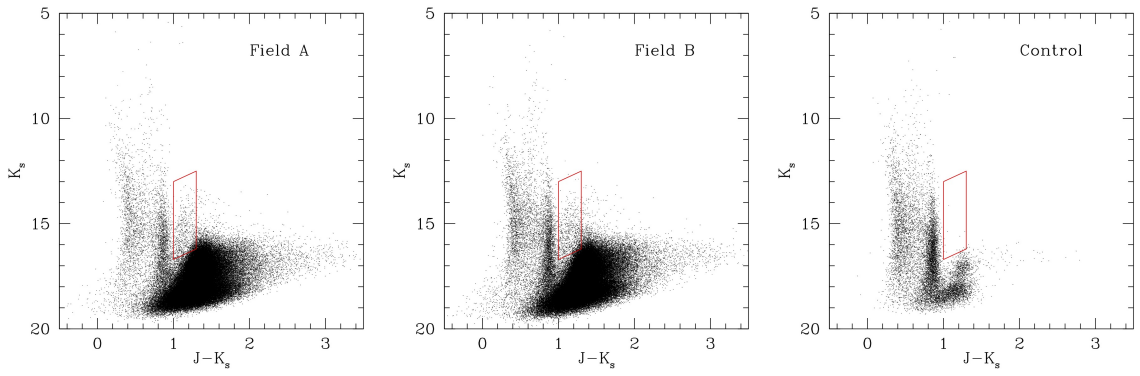

Figure 7.5 - The observed CMD for all three fields. The UKIRT photometry, supplemented by 2MASS values at $K_s < 12$ and $J < 12$ as explained in the text. The control number and location of stars in the control field gives a good impression of the degree of foreground contamination in the two M31 fields; recall that the area of Field A is only 75% of that of Field B and the control field. The red parallelogram shows the expected region of RSGs, based upon temperatures of 3500-4100 K, reddenings corresponding to $A_V = 1.0$mag, and $4.2 < \log L/L_\odot < 5.5$. © AAS. Reproduced with permission from Neugent et al. (2020b).

where the yellow supergiants (YSGs) are found, and as we have previously shown by radial velocity studies, the YSGs are a rare constituent (∼5%) in that part of the CMD (Drout et al., 2009). Stars of similar colors to our RSGs but fainter are also expected to have a strong foreground component, as seen in Figure 7.5.

Defining the Gaia Membership Criteria

We explicitly remove foreground contamination in by utilizing the proper motions (μ_α, μ_δ) and parallaxes (π) from the *Gaia* Data Release 2 (DR2). In order to astrometrically distinguish probable M31 members from likely foreground stars we follow a procedure based on that described in Gaia Collaboration et al. (2018) for the LMC/SMC. In summary: we first define a three dimensional filter in μ_α, μ_δ, and π based on a sample highly probable members of M31, and this filter is subsequently applied to the full set of UKIRT sources described

above in order to assess their consistency with the expected proper motions and parallaxes of M31 members.

In order to define our filter, we begin by selecting a sample of stars from the Local Group Galaxy Survey of M31 (Massey et al., 2007b). We restrict ourselves to stars with B-V > 1.8 and B-V < 0.3 in order to eliminate the yellow region of the color magnitude diagram, which has been shown to be >95% contaminated by foreground dwarfs Drout et al. (2009). These stars are then cross-matched with *Gaia* DR2, and we further restrict the sample to stars with G<19.5 and π/σ_π <5. We determine the median proper motions and median parallax for this sample and, finally, following Gaia Collaboration et al. (2018), we further eliminate any sources whose μ_α or μ_δ are more than four times the robust scatter estimate in order to minimize any remaining contributions from foreground stars.

Applying these cuts, we are left with a sample of ∼2200 stars, which we use to determine the covariance matrix μ of μ_α, μ_δ, and π. Based on this matrix, we define multiple filters that will be used to classify our UKIRT sources as either probable M31 members or likely foreground dwarfs. Specifically, if:

- $\mu^T\sigma^{-1}\mu > 12.8$, a star is classified as a probable foreground star. This value corresponds to the 99.5% confidence region.

- $\mu^T\sigma^{-1}\mu < 4.11$, a star is classified as a likely M31 member. This value corresponds to the 75% confidence region.

- $4.11 < \mu^T\sigma^{-1}\mu < 12.8$, a star is classified as having uncertain membership.

Eliminating the Foreground Stars

We apply these filters to our sample of UKIRT sources (in both the M31 and control fields), after cross-matching with the *Gaia* DR2 database. Of course, not all of our sources have measurements from *Gaia*—in particular, the fainter, reddest stars have no *Gaia* data.

In Fig. 7.6(a) we show a closeup of the CMD, again indicating the general region where we expect RSGs to be found. In Fig 7.6(b) we show stars with no Gaia information (blue) and those with uncertain membership status based on Gaia data (green). Finally in Fig. 7.6(c) we show only the stars certain to be members, while in Fig. 7.6(d) we show all of the data *except* the stars certain to be foreground.

What fraction of the stars with no *Gaia* data are likely to be foreground? We can answer this by appealing to the control field CMD. In Figure 7.7 we show the control field before and after removing *Gaia*-identified foreground stars. We have once again indicated the stars with no *Gaia* information by color-coding the points blue, and the ones with ambiguous results, green. By comparing Figure 7.7 (a) with 7.7(b), we see that most of the handful of stars in the RSG region on the control field (which should all be foreground stars) are correctly identified as foreground stars based on their kinematics. The remaining ones have no *Gaia* data. At fainter magnitudes ($K_s < 16$) in the same color range there are also no *Gaia* data. We will revisit this issue once we better define the region of RSGs.

We note that the control field also has proven useful in confirming that the number of halo giants contaminating our data is negligible. Giants in the MW's halo, at distances of 10 kpc or more, will have parallaxes and proper motions so tiny that even *Gaia* data (at present) has a hard time distinguishing them from members of other galaxies, at least on a star-by-star basis[6] The lack of any stars identified as members or with ambiguous information in the RSG region of the control field CMD shows that this is not a problem.

7.5.2 Removing the AGB Stars

The other contaminant is M31's own asymptotic giant branch (AGB) stars. These are the the bane of RSG population studies at lower luminosities. AGB stars are evolved low- to intermediate-mass stars that are past their core-He burning phase but undergoing He- and H-shell burning. Their temperatures are generally cooler than that of RSGs, and their

[6]Very careful analysis has allowed the tangental rotation of M31 and M33 to be measured in a *statistical* sense; see van der Marel et al. (2019).

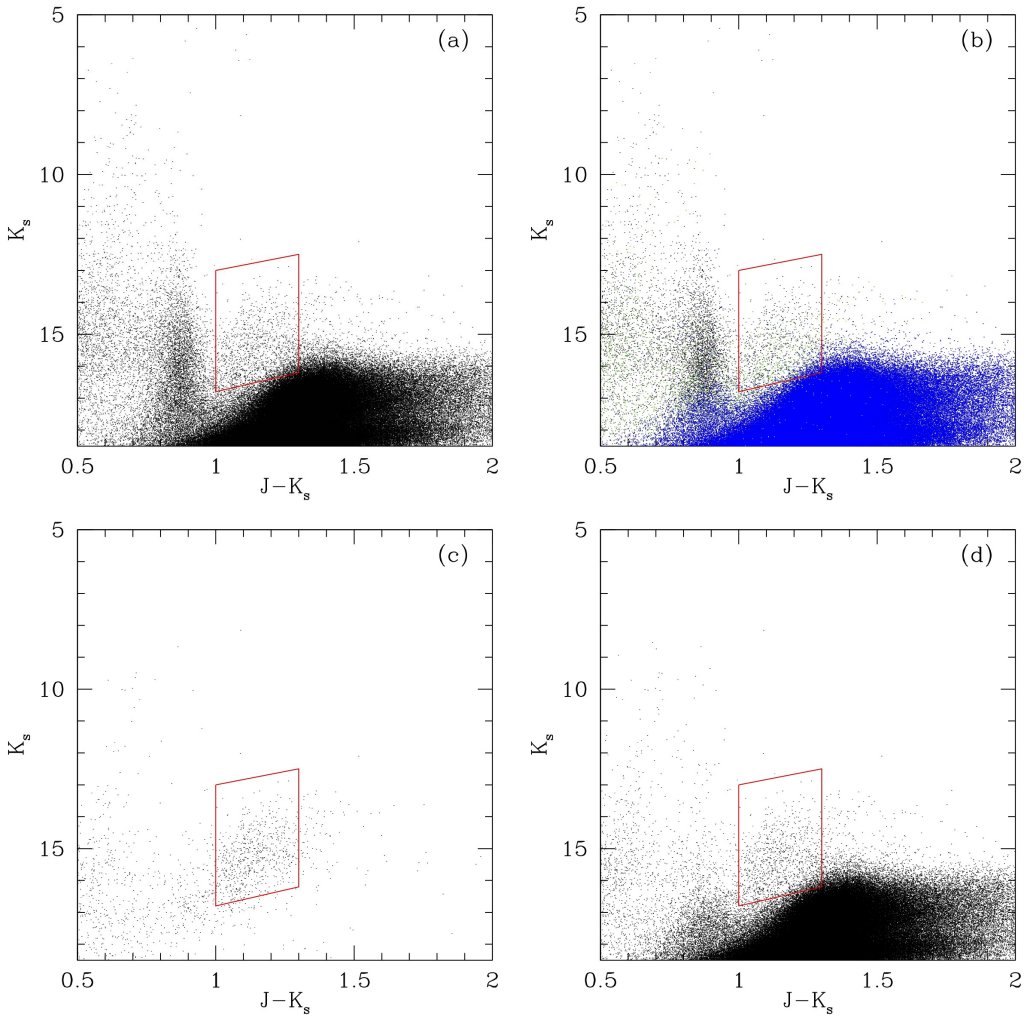

Figure 7.6 - The CMD for the two M31 fields combined. In (a) we show all of the data, with the parallelogram showing the approximate location of where we expect RSGs to be found. In (b) we color-code the data based upon whether or not the star's membership status can be determined from *Gaia* or not; the blue points have no *Gaia* data, and the green points show ambiguous membership. In (c) we show the CMD for the confirmed members only. In (d) we now only exclude the stars for which *Gaia* shows that they are clearly non-members.

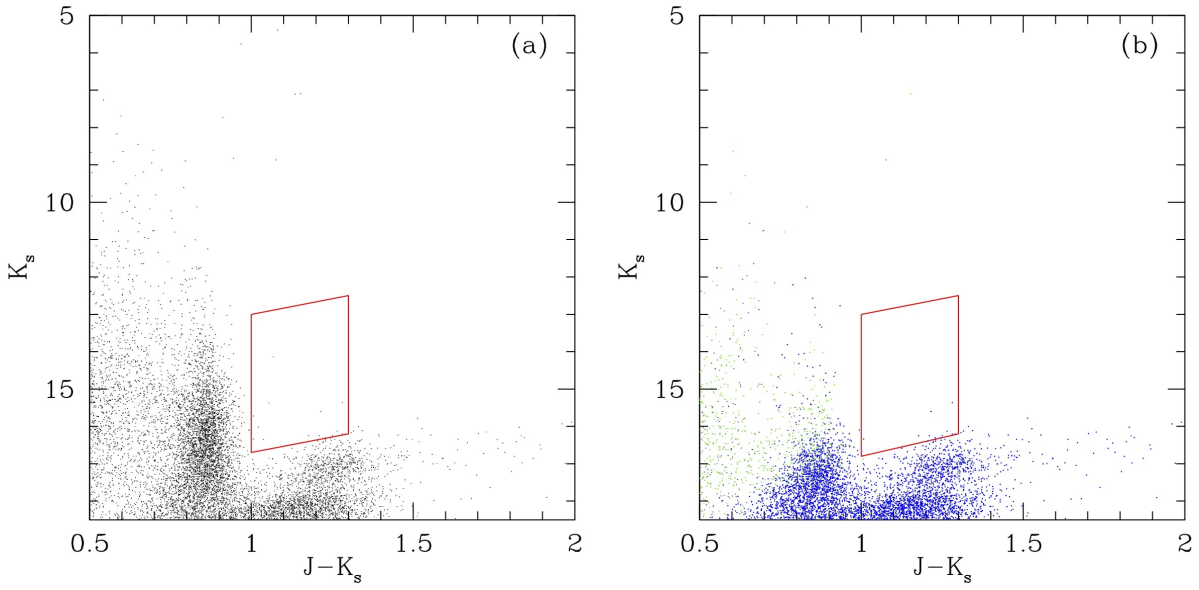

Figure 7.7 - The CMD for the control field. In (a) we show all of the data, with the parallelogram showing the approximate location of where we expect RSGs to be found. In (b) we have removed the *Gaia*-selected foreground stars, and color-coded the data based upon whether or not the star's membership status can be determined. As with the previous figures, the blue points have no *Gaia* data, and the green points show ambiguous membership. © AAS. Reproduced with permission from Neugent et al. (2020b).

luminosities overlap those of the lower mass RSGs. Brunish et al. (1986) may have been the first to emphasize the potential confusion between intermediate-mass AGB stars and RSGs in stellar population studies, and suggested that at luminosities below $\log L/L_{\odot} = 4.9$ there could be overlap in luminosity. Studies like Massey & Olsen (2003) often adopt this as a cut-off; that luminosity roughly corresponds to $20M_{\odot}$ (see, e.g., Figure 2 in Ekström et al. 2012). Of course, we would like to go much lower than that.

However, with good NIR colors it is relatively easy to separate RSGs and AGBs at lower luminosities, as AGBs are significantly cooler. Cioni et al. (2006) and Boyer et al. (2011) showed that one could in fact readily separate the various types of AGBs (carbon-rich,

oxygen-rich) from one another, as well as separate the AGBs from RSGs. This has most recently been used by Yang et al. (2019) in the SMC, who claim unambiguous separation of RSGs from AGBs down to the tip of the red giant branch at about $K_s = 12.7$ in the SMC, which would roughly correspond to $K_s = 18.1$ in M31. This is 1.5 mag deeper than we need to go to achieve $\log L/L_\odot = 4.0$.

In Fig. 7.8 (a) the two diagonal magenta lines show the Yang et al. (2019) color cuts for RSGs using their "CB" method (i.e., based on Cioni et al. 2006 and Boyer et al. 2011), adjusted for the difference in distances (59 kpc for the SMC and 760 kpc for M31, according to van den Bergh 2000 and references therein) and by 0.16 mag in $J - K_s$. The latter was determined first empirically by eye, but is consistent with what we expect due to the change of the Hayashi limit with metallicity. The typical RSG in the SMC is a K2-3 I with a typical temperature of 4000 K (Levesque et al. 2006, Table 4). According to the MARCS models, this corresponds to a $(J - K)_0$ of 0.951 at SMC metallicity. The typical RSG in M31 is an M2 I with a temperature of 3600 K (Massey et al. 2009, Table 5). According to the MARCS models this correspond to a $(J - K)_0$ of 1.121. Converting this 0.17 difference in $(J - K)_0$ translates to a difference of 0.16 in $(J - K_s)_0$ according to the transformation equation of Carpenter (2001), as discussed below in Sec. 7.6, a rather remarkable, and perhaps fortuitous, agreement. We defined the width of the RSG band to be 0.25 mag wide in $J - K_s$, slightly larger than the 0.20 wide boundary adopted by Boyer et al. 2011. We list the equations for these two lines in Table 7.4. The blue points in that figure show the stars for which there are no *Gaia* data; this set is dominate by the AGBs. We see that that the vast majority of points to the left of our parallelogram have ambiguous membership; we believe most of these stars are foreground.

Based on this we now identify the RSGs in Fig. 7.8 (b). We have relaxed the upper temperature limit slightly, and at brighter magnitudes we accept slightly cooler stars. As Yang et al. (2019) argues this could contaminate the upper luminosity sample lightly by super-AGBs but the degree should be small and allows for the existence of dusty high-luminosity RSGs. The adopted limits are as follows:

Table 7.4. M31 Adopted and Derived Relations

Relation	Reference
Adopted Distances:	
M31: 760 kpc	1
SMC: 59 kpc	1
Reddening Relations:	
$A_V = 3.1E(B-V)$	···
$A_K = 0.12A_V = 0.367E(B-V) = 0.686E(J-K)$	2
$E(J-K) = A_V/5.79 = 0.535E(B-V)$	2
Photometric Criteria for RSGs with $K_s \leq 17.0$	
$0.87 < (J-K_s) \leq 1.0$: $K_0 \leq K_s$	3
$1.0 < (J-K_s) \leq 1.3$: $K_0 \leq K_s \leq K_1$	3
$1.3 < (J-K_s) \leq 1.5$: $K_s \leq 14.4$	3
$K_0 = 28.62 - 13.33(J-K_s)$	3,4
$K_1 = 31.95 - 13.33(J-K_s)$	3,4
Adopted Extinction	
$K_s > 14.5$: $A_V = 0.75$	3
$K_s < 14.5$: $A_V = 0.75 - 1.26(K_s - 14.5)$	3
Conversion from 2MASS (J, K_s) to Standard System (J, K):	
$K = K_s + 0.044$	5
$J-K = (J-K_s + 0.011)/0.972$	5
Conversion to Physical Properties (Valid for 3500-4500 K):	
$T_{\rm eff} = 5643.5 - 1807.1(J-K)_0$	3
$\mathrm{BC}_K = 5.567 - 0.7569 \times T_{\rm eff}/1000$	3
$K_0 = K - A_K$	···
$M_{\rm bol} = K_0 + \mathrm{BC}_K - 24.40$	···
$\log L/L_\odot = (M_{\rm bol} - 4.75)/-2.5$	···

References. — 1–van den Bergh 2000; 2–Schlegel et al. 1998; 3–Neugent et al. 2020b (Chapter 7); 4–Cioni et al. 2006; 5–Carpenter 2001

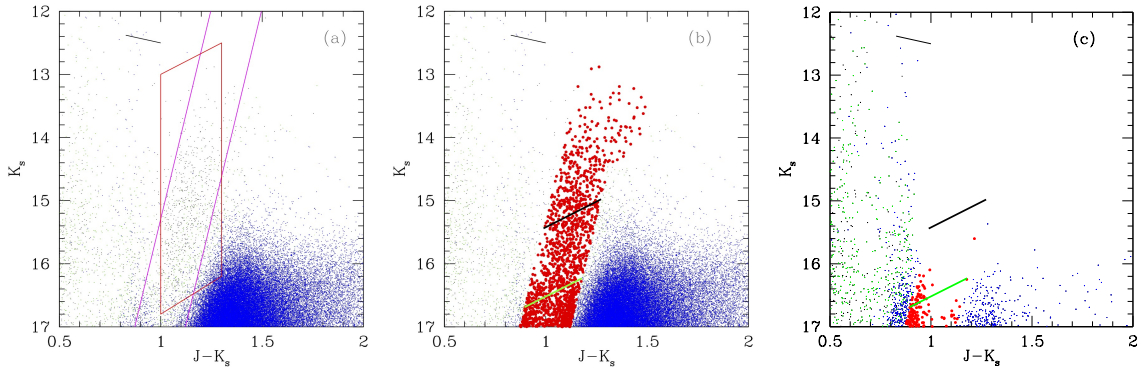

Figure 7.8 - The Identification of RSGs. (a) The two magenta lines denote the region expected to be RSGs based on the "CB" method of Yang et al. (2019), with a 0.16 mag adjustment in $(J - K_s)$ due to the expected shift in the temperature of RSGs from the SMC to M31, and a 5.55 mag adjustment in K_s due to the greater distance of M31 compared to the SMC. The blue points are stars without membership data, and the green points are the ones with ambiguous membership data. Non-members have been removed. The line at upper left shows the reddening vector corresponding to $A_V = 1.0$ mag. (b) The same as (a), but now with the adopted RSGs indicated by larger red points. The thick green diagonal line going through the RSG points denotes $\log L/L_\odot = 4.0$, our limit. For comparison $\log L/L_\odot = 4.5$ is denoted by the black line. (c) The same as (b) but for the control field. The "RSGs" in this field (large red points) are likely all foreground objects, and their numbers will be used to correct the luminosity function we derive. © AAS. Reproduced with permission from Neugent et al. (2020b).

- $0.87 \leq (J - K_s) \leq 1.15$, $K_s \leq 17.0$ and $K_s < K_1$
- $1.15 < (J - K_s) \leq 1.32$, $K_s \leq 31.873 - 13.235(J - K_s)$
- $1.32 < (J - K_s) \leq 1.50$, $K_s \leq 14.40$

We include members, uncertain members, and stars without *Gaia* information, excluding only the *Gaia*-identified foreground stars. The green line corresponds to our luminosity

cutoff $\log L/L_\odot > 4.0$; we can see that there is still a considerable gap between the coolest star and the mountain of AGBs.

In Fig. 7.8(c) we show the same information for the control field. We see that within the RSG region there is considerable contamination at the fainter magnitudes and warmer temperatures. (This contamination is less than a few percent for $K_s < 16$ but 30% at the faintest magnitudes we include in determining our M31 RSG luminosity function.) We could simply correct our luminosity function for these stars, under the assumption that they are all foreground. However, an examination of the spatial distribution of these control field stars show that for stars with $\log L/L_\odot \geq 4.0$, there are 2.3× more control field stars on the side closest to M31 compared to the side furthest from M31. We will count only the stars on the western half of the control field in correcting our RSG luminosity function (and of course scaling their numbers by the relative areas), and keep in mind that even so we may be slightly overestimating the size of the correction.

7.6 Transformations of Photometry to Effective Temperatures and Bolometric Luminosities

In order to construct a luminosity function, we must use our photometry to determine bolometric luminosities; this requires that we derive effective temperatures and the resulting bolometric corrections. Our first step is to transform our UKIRT photometry (tied to the 2MASS J, K_s system) to the standard Bessell & Brett (1988) (BB) system, as these standard bandpasses were used in computing the expected colors from the MARCS stellar atmospheres (see Bessell et al. 1998). Carpenter (2001) provides transformations from standard system to 2MASS. Inverting these we find:

$$(J-K)_{\rm BB} = \frac{[(J-K_{\rm 2MASS}+0.11]}{0.972}$$

and

$$K_{\rm BB} = K_{\rm 2MASS} - 0.044.$$

The next step was to correct the photometry for reddening. Massey et al. (2007b) finds

that the average reddening for OB stars in M31 is $E(B-V) = 0.13$, or $A_V = 0.40$. However, as mentioned above, RSGs are usually considerably more reddened than their neighboring OB stars due to circumstellar dust (Massey et al., 2005). We would ideally like to correct the photometry for each star individually. We have succeeded in that by fitting the spectra with MARCs models (i.e., Levesque et al. 2005, 2006; Massey et al. 2009). We could simply adopt a single "moderate" value for the extinction, say, $A_V = 1.0$, but this overlooks the fact that in general the higher luminosity RSGs are more heavily reddened than lower luminosity RSGs. For instance, the M31 stars analyzed by Massey et al. (2009) show a strong trend in A_V with bolometric luminosity, with the more luminous stars showing the greater reddening.

We illustrate the correlation in Fig. 7.9(a). To show this is not simply a logical tautology (since the stars' luminosities are computed using the adopted extinctions), we show in Fig 7.9(b) a similar plot where we have replaced the abscissa values with the uncorrected K_s-band photometry. Although the scatter is larger, particularly at the low luminosity end, the same trend is seen; RSGs in M31 that have brighter K values show more extinction. Recall that $A_K = 0.12 A_V$ and $E(J-K) = A_V/5.8$; i.e., we expect a color excess of 0.10-0.20 in $J - K_s$ at low luminosities ($\log L/L_\odot < 4.8$) but $0.35 - 0.45$ at higher luminosities.

We have therefore decided to adopt a color-dependent relation for the extinction. For $K_s \geq 14.5$ we adopt $A_V = 0.75$ mag, i.e., $A_K = 0.09$ mag, and $E(J-K) = 0.13$. For brighter stars, we adopt $A_V = 0.75 - 1.26(K_s - 14.5)$. For our brightest stars this translates to $A_V \sim 2.0$, or $A_K = 0.25$ mag, with $E(J-K) = 0.34$.

We then transformed these magnitudes and colors to effective temperatures and bolometric luminosities via the MARCS models. As part of our previous work, our collaborator Bertrand Plez (private communication 2005, 2009) provided us with tables of colors and bolometric corrections for each model. We used these to derive new relationships based upon the solar metallicity models used by Levesque et al. (2005) and 1.8× solar models used by Massey et al. (2009); the best determinations of the H II region abundances in M31 suggest a metallicity of ∼1.5 solar based upon the oxygen abundances (Sanders et al., 2012). We restrict ourselves to the $\log g$=0.0 models as these are the most appropriate for the RSGs

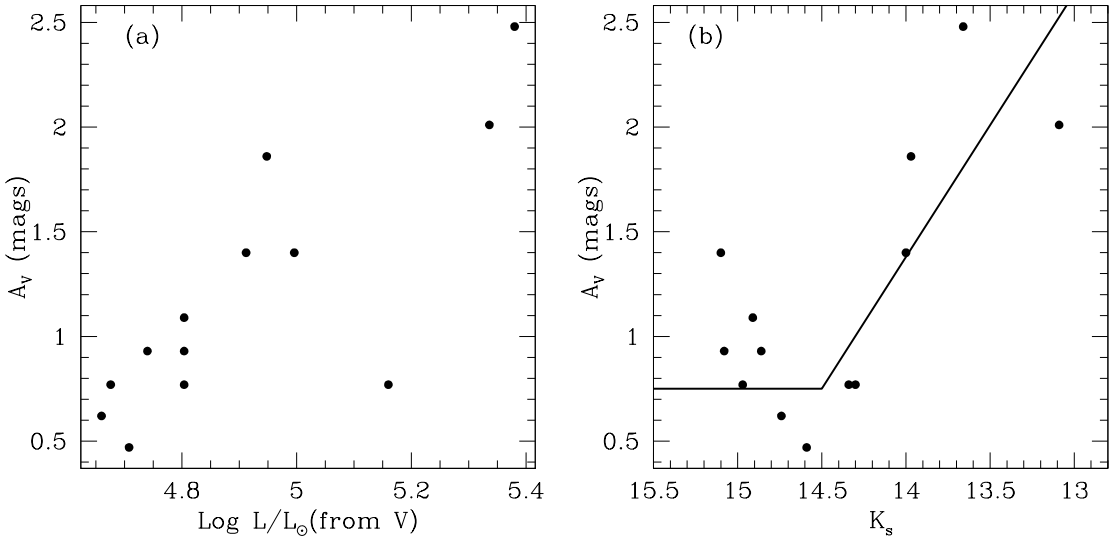

Figure 7.9 - Extinction of Previously Analyzed M31 RSGs. (a) The extinction A_V is shown as a function of the bolometric luminosity for the sample of stars analyzed by Massey et al. (2009). (b) Same as (a), but now with the extinction plotted as a function of K_s magnitude as given by Massey et al. (2009). The adopted extinction relation is shown by the solid line. © AAS. Reproduced with permission from Neugent et al. (2020b).

with known physical properties (Levesque et al., 2005, 2006; Massey et al., 2009). We find that the relationships are quite linear over the relevant temperature range (3500-4500 K):

$$T_{\rm eff} = 5643.5 - 1807.1 \times (J-K)_0$$

and

$$BC_K = 5.567 - 0.757 \times \frac{T_{\rm eff}}{1000}.$$

Our adopted distance to M31 of 760 kpc is equivalent to a true distance modulus of 24.40. Thus

$$M_{\rm bol} = K_0 + BC_K - 24.40,$$

and

$$\log L/L_\odot = \frac{M_{\rm bol} - 4.75}{-2.5},$$

where we have adopted the bolometric luminosity of the sun as 4.75.

With these conversions, and our adopted reddenings, we now show in our CMD the limits corresponding to $\log L/L_{\odot}$ 3.95 (the lowest part of 0.1 dex wide bin centered on $\log L/L_{\odot}$=4.0). Recall from our discussion of our error budget in Chapter 7.4: our errors even at the faintest magnitude levels correspond to <100 K (about 0.01 dex) in temperature, and 0.04 dex in $\log L$.

7.7 Model Comparisons

Figure 7.10 now shows the location of our RSG sample in the H-R diagram. In (a) we have adopted the above relationship between the extinction and brightness. We see that the location of the points are very good match to the location of the Geneva evolutionary tracks, and even turn back towards higher temperatures at higher luminosities. In (b) we adopt a constant value $A_V = 1.0$ mag following Massey & Evans (2016). The lower luminosity points are too warm compared to the tracks, and the higher luminosity points scatter to much cooler temperatures than the tracks.

In (a) we do find three rather high luminosity RSGs with $\log L/L_{\odot} > 5.5$. The *Gaia* data for all three of these strongly indicate membership in M31. It is possible of course that for these stars our method for computing the extinction has resulted in an overestimate for both the temperature and luminosity. Adopting an average $A_V = 1.0$ mag for these stars would result in moving these points down to where the top three points are in (b), a significant change. The luminosity of the most luminous RSG is of considerable interest (see, e.g., Massey et al. 2009), and we plan to obtain spectrophotometry of these three stars and measure their reddening accurately using their SEDs. Until then, we will treat the luminosities of those three stars as uncertain. If these high luminosities are correct, this stands at odds with the result found by Davies et al. (2018) that the maximum luminosity of RSGs is in the region of $\log L/L_{\odot} = 5.5$. Massey et al. (2009) found, and Davies et al. (2018) confirmed, that there does not appear to be a metallicity dependence on the maximum luminosity, and thus the RSGs we have discovered here in M31 should not be any more

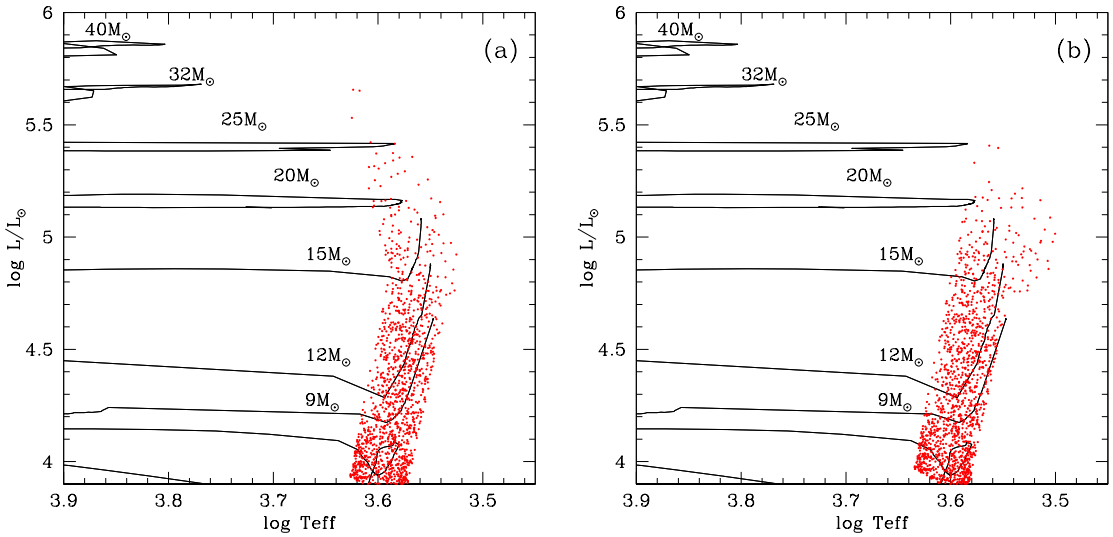

Figure 7.10 - HRD for our RSG sample. The tracks shown are from Ekström et al. (2012) computed for solar ($z = 0.014$) metallicity and with an initial rotation of 40% of the breakup speed at ZAMS. (a) The location of our RSGs are shown using the adopted K-dependent relationship for the extinction. The turn towards higher temperatures at higher luminosities is consistent with the location of the tracks. (b) The location of the RSGs assuming a constant value for the extinction (equivalent to $A_V = 1.0$), similar to what was done by Massey & Evans (2016). Note the deviation from the location of the tracks. © AAS. Reproduced with permission from Neugent et al. (2020b).

luminous than those found by Davies et al. (2018) in the Magellanic Clouds. If anything, we would expect them to be less luminous, given the shift of the atmospheric Eddington limit to lower values at higher metallicity; see discussion in Lamers & Levesque (2017). We will revisit this issue in a future paper after we have investigated the RSG content of other galaxies in the Local Group.

With a better understanding of the RSG population of M31 in hand, we compared our results with that of the SYnthetic CLusters Isochrones & Stellar Tracks (SYCLIST) models created by the Geneva Evolutionary group to check which mass-loss rate during the RSG

phase best fits the observed luminosity function. A full description of SYCLIST can be found in Georgy et al. (2014a). As one of its many functions, it computes stellar populations as a function of time based on evolutionary tracks that are given as input. The model we used included 1000 stars within the cluster and a Salpeter IMF (Salpeter, 1955). Our minimum mass of $8M_{\odot}$ and maximum mass of $30M_{\odot}$ came from the expected mass range of RSGs. For our calculation we ignored the effects of binaries. We compute the positions of stars in the HRD for single-aged populations with ages between 0 and 1.6×10^8 years (corresponding to the total lifetime of the lowest initial mass star considered here) with time steps of 32,000 years (making 5000 steps). The program outputs, among other things, the mass-loss rate vs. luminosity for 1, 10× and 25× the mass-loss rates described in Meynet & Maeder (2002), following the arguments of Georgy (2012) and Meynet et al. (2015). To get the luminosity distribution functions for the continuous star formation hypothesis, the models at each time step are summed up.

We next compared the luminosity functions given by our sample of M31 RSGs to the SYCLIST model predictions. In Figure 7.11(a) the uncorrected luminosity function is shown by the black histogram; the correction for foreground stars is shown as a dashed line, and recall from the discussion above that this will likely be an *over*-correction. We compare this to the three SYCLIST predictions: the currently used Geneva mass-loss rate prescriptions (as described in Ekström et al. 2012), and values enhanced by 10× and 25×. There are 1145 stars at luminosities $\log L/L_{\odot} \geq 4.0$. The sum of the SYCLIST luminosity function is normalized to unity, and we have adjusted the output in accord with the total number of stars and bin size of our histogram. Thus both the shape and the actual values are meaningful in comparing the theoretical predictions with the observations.

We were also curious how much our choice of a luminosity-dependent reddening correction influenced our results. In Figure 7.11(b) we show the luminosity function obtained by adopting a constant $A_V = 1.0$ mag. We find that our findings are robust: the current Geneva RSG mass-loss prescription still does an excellent job of matching the observations, while the two enhanced (10× and 25×) versions do not. Figure 7.11(c) includes the BPASS 2.2.1

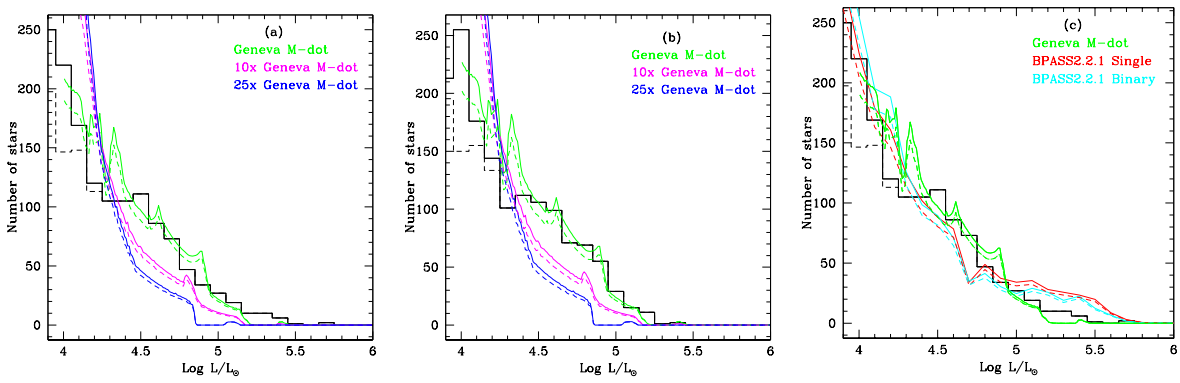

Figure 7.11 - Luminosity histogram compared to mass-loss rate model predictions. (a) The figure shows the observed luminosity histogram of M31 RSGs as determined by the UKIRT data. The black histogram is the combined data from fields A and B in M31, while the dashed shows the effect of the correction of the results from the control field scaled to the same area, and likely is an over-correction. The SYCLIST predictions are shown by three colored curves for different mass-loss rates during the RSG phase. The currently used Geneva mass-loss rate matches the observations; the 10× and 25× enhanced rates predict far too few high luminosity RSGs and too many lower luminosity RSGs for a given number of stars. (b) The same as (a) but using a constant $A_V = 1.0$ mag in computing the luminosities. (c) BPASS 2.2.1 model predictions for both single stars (red) and binaries (blue) with the Geneva single-star predictions included in green for comparison. © AAS. Reproduced with permission from Neugent et al. (2020b).

model predictions for both single and binary stars, showing that these models also match the observations well, except for over predicting the number of high luminosity RSGs. For the BPASS models this is presumably due to the adoption of the de Jager et al. (1988) RSG mass-loss rate, without accounting for the supra-Eddington losses that occur for for the highest luminosities.

Our results are quite striking. By comparing the luminosity histograms with the model outputs, we can see that the current prescription for mass-loss rates does an incredibly good

job of matching the estimating the number of lower luminosity stars (under $\sim \log L_{\odot} = 4.5$). In contrast, the 10× and 25× enhanced mass-loss models both underestimate the number of higher luminosity RSGs, and grossly over-estimate the number of lower luminosity RSGs. This suggests that the RSG mass-loss rates are currently in use are actually a very good approximation to reality both for the Geneva mass-loss rates and BPASS 2.2.1 models.

We can quantitatively describe the agreement between the observed distribution and that of the Geneva models by running a Kolmogorov-Smirnov (KS) test. A comparison between the currently used Geneva mass-loss rates and the observed distribution returns a p-value of 0.97. Comparing our observations to the 10× and 25× enhanced mass-loss models produce p-values of 0.30 and 0.12, respectively. Since the p-value of the current used Geneva mass-loss rates is so close to 1, this objectively shows that they are a good match to observations. KS tests on both the BPASS 2.2.1 single and binary star model models produce p-values of 0.96 suggesting good agreement to the observations as well.

7.8 Discussion

Based on our observations of the luminosities of M31 RSGs, we conclude that the current mass-loss prescriptions in use by the Geneva evolutionary group and described in Ekström et al. (2012) are well matched to both our observations and thus what occurs physically. While it is discussed in detail in Ekström et al. (2012), Section 2.6, we briefly go over the mass-loss rate prescriptions used in the models for RSGs here. For RSGs up to $12M_{\odot}$, the mass-loss rates are adopted from Reimers (1975, 1977). For RSGs above $15M_{\odot}$, the mass-loss rate depends on the temperature. For stars with $\log T_{\rm eff} > 3.7$, the rates come from de Jager et al. (1988) while for RSGs with $\log T_{\rm eff} < 3.7$, the rates come from a linear fit to the data from Sylvester et al. (1998) and van Loon et al. (1999). For the rotating models (that we use here for comparison), there is an additional correction factor applied as described by Maeder & Meynet (2000). However, as we discussed in the Introduction, RSGs are quite unstable and undergo episodic mass-loss rate events with some unknown frequency. In these instances, the external layers of the RSG's envelope exceeds the Eddington luminosity. The

Geneva models are not able to model the mass-loss rates in these instances directly using their hydrostatic approaches because the systems are so unstable. Thus, they artificially increase the mass-loss rate of the star by a factor of three whenever the luminosity of any of the layers of the envelope is higher than the Eddington luminosity by a factor of five. This takes into account the differing mass-loss rates caused by episodic instabilities. Based on our observations we find that this method of increasing the mass-loss rates during times of high instability produces a good fit to the observed time-averaged RSG mass-loss rate.

This discovery suggests that the majority of RSGs *will not* evolve back across the HRD and become post-RSG YSGs. We note however that in the upper luminosity range (above $\sim \log L/L_{\odot} = 5.15$, or an initial mass above $20M_{\odot}$), the models of Ekström et al. (2012) predict that most of the RSGs will evolve back in the blue. Previous surveys of YSGs in the LMC and M33 found that the Geneva Evolutionary models were able to correctly predict the relative lifetimes of YSGs at varying luminosities (Neugent et al., 2012b; Drout et al., 2012) and our result here lends further credence to the accuracy of the models. From an observational point of view, it is difficult to distinguish the difference between YSGs moving rightward and leftward across the HRD. However, steps are being taken to do just that. It has been argued that the stars' rotational velocities will slow down, they may experience periodicity or pulsations, and certain chemical elements will be enhanced. The presence of enhanced pulsations in blue supergiants as post RSG objects was discussed by Saio et al. (2013) and Georgy et al. (2014b). Using TESS data, Dorn-Wallenstein et al. (2019) modeled the variability of four YSGs finding that one of them showed drastically different variability from the other three. They hypothesized that this could be a post-RSG object as it is additionally quite dusty. It will be interesting to differentiate between post and pre-RSG YSGs observationally in the future.

Since the RSG lifetime depends upon the mass-loss rate, an additional test will be comparing the number of RSGs to WRs as a function of metallicity. Maeder et al. (1980) has argued that this ratio should be a sensitive function of metallicity as higher metallicity lends itself to WR production. The author is also currently undertaking a project that will allow

us to compare this ratio to model predictions, ideally over a range of metallicities.

7.9 Summary and Conclusions

As Georgy et al. (2013) puts it, "Of the most relevant parameters determining the evolution of massive stars, ... the mass-loss rate during the RSG phase, is the least constrained by the observations or theory." As part of our work, we hoped to remedy this situation by comparing the observed RSG mass-loss rates with those predicted by single-star evolutionary theory. We used new UKIRT data to obtain deep, accurate NIR photometry of stars in two fields in M31. We separated out the RSGs from the foreground stars and AGBs using both *Gaia* and color-color cuts down to RSGs of $\log L/L_{\odot} > 4.0$. We then calculated the theoretically expected luminosity functions using SYCLIST adopting three different time-averaged mass-loss rates. Comparisons with our observed RSG luminosity function show that the actual RSG mass-loss rates are well represented by the Geneva evolutionary models as described by Ekström et al. (2012) and the BPASS 2.2.1 single and binary star models as described by (Stanway & Eldridge, 2018). Significantly higher (10-25×) mass-loss rates are not consistent with our data. However, our collaborators in Geneva are currently computing models with the "old" standard mass-loss rates which we will compare to the same data to see if indeed the older rates don't work.

7.10 Project #2: RSG Mergers

While the majority of this work focused on better understanding binary RSGs, there is still a completely uncharacterized subset of RSGs yet to be studied - those that were once in a binary system, but have since merged. In such a case, the binary system starts off with two main sequence OB stars. Over time, the more massive star evolves first and eventually turns into a RSG with a companion. If the two stars are close enough, they will influence each other's orbits, begin tidally spinning up, and transfer angular momenta. As they merge, their rotational velocities will increase from around 5 km s^{-1} up to 15 km s^{-1} (de Mink et al., 2014). Such rotational velocities can be measured with high resolution spectra in an

attempt to observationally determine whether an apparently single RSG is actually a merger product.

While a RSG merger hasn't been directly observed, it has been offered as an explanation for why one of the most famous RSGs is spinning so fast. Betelgeuse has a projected rotational velocity of around 15 km s^{-1}, much higher than that of a normal RSG. Wheeler et al. (2017) suggest that this increased velocity could be due to a past merger with a smaller mass companion. de Mink et al. (2014) estimate that 19% of massive, apparent single stars, are actually the result of mergers. However, this has never been confirmed observationally. We are in the process of observing a statistically robust sample of single RSGs to identify the fraction of RSGs that have undergone a merger. This will give us a complete picture of the fate of both single and binary RSGs right before they end their lives as supernovae.

7.11 The High Resolution Spectral Data

We expect merged RSGs to have slightly higher rotational velocities since the stars will have tidally spun up during the process of merging. Such rotational velocities should be measurable with high spectral resolution data. Thus, we have spent the Fall 2020 semester observing 70 Galactic RSGs using the EXtreme PREcision Spectrograph (EXPRES) on Lowell Observatory's 4.3-m Lowell Discovery Telescope (LDT) during ten half-nights. EXPRES is an ultra-high resolution ($R = 137,500$) spectrograph built by D. Fischer and C. Jurgenson under an NSF-funded MRI program (Jurgenson et al., 2016; Blackman et al., 2020; Petersburg et al., 2020). The resulting spectra span a wavelength range of ∼5000 - 8100Å and, using our calibration setup, achieves radial velocity measurements on the order of 1 m s^{-1} precision. All 70 Galactic RSGs were observed with S/N > 200 per resolution element. A full list of the observed Galactic RSGs is shown in Table 7.5. Reductions were completed as part of the EXPRES pipeline as described in Blackman et al. (2020); Petersburg et al. (2020). The spectrum of one of our observed Galactic RSGs, CE Tau, is shown in Figure 7.12.

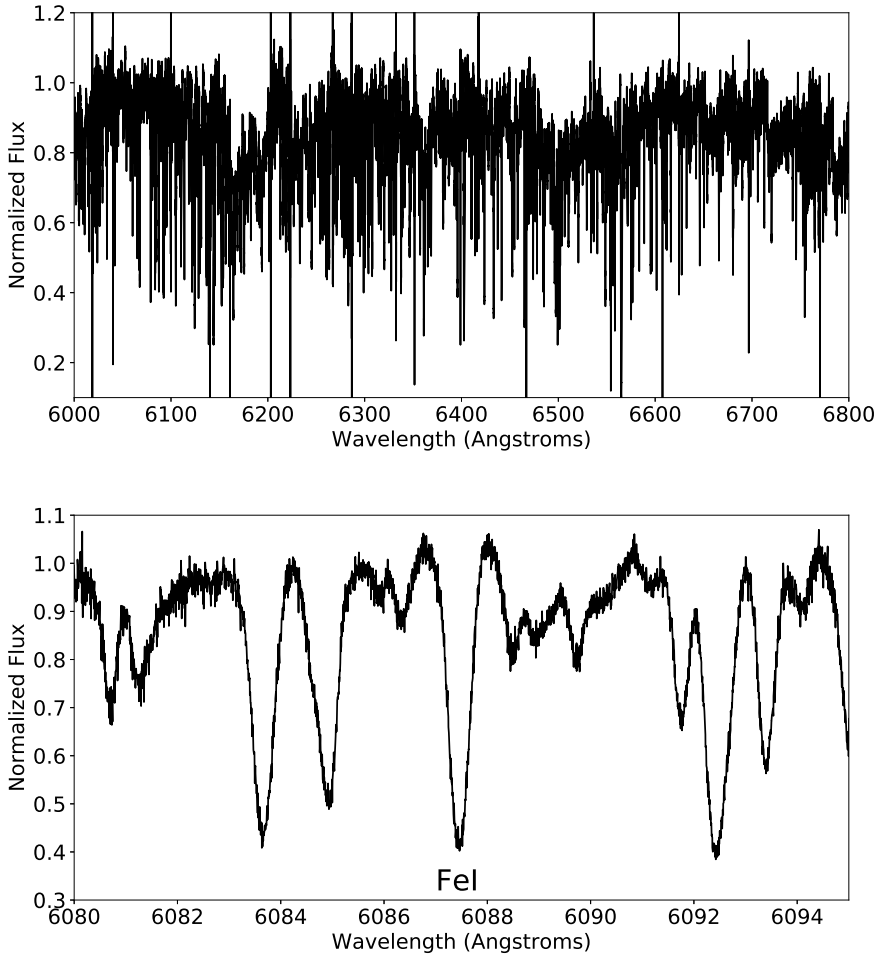

Figure 7.12 – Spectrum of Galactic RSG CE Tau taken with EXPRES with a resolving power $R \sim 150,000$ and a S/N$\sim$200 per spectral resolution element. Top: Note the large number of narrow photospheric metal lines that can be used to determine the star's rotational velocity. Bottom: Subset of the spectrum showing an example Fe I line.

Table 7.5. Galactic RSGs Observed with EXPRES

Star Name	α_{2000}	δ_{2000}	V	Type	Ref*
KN Cas	00 09 36.4	+62 40 04	9.5	M2Iep+B2.5III:	2
MZ Cas	00 21 24.3	+59 57 11	9.7	M2Ia-Iab	1
V466 Cas	01 19 53.6	+58 18 31	8.6	M0.5Ib	1
BD+59 274	01 33 29.2	+60 38 48	8.5	M0.5Ib-II	1
AZ Cas	01 42 16.5	+61 25 16	9.2	M0Ib:ep+B	2
V589 Cas	01 46 05.5	+60 59 37	9.0	M3Iab-Ib	1
V774 Cas	01 47 00.0	+60 22 20	8.6	M3Iab-Ib	1
V778 Cas	01 58 28.9	+59 16 09	8.4	M2Iab	1
BD+59 372	01 59 39.7	+60 15 02	9.4	K5/M0Ib	1
XX Per	02 03 09.4	+55 13 57	8.2	M4Ib+	2
HD 236947	02 07 12.1	+58 47 16	8.6	M2III	2
KK Per	02 10 15.8	+56 33 33	7.7	M2Iab-Ib	2
V550 Per	02 15 13.3	+58 08 32	8.9	M0-M1I	2
T Per	02 19 21.9	+58 57 40	8.5	M2Iab	2
V605 Cas	02 20 22.5	+59 40 17	8.4	M2Iab	2
AD Per	02 20 29.0	+56 59 35	7.9	M3Iab	2
FZ Per	02 20 59.7	+57 09 30	8.0	M1Iab	2
PR Per	02 21 42.4	+57 51 46	8.0	M1-Iab-Ib	2
SU Per	02 22 06.9	+56 36 15	9.4	M3-M4Iab	1
RS Per	02 22 24.3	+57 06 34	7.8	M3.5IabFe-1	1
S Per	02 22 51.7	+58 35 11	7.9	M4.5-7Iae	1
V439 Per	02 23 11.1	+57 11 58	8.2	M0.5Iab	1
V403 Per	02 23 24.1	+57 12 43	8.5	M0Iab	1
V441 Per	02 25 21.9	+57 26 14	8.2	M3Iab	1
YZ Per	02 38 25.4	+57 02 46	10.0	M1Iab	1
W Per	02 50 37.9	+56 59 00	9.6	M3Iab-M5I	1
V648 Cas	02 51 03.9	+57 51 20	9.4	M2Ia	1
HD 17958	02 56 24.6	+64 19 57	6.2	K3Ib	1
BE Cam	03 49 31.3	+65 31 34	4.4	M2II	1
HD 33299	05 10 35.0	+30 47 51	6.7	K0-Ib	1
V362 Aur	05 27 10.2	+29 55 16	7.3	M1.5Ib	1
119 Tau	05 32 12.8	+18 35 39	4.3	M2Iab-Ib	1
CE Tau	05 32 12.8	+18 35 39	1.8	M2Iab-Ib	2
NO Aur	05 40 42.1	+31 55 14	6.2	M2Iab	1
alf Ori	05 55 10.3	+07 24 25	0.4	M1-M2Ia-Iab	1
TV Gem	06 11 51.4	+21 52 06	6.6	M0-M1.5Iab	1
WY Gem	06 11 56.3	+23 12 25	7.4	M2Iabep+B:	2
6 Gem	06 12 19.1	+22 54 31	6.4	M1-M2Ia-Iab	1
psi01 Aur	06 24 53.9	+49 17 16	4.8	K5-M1Iab-Ib	1
omi01 CMa	06 54 08.0	−24 11 03	3.9	K2Iab	1
41 Gem	07 00 15.8	+16 04 44	5.7	K3-Ib	1
sig CMa	07 01 43.1	−27 56 05	3.5	K5Ib	2
QY Pup	07 47 38.5	−15 59 26	6.3	K1Ia-Iab	1
alf Sco	16 29 24.5	−26 25 55	0.9	M0.5Iab+B3V:	2
alf Her	17 14 38.9	+14 23 25	3.1	M5Ib-II+G5III+F2V:	1
HD 163428	17 57 07.5	−23 56 21	6.7	K5II	2
AX Sgr	18 08 26.5	−18 33 08	9.2	K0Ia	2
del02 Lyr	18 54 30.3	+36 53 55	4.3	M4II	1

Table 7.5 (cont'd)

Star Name	α_{2000}	δ_{2000}	V	Type	Ref*
HD 181475	19 20 48.3	−04 30 09	7.0	K7IIa	1
NR Vul	19 50 11.9	+24 55 24	9.4	M1Ia:	1
HD 188895	19 56 37.8	+23 53 19	6.9	K2	2
BD+35 4077	20 21 14.1	+35 37 17	9.7	M3Iab:	1
BI Cyg	20 21 21.9	+36 55 56	8.4	M4Iab	1
RW Cyg	20 28 50.6	+39 58 54	8.0	M3-M4Ia-Iab	1
ksi Cyg	21 04 55.9	+43 55 40	3.7	K4.5Ib-II	1
V419 Cep	21 12 47.2	+60 05 53	6.6	M2Ib	1
HD 203338	21 19 15.7	+58 37 25	5.8	M1Ibep	2
HD 205349	21 33 17.9	+45 51 14	6.2	K4Ib	1
mu Cep	21 43 30.5	+58 46 48	4.1	M2-Ia	1
VV Cep	21 56 39.1	+63 37 32	4.9	M2epIa-Iab+B8:eV	1
alf Aqr	22 05 47.0	−00 19 11	2.9	G2Ib	2
zet Cep	22 10 51.3	+58 12 05	3.4	K1.5Ib	1
RW Cep	22 23 07.0	+55 57 48	6.7	K2-K0-Ia	2
ST Cep	22 30 10.7	+57 00 03	9.7	M2Ia-Iab	1
W Cep	22 36 27.6	+58 25 34	7.6	M0Iaep	2
V424 Lac	22 56 26.0	+49 44 01	4.9	K5Ib	1
V809 Cas	23 19 23.8	+62 44 23	6.7	K4.5Ib	1
PZ Cas	23 44 03.3	+61 47 22	8.9	M3Ia	1
TZ Cas	23 52 56.2	+61 00 08	9.2	M3Iab	1

*References for V magnitude and spectral type: 1 = Levesque et al. 2005, 2 = Humphreys 1978

7.12 Identifying Merged RSGs

Using the high-resolution LDT-EXPRES spectra, we can determine the projected rotational velocities of their metal lines. We expect to see a split distribution of rotational velocities with a clump of merged RSGs around 15 km s^{-1} and the truly single RSGs around 5 km s^{-1}. However, it is important to remember that we can only measure the *projected* rotational velocities, $v \sin i$, and thus the split distribution will undoubtedly have a large amount of scatter. Any RSGs with large projected rotational velocities can be readily identified as merger candidates, but some mergers will be viewed nearly pole-on and will have small projected rotational velocities. We can correct for this statistically, assuming random alignment, but for that reason our sample size has to be large. If de Mink et al. (2014) is correct, around 20% of the stars we've observed will be merged. Thus, since we've observed 70 stars, we

expect around 14 of them to be merged RSGs.

At first glance, this process might seem simple – after all, measuring the rotational velocity of a spectral line is quite straightforward. However, in practice, this project has proven to be much more complicated than initially anticipated. The rotational velocities of RSGs have been measured before (such as with Betelgeuse), but previous methods relied on polarimetry to determine the rotational velocity across the star's resolved disk (Wheeler et al., 2017). Some of the RSGs we've observed here are close enough to be resolvable but we'd rather use a method that can be applied to any RSG with high spectroscopic resolution data. Such a method has been used with great success on red giant spectra, but in that case, the entire spectrum was compared to a model and rotationally broadened to determine the rotational velocity (Valenti & Fischer, 2005). This process cannot be applied to RSGs because of the differing physics behind line creation in RSGs vs. red giants. The extended atmospheres of RSGs means that the lines we observe are forming in different parts of the star. Since we're interested in the surface rotation, we need to make sure we're only measuring the rotational velocities of the lines that come from elements being formed on the surface. Luckily, new work in tomography of RSGs allows us to determine where individual lines are formed (Kravchenko et al., 2018, 2019, 2020). This recent research points to Fe lines being promising indicators of surface rotation. Luckily, there are enough of them that we can identify the unblended lines and measuring their rotational velocities should give us a good first indication of how fast these RSGs are rotating. We have additionally compared the rotational velocities given by various Fe lines in the spectrum of Betelgeuse to its expected rotational velocity of ~ 15 km s^{-1} and have found consistent, and thus promising, results. In the future, we hope to take a broader view at the entire spectrum, but focusing on the Fe lines is a good starting point.

Chapter 8

SUMMARY, CONCLUSIONS, AND NEXT STEPS

When this research began, there were only around a dozen known RSG binaries and the reason behind this rarity was not well understood. The search for binary RSGs began by determining that the stellar companions to RSGs will primarily be B-type stars (or stars with $M > 3M_{\odot}$). Stars more massive than this (WRs, O stars, etc.) are rare as dictated by the initial mass function, and stars less massive than this will still be protostars by the time a RSG has formed. RSG+B binaries will photometrically appear different than single RSGs or single B-type stars because of their strong flux in both the red and blue. Thus, candidate RSG+B binaries can be identified using archival photometric surveys such as the LGGS in M31 and M33 as well as the surveys in the MCs done by Zaritsky et al. (2002) and Zaritsky et al. (2004). Using the 6.5-m Magellan and MMT telescopes, we obtained spectra of candidate RSG+B binaries and confirmed 250 new systems in the Local Group galaxies. We then calculated the binary fraction of RSGs in the LMC, M31, and M33 using NIR photometry to identify a complete sample of RSGs and a k-NN classification algorithm to determine the probability that each RSG is in a binary system. Finally, we found that the RSG binary fraction decreases with decreasing metallicity.

While this thesis represents a significant advancement in our understanding of the binary fraction of RSGs, there is still much left to be done. To better understand the binary fraction and our sensitivity limits for detecting B-type companions, we've recently obtained spectra of an additional 40 RSG+B binary candidates in the LMC using GMOS on Gemini-S. This sample set focused on RSGs that are bright in the UV and should allow us to decrease the errors in the k-NN algorithm while hopefully discovering new binary RSGs. We additionally discovered around 10 new RSG+Be binary systems and have obtained multi-

epoch spectroscopy of these systems in an attempt to determine whether the emission showing in the B star spectrum is due to a disk around the B star or Roche-lobe overflow from the RSG (and thus the existence of an interacting system). Finally, as discussed in Chapter 7, we are continuing to investigate the mass-loss rates of binary vs. single RSGs and hope to better understand how they change with environmental metallicity.

This thesis has additionally raised a few open questions for the massive star community as a whole to answer. Long baseline radial velocity studies of RSGs, such as those being done by Patrick et al. (2019) and Dorda & Patrick (2021), are sensitive to RSG binary companions such as compact objects that our observational study could not detect. Thus, studies such as these are both crucial and complementary to the work presented here. Finally, we've hypothesized that the RSG binary fraction's change with metallicity is due to the parent population of OB binary systems having a different binary fraction with changing metallicity. This remains to be observationally confirmed. Because OB binaries will generally appear photometrically identical to single OB stars, a targeted spectroscopic or photometric monitoring campaign is needed. Hopefully with the advent of new large scale surveys, a massive project like this can be successful.

Massive stars such as RSGs are the cosmic engines of our Universe. Understanding their evolution brings us a tiny bit closer to understanding the creation of the heavy elements and building blocks for life we find here on Earth. While characterizing the binary fraction of RSGs is just one small component, hopefully in time these components can be added together to help us better understand our Universe.

BIBLIOGRAPHY

Aadland, E., Massey, P., Neugent, K. F., & Drout, M. R. 2018, AJ, 156, 294

Abbott, B. P., Abbott, R., Abbott, T. D., et al. 2016, Phys. Rev. Lett., 116, 241103

—. 2017, Phys. Rev. Lett., 119, 161101

—. 2019, Physical Review X, 9, 031040

Ahmad, I. A., & Parsons, S. B. 1985, ApJ, 299, L33

Antoniou, V., & Zezas, A. 2016, MNRAS, 459, 528

Baade, R., & Reimers, D. 2007, A&A, 474, 229

Baron, F., Monnier, J. D., Kiss, L. L., et al. 2014, ApJ, 785, 46

Bartzakos, P., Moffat, A. F. J., & Niemela, V. S. 2001, MNRAS, 324, 18

Bauer, W. H., & Bennett, P. D. 2000, PASP, 112, 31

Beasor, E. R., & Davies, B. 2016, MNRAS, 463, 1269

Bellm, E. C., Kulkarni, S. R., Graham, M. J., et al. 2019, PASP, 131, 018002

Bessell, M. S. 1990, PASP, 102, 1181

Bessell, M. S., & Brett, J. M. 1988, PASP, 100, 1134

Bessell, M. S., Castelli, F., & Plez, B. 1998, A&A, 333, 231

Bianchi, L. 2009, Ap&SS, 320, 11

Blackman, R. T., Fischer, D. A., Jurgenson, C. A., et al. 2020, AJ, 159, 238

Bonanos, A. Z., Lennon, D. J., Köhlinger, F., et al. 2010, AJ, 140, 416

Boyarchuk, A. A. 1985, in ESA Special Publication, Vol. 236, Recent Results on Cataclysmic Variables. The Importance of IUE and Exosat Results on Cataclysmic Variables and Low-Mass X-Ray Binaries, ed. W. R. Burke

Boyer, M. L., Srinivasan, S., van Loon, J. T., et al. 2011, AJ, 142, 103

Bray, J. C., & Eldridge, J. J. 2018, MNRAS, 480, 5657

Brunish, W. M., Gallagher, J. S., & Truran, J. W. 1986, AJ, 91, 598

Cardelli, J. A., Clayton, G. C., & Mathis, J. S. 1989, ApJ, 345, 245

Carpenter, J. M. 2001, AJ, 121, 2851

Casali, M., Adamson, A., Alves de Oliveira, C., et al. 2007, A&A, 467, 777

Castelli, F., Gratton, R. G., & Kurucz, R. L. 1997, A&A, 318, 841

Chiavassa, A., Pasquato, E., Jorissen, A., et al. 2011, in Astronomical Society of the Pacific Conference Series, Vol. 445, Why Galaxies Care about AGB Stars II: Shining Examples and Common Inhabitants, ed. F. Kerschbaum, T. Lebzelter, & R. F. Wing, 169

Chojnowski, S. D., Labadie-Bartz, J., Rivinius, T., et al. 2018, ApJ, 865, 76

Chun, M.-S. 1992, Journal of Astronomy and Space Sciences, 9, 143

Cioni, M. R. L., Girardi, L., Marigo, P., & Habing, H. J. 2006, A&A, 448, 77

Cousins, A. W. J. 1976, MmRAS, 81, 25

Cowley, A. P. 1969, Publications of the Astronomical Society of the Pacific, 81, 297

Cox, A. N. 2000, Allen's Astrophysical Quantities (New York: Springer)

Crowther, P. A. 2001, in Astrophysics and Space Science Library, Vol. 264, The Influence of Binaries on Stellar Population Studies, ed. D. Vanbeveren, 215

Cunningham, P., & Delany, S. J. 2020, arXiv e-prints, arXiv:2004.04523

Cutri, R. M., Skrutskie, M. F., van Dyk, S., et al. 2012, VizieR Online Data Catalog, II/281

Dalcanton, J. J., Williams, B. F., Lang, D., et al. 2012, ApJS, 200, 18

Davies, B., Crowther, P. A., & Beasor, E. R. 2018, MNRAS, 478, 3138

Davies, B., Figer, D. F., Law, C. J., et al. 2008, ApJ, 676, 1016

de Jager, C., Nieuwenhuijzen, H., & van der Hucht, K. A. 1988, A&AS, 72, 259

de Mink, S. E., Sana, H., Langer, N., Izzard, R. G., & Schneider, F. R. N. 2014, ApJ, 782, 7

Decin, L., Hony, S., de Koter, A., et al. 2006, A&A, 456, 549

Devereux, N. A., Price, R., Wells, L. A., & Duric, N. 1994, AJ, 108, 1667

Dorda, R., Negueruela, I., González-Fernández, C., & Marco, A. 2018, A&A, 618, A137

Dorda, R., & Patrick, L. R. 2021, MNRAS, arXiv:2010.15627

Dorn-Wallenstein, T. Z., & Levesque, E. M. 2018, ApJ, 867, 125

Dorn-Wallenstein, T. Z., Levesque, E. M., & Davenport, J. R. A. 2019, ApJ, 878, 155

Draine, B. T., Aniano, G., Krause, O., et al. 2014, ApJ, 780, 172

Drout, M. R., Massey, P., & Meynet, G. 2012, ApJ, 750, 97

Drout, M. R., Massey, P., Meynet, G., Tokarz, S., & Caldwell, N. 2009, ApJ, 703, 441

Ekström, S., Georgy, C., Eggenberger, P., et al. 2012, A&A, 537, A146

Eldridge, J. J., Izzard, R. G., & Tout, C. A. 2008, MNRAS, 384, 1109

Eldridge, J. J., Stanway, E. R., Xiao, L., et al. 2017, PASA, 34, e058

Eldridge, J. J., Xiao, L., Stanway, E. R., Rodrigues, N., & Guo, N. Y. 2018, PASA, 35, 49

Elias, J. H., Frogel, J. A., & Humphreys, R. M. 1985, ApJS, 57, 91

Esteban, C., Bresolin, F., García-Rojas, J., & Toribio San Cipriano, L. 2020, MNRAS, 491, 2137

Evans, K. A., & Massey, P. 2017, in American Astronomical Society Meeting Abstracts #229, Vol. 229, 154.04

Fabricant, D., Fata, R., Roll, J., et al. 2005, PASP, 117, 1411

Fabricant, D. G., Kurtz, M. J., Geller, M. J., et al. 2008, Publications of the Astronomical Society of the Pacific, 120, 1222

Foellmi, C., Moffat, A. F. J., & Guerrero, M. A. 2003a, MNRAS, 338, 360

—. 2003b, MNRAS, 338, 1025

Gaia Collaboration, Helmi, A., van Leeuwen, F., et al. 2018, A&A, 616, A12

Garmany, C. D., Conti, P. S., & Massey, P. 1980, ApJ, 242, 1063

Georgy, C. 2012, A&A, 538, L8

Georgy, C., & Ekström, S. 2015, in EAS Publications Series, Vol. 71, EAS Publications Series, 41–46

Georgy, C., & Ekström, S. 2018, ArXiv e-prints, arXiv:1808.09231

Georgy, C., Granada, A., Ekström, S., et al. 2014a, A&A, 566, A21

Georgy, C., Saio, H., & Meynet, G. 2014b, MNRAS, 439, L6

Georgy, C., Ekström, S., Eggenberger, P., et al. 2013, A&A, 558, A103

Gies, D. R. 2008, in Massive Star Formation: Observations Confront Theory, ed. H. Beuther, H. Linz, & T. Henning, Vol. 387, 93

Götberg, Y., de Mink, S. E., Groh, J. H., Leitherer, C., & Norman, C. 2019, A&A, 629, A134

Gray, R. O., & Skiff, B. A. 2004, PASP, 116, 1123

Guo, J. H., & Li, Y. 2002, ApJ, 565, 559

Gustafsson, B., Bell, R. A., Eriksson, K., & Nordlund, A. 1975, A&A, 42, 407

Haberl, F., & Sturm, R. 2016, A&A, 586, A81

Hambly, N. C., Collins, R. S., Cross, N. J. G., et al. 2008, MNRAS, 384, 637

Hayashi, C., & Hoshi, R. 1961, PASJ, 13, 442

Hecht, J. H., Clayton, G. C., Drilling, J. S., & Jeffery, C. S. 1998, ApJ, 501, 813

Heida, M., Jonker, P. G., Torres, M. A. P., et al. 2016, MNRAS, 459, 771

Hinkle, K. H., Lebzelter, T., Fekel, F. C., et al. 2020, ApJ, 904, 143

Huang, W., & Gies, D. R. 2006, ApJ, 648, 591

Humphreys, R. M. 1978, ApJS, 38, 309

Humphreys, R. M., & McElroy, D. B. 1984, ApJ, 284, 565

Hunter, D. A., Shaya, E. J., Holtzman, J. A., et al. 1995, ApJ, 448, 179

Husser, T.-O., Wende-von Berg, S., Dreizler, S., et al. 2013, A&A, 553, A6

Jacoby, G. H., Hunter, D. A., & Christian, C. A. 1984, ApJS, 56, 257

Johnson, H. L., & Morgan, W. W. 1953, ApJ, 117, 313

Josselin, E., Blommaert, J. A. D. L., Groenewegen, M. A. T., Omont, A., & Li, F. L. 2000, A&A, 357, 225

Jura, M., & Jacoby, G. 1976, Astrophys. Lett., 18, 5

Jurgenson, C., Fischer, D., McCracken, T., et al. 2016, Journal of Astronomical Instrumentation, 5, 1650003

Keyes, C. D., & Preblich, B. 2004, AJ, 128, 2981

Kilkenny, D., Holmgren, D., van Wyk, F., et al. 1995, The Observatory, 115, 31

Kochanek, C. S., Shappee, B. J., Stanek, K. Z., et al. 2017, PASP, 129, 104502

Kravchenko, K., Chiavassa, A., Van Eck, S., et al. 2019, A&A, 632, A28

Kravchenko, K., Van Eck, S., Chiavassa, A., et al. 2018, A&A, 610, A29

Kravchenko, K., Wittkowski, M., Jorissen, A., et al. 2020, A&A, 642, A235

Lamers, H. J. G. L. M., & Levesque, E. M. 2017, Understanding Stellar Evolution, doi:10.1088/978-0-7503-1278-3

Lanz, T., & Hubeny, I. 2007, ApJS, 169, 83

Lesh, J. R. 1968, ApJS, 17, 371

Levesque, E. M. 2017, Astrophysics of Red Supergiants (Bristol: IOP), doi:10.1088/978-0-7503-1329-2

Levesque, E. M., & Massey, P. 2020, ApJ, 891, L37

Levesque, E. M., Massey, P., Olsen, K. A. G., & Plez, B. 2007, ApJ, 667, 202

Levesque, E. M., Massey, P., Olsen, K. A. G., et al. 2005, ApJ, 628, 973

—. 2006, ApJ, 645, 1102

Levesque, E. M., Massey, P., Plez, B., & Olsen, K. A. G. 2009, AJ, 137, 4744

Levesque, E. M., Massey, P., Żytkow, A. N., & Morrell, N. 2014, MNRAS, 443, L94

Lindegren, L., Hernández, J., Bombrun, A., et al. 2018, A&A, 616, A2

López, K. M., Heida, M., Jonker, P. G., et al. 2017, MNRAS, 469, 671

Maeder, A. 1991, A&A, 242, 93

Maeder, A., & Conti, P. S. 1994, ARA&A, 32, 227

Maeder, A., Lequeux, J., & Azzopardi, M. 1980, A&A, 90, L17

Maeder, A., & Meynet, G. 2000, ARA&A, 38, 143

Magrini, L., Vílchez, J. M., Mampaso, A., Corradi, R. L. M., & Leisy, P. 2007, A&A, 470, 865

Marshall, J. L., Burles, S., Thompson, I. B., et al. 2008, in Proc. SPIE, Vol. 7014, Ground-based and Airborne Instrumentation for Astronomy II, 701454

Martin, C., & GALEX Team. 2005, in Multiwavelength Mapping of Galaxy Formation and Evolution, ed. A. Renzini & R. Bender, 197

Massey, P. 1998, ApJ, 501, 153

—. 2002, ApJS, 141, 81

Massey, P., & Evans, K. A. 2016, ApJ, 826, 224

Massey, P., & Hanson, M. M. 2013, in Planets, Stars and Stellar Systems. Volume 2: Astronomical Techniques, Software and Data, ed. T. D. Oswalt & H. E. Bond (Dordrecht: Springer), 35

Massey, P., McNeill, R. T., Olsen, K. A. G., et al. 2007a, AJ, 134, 2474

Massey, P., Neugent, K. F., & Levesque, E. M. 2017, Philosophical Transactions of the Royal Society of London Series A, 375, 20160267

—. 2019, AJ, 157, 227

Massey, P., Neugent, K. F., Levesque, E. M., Drout, M. R., & Courteau, S. 2021, AJ, 161, 79

Massey, P., Neugent, K. F., Morrell, N., & Hillier, D. J. 2014, ApJ, 788, 83

Massey, P., Neugent, K. F., & Smart, B. M. 2016, AJ, 152, 62

Massey, P., & Olsen, K. A. G. 2003, AJ, 126, 2867

Massey, P., Olsen, K. A. G., Hodge, P. W., et al. 2007b, AJ, 133, 2393

—. 2006, AJ, 131, 2478

Massey, P., Plez, B., Levesque, E. M., et al. 2005, ApJ, 634, 1286

Massey, P., Silva, D. R., Levesque, E. M., et al. 2009, ApJ, 703, 420

Mauron, N., & Josselin, E. 2011, A&A, 526, A156

McLaughlin, D. B. 1950, ApJ, 111, 449

Meynet, G., & Maeder, A. 2002, A&A, 390, 561

Meynet, G., Chomienne, V., Ekström, S., et al. 2015, A&A, 575, A60

Mikołajewska, J. 2007, Baltic Astronomy, 16, 1

Mochejska, B. J., Kaluzny, J., Stanek, K. Z., Krockenberger, M., & Sasselov, D. D. 1999, AJ, 118, 2211

Moe, M., & Di Stefano, R. 2017, ApJS, 230, 15

Moe, M., Kratter, K. M., & Badenes, C. 2019, ApJ, 875, 61

Morrissey, P., Conrow, T., Barlow, T. A., et al. 2007, ApJS, 173, 682

Munari, U., & Zwitter, T. 2002, A&A, 383, 188

Munari, U., Corradi, R. L. M., Henden, A., et al. 2007, A&A, 474, 585

Neugent, K. F. 2021, ApJ, 908, 87

Neugent, K. F., Levesque, E. M., & Massey, P. 2018a, AJ, 156, 225

Neugent, K. F., Levesque, E. M., Massey, P., & Morrell, N. I. 2019, ApJ, 875, 124

Neugent, K. F., Levesque, E. M., Massey, P., Morrell, N. I., & Drout, M. R. 2020a, ApJ, 900, 118

Neugent, K. F., & Massey, P. 2011, ApJ, 733, 123

—. 2014, ApJ, 789, 10

Neugent, K. F., Massey, P., & Georgy, C. 2012a, ApJ, 759, 11

Neugent, K. F., Massey, P., Georgy, C., et al. 2020b, ApJ, 889, 44

Neugent, K. F., Massey, P., & Morrell, N. 2018b, ApJ, 863, 181

Neugent, K. F., Massey, P., Skiff, B., et al. 2010, ApJ, 719, 1784

Neugent, K. F., Massey, P., Skiff, B., & Meynet, G. 2012b, ApJ, 749, 177

Nidever, D. L., Olsen, K., Choi, Y., et al. 2019, ApJ, 874, 118

Patrick, L. R., Lennon, D. J., Britavskiy, N., et al. 2019, A&A, 624, A129

Pedregosa, F., Varoquaux, G., Gramfort, A., et al. 2011, Journal of Machine Learning Research, 12, 2825

Petersburg, R. R., Ong, J. M. J., Zhao, L. L., et al. 2020, AJ, 159, 187

Plez, B., Brett, J. M., & Nordlund, A. 1992, A&A, 256, 551

Podsiadlowski, P., Joss, P. C., & Hsu, J. J. L. 1992, ApJ, 391, 246

Pollmann, E., Vollmann, W., & Bennett, P. D. 2017, Information Bulletin on Variable Stars, 6198, 1

Reimers, D. 1975, Memoires of the Societe Royale des Sciences de Liege, 8, 369

—. 1977, A&A, 57, 395

Rivinius, T., Carciofi, A. C., & Martayan, C. 2013, A&A Rev., 21, 69

Roberts, M. S. 1966, ApJ, 144, 639

Russell, S. C., & Dopita, M. A. 1990, ApJS, 74, 93

Saio, H., Georgy, C., & Meynet, G. 2013, MNRAS, 433, 1246

Salpeter, E. E. 1955, ApJ, 121, 161

Samus, N. N., Kazarovets, E. V., Durlevich, O. V., Kireeva, N. N., & Pastukhova, E. N. 2009, VizieR Online Data Catalog, 1

Sana, H., de Mink, S. E., de Koter, A., et al. 2012, Science, 337, 444

Sana, H., de Koter, A., de Mink, S. E., et al. 2013, A&A, 550, A107

Sanders, N. E., Caldwell, N., McDowell, J., & Harding, P. 2012, ApJ, 758, 133

Schaller, G., Schaerer, D., Meynet, G., & Maeder, A. 1992, A&AS, 96, 269

Schlegel, D. J., Finkbeiner, D. P., & Davis, M. 1998, ApJ, 500, 525

Shappee, B. J., Prieto, J. L., Grupe, D., et al. 2014, ApJ, 788, 48

Shenoy, D., Humphreys, R. M., Jones, T. J., et al. 2016, AJ, 151, 51

Simons, R., Thilker, D., Bianchi, L., & Wyder, T. 2014, Advances in Space Research, 53, 939

Skrutskie, M. F., Cutri, R. M., Stiening, R., et al. 2006, AJ, 131, 1163

Smartt, S. J., Eldridge, J. J., Crockett, R. M., & Maund, J. R. 2009, MNRAS, 395, 1409

Smith, N., Humphreys, R. M., Davidson, K., et al. 2001, AJ, 121, 1111

Stanway, E. R., & Eldridge, J. J. 2018, MNRAS, 479, 75

Stanway, E. R., Eldridge, J. J., & Becker, G. D. 2016, MNRAS, 456, 485

Stencel, R. E., Hopkins, J. L., Hagen, W., et al. 1984, ApJ, 281, 751

Stothers, R., & Leung, K. C. 1971, A&A, 10, 290

Stothers, R. B. 2010, ApJ, 725, 1170

Sylvester, R. J., Skinner, C. J., & Barlow, M. J. 1998, MNRAS, 301, 1083

Szczygieł, D. M., Stanek, K. Z., Bonanos, A. Z., et al. 2010, AJ, 140, 14

Tauris, T. M., Kramer, M., Freire, P. C. C., et al. 2017, ApJ, 846, 170

Thompson, T. A., Kochanek, C. S., Stanek, K. Z., et al. 2019, Science, 366, 637

Toribio San Cipriano, L., García-Rojas, J., Esteban, C., Bresolin, F., & Peimbert, M. 2016, MNRAS, 458, 1866

Tycner, C., Jones, C. E., Sigut, T. A. A., et al. 2008, ApJ, 689, 461

Tylenda, R., Kamiński, T., & Schmidt, M. 2009, A&A, 503, 899

Tylenda, R., Kamiński, T., Schmidt, M., Kurtev, R., & Tomov, T. 2011, A&A, 532, A138

Valenti, J. A., & Fischer, D. A. 2005, ApJS, 159, 141

van den Bergh, S. 2000, The Galaxies of the Local Group (Cambridge: Cambridge Univ. Press)

van der Marel, R. P., Fardal, M. A., Sohn, S. T., et al. 2019, ApJ, 872, 24

van Loon, J. T., Cioni, M. R. L., Zijlstra, A. A., & Loup, C. 2005, A&A, 438, 273

van Loon, J. T., Groenewegen, M. A. T., de Koter, A., et al. 1999, A&A, 351, 559

Vinter Hansen, J. M. 1944, ApJ, 100, 8

Wellstein, S., & Langer, N. 1999, A&A, 350, 148

Wenger, M., Ochsenbein, F., Egret, D., et al. 2000, A&AS, 143, 9

Wheeler, J. C., Nance, S., Diaz, M., et al. 2017, MNRAS, 465, 2654

Williams, B. F., Durbin, M. J., Dalcanton, J. J., et al. 2021, arXiv e-prints, arXiv:2101.01293

Wittkowski, M., Abellán, F. J., Arroyo-Torres, B., et al. 2017, A&A, 606, L1

Yang, M., Bonanos, A. Z., Jiang, B.-W., et al. 2019, A&A, 629, A91

Zapartas, E., de Mink, S. E., Justham, S., et al. 2019, A&A, 631, A5

Zaritsky, D., Harris, J., Thompson, I. B., & Grebel, E. K. 2004, AJ, 128, 1606

Zaritsky, D., Harris, J., Thompson, I. B., Grebel, E. K., & Massey, P. 2002, AJ, 123, 855

Zaritsky, D., Kennicutt, Robert C., J., & Huchra, J. P. 1994, ApJ, 420, 87

Zorec, J., & Briot, D. 1997, A&A, 318, 443